

Multi-Scale Modeling of Gas Flows with Continuum-Rarefied Transitions

Application to Expanding Gas Jets in Thin Film
Deposition Processes

Multi-Scale Modeling of Gas Flows with Continuum-Rarefied Transitions

Application to Expanding Gas Jets in Thin Film
Deposition Processes

PROEFSCHRIFT

ter verkrijging van de graad van doctor
aan de Technische Universiteit Delft,
op gezag van de Rector Magnificus prof. dr. ir. J. T. Fokkema,
voorzitter van het College voor Promoties,
in het openbaar te verdedigen op
maandag 12 januari 2009 om 12:30 uur

door

Giannandrea ABBATE

Ingenereer Aerospace - Università degli Studi "Federico II" di Napoli (Italy)
geboren te Caserta (Italy)

Dit proefschrift is goedgekeurd door de promotoren:

Prof. dr. ir. C.R. Kleijn

Prof. dr. B.J. Thijsse

Samenstelling promotiecommissie:

Rector Magnificus, voorzitter

Prof. dr. ir. C.R. Kleijn,

Technische Universiteit Delft, promotor

Prof. dr. B.J. Thijsse,

Technische Universiteit Delft, promotor

Prof. dr. G. Zuppari,

Università degli Studi "Federico II" di Napoli

Prof. dr. W.J. Goedheer,

Universiteit Utrecht

Prof. dr. ir. A.A. van Steenhoven,

Technische Universiteit Eindhoven

Prof. dr. ir. C. Vuik,

Technische Universiteit Delft

Prof. dr. ir. M.C.M. van de Sanden,

Technische Universiteit Eindhoven

This project was supported by the Delft Centre for Computational Science and Engineering (DCSE)

Cover:

Expanding thermal plasma.

The picture was taken in the group of Plasma & Materials Processing (P&MP) at the Eindhoven University of Technology (TU/e).

Printed by Ponsen & Looijen b.v., Wageningen, the Netherlands

Copyright © 2008 by Giannandrea Abbate.

All rights reserved. No part of the material protected by this copyright notice may be reproduced or utilized in any form or by any means, electronic or mechanical, including photocopying, recording, or by any information storage and retrieval system without written permission from the publisher.

Ai miei nonni

Contents

Contents	vii
List of symbols	xi
Summary	xv
Samenvatting	xvii
1 Introduction	1
1.1 Project background	1
1.1.1 Numerical simulation of gas flow in different flow regimes . . .	1
1.1.2 Thin film deposition based on an expanding thermal plasma . .	3
1.2 Continuum-rarefied transition in supersonically expanding plasma . .	4
1.2.1 The reactor	4
1.2.2 The model	4
1.2.3 The flowfield	8
1.2.4 The continuum-rarefied flow transition	10
1.3 Motivation and aim	11
1.4 Rarefied flow simulations in the Department of Multi-Scale Physics . .	12
1.5 Thesis outline	12
1.6 Acknowledgment	13
2 Numerical methods	15
2.1 From Boltzmann to Navier-Stokes	15
2.2 Finite volume scheme for compressible Navier-Stokes equations	20
2.2.1 Finite volume discretization	21
2.2.2 Time discretization	21
2.2.3 The MUSCL discretization scheme	22
2.2.4 Chapman-Enskog split fluxes	24
2.2.5 Boundary conditions	25

2.2.6	Validation	26
2.2.6.1	Sod's problem	26
2.2.6.2	Poiseuille flow	28
2.2.6.3	Couette flow	30
2.2.6.4	Jet expansion in a cylindrical chamber	31
2.2.6.5	Concluding remarks	33
2.3	Direct Simulation Monte Carlo scheme for rarefied gas flows	34
2.3.1	Initialization	35
2.3.2	Particle movement and boundary interaction	36
2.3.3	Particle collisions	38
2.3.3.1	Collision models	39
2.3.4	Sampling	40
2.3.5	Radial weighting factors	41
2.3.6	Validation	42
2.3.6.1	Fluid between two flat plates at different temperature	42
2.3.6.2	The impulsive piston	44
2.3.6.3	Rarefied Poiseuille flow	45
2.3.6.4	Rarefied Couette flow	47
2.3.6.5	Concluding remarks	48
3	Development of a hybrid N-S/DSMC solver	49
3.1	Introduction	49
3.2	Breakdown parameter	51
3.3	Steady-state formulation	53
3.4	Unsteady formulation	54
3.5	Results and discussion	55
3.5.1	Unsteady shock-tube problem	55
3.5.1.1	Sensitivity to numerical parameters	58
3.5.2	Unsteady pressure-driven slit flow	62
3.5.3	Rarefied Poiseuille flow	67
3.6	Conclusions	69
4	Influence of rarefaction on a supersonic hot gas expansion	71
4.1	Introduction	71
4.2	Studied configuration and measurement technique	73
4.3	Numerical simulation method	73
4.3.1	Modelled geometry	74
4.4	Results and discussion	76
4.4.1	General flowfield characteristics and rarefaction effects	76
4.4.2	Invasion of the supersonic region by background particles	85
4.5	Conclusions	89

5 Conclusions	91
5.1 CFD/DSMC coupling in steady-state and transient flows	91
5.2 Influence of rarefaction on expanding gas jet hydrodynamics	92
5.3 Supersonic region invasion by background particles in rarefied super- sonic jet expansion	93
5.4 General conclusions and outlook	94
Bibliography	95
Acknowledgements	103
List of publications	105
About the author	107

List of symbols

Greek letters

α	VSS model parameter	-
β	compression parameter for the MUSCL scheme	-
γ	ratio of specific heat	-
ε	additional internal energy for polyatomic molecules; prescribed small value	J; -
δ	Kronecker delta	-
Δ	discreet value; difference	-
Δt_c	mean collision time	s
θ	circumferential coordinate; weighting parameter for the integration scheme	deg; -
λ	mean free path length	m
μ	coefficient of viscosity	kg/(m s)
ρ	density	kg/m ³
σ_T	total collision cross-section	m ²
τ	viscous stress tensor	Pa
ϕ	flow property; generic function	-
χ	deflection angle	rad
ω	viscosity-temperature exponent	-
Ω	computational domain	-

Roman letters

a	generic variable	-
b	generic variable; miss distance or impact parameter	-; m
A	surface area	m ²
c	molecular velocity	m/s

c_r	molecules' relative speed	m/s
C	thermal velocity; Courant number	m/s; -
C_r	most probable molecular velocity	m/s
C_T	jump length	m
d	diameter; collision diameter	m
e	energy	J/kg
E	noise	-
f	velocity distribution function	-
F	flux vector	-
F_{num}	ratio between the number of real molecules and the DSMC simulated particles	-
h	height; distance	m
k	weighting parameter for the MUSCL scheme	-
k_B	Boltzmann constant	$\text{m}^2\text{kg}/(\text{s}^2 \text{K})$
K	coefficient of thermal conductivity	$\text{W}/(\text{m K})$
Kn	Knudsen number	-
l	length	m
L	characteristic length scale; length; distance	m
m	molecular mass	kg
\dot{m}	mass flow	$\text{kg}/(\text{m}^2\text{s})$
m_r	reduced mass of the two colliding molecules	kg
M	Mach number	-
n	number density	m^{-3}
N	number of DSMC simulated particles	-
N_c	number of collision pairs	-
p	pressure	Pa
P	pressure; collision probability	Pa; -
P_{1-2}	pressure ratio	-
q	heat flux	W/m^2
Q	generic function; generic flow property	-
r	radial coordinate	m
R	radius; specific gas constant; random number	m; $\text{J}/(\text{kg K})$; -
Re	Reynolds number	-
S	surface; speed ratio	m^2 ; -
t	time	s
T	temperature	K
u	velocity component	m/s
U	state vector	-
v	velocity	m/s
V	volume; velocity	m^3 ; m/s

V_0	fluid velocity at the symmetry axis	m/s
V_{ma}	mass average velocity	m/s
V_{slip}	slip velocity at the wall	m/s
W	radial weighting factor	-
x	spatial coordinate; particle position	m; -
X	particle position	-
y, z	spatial coordinates	m

Subscripts

ρ	based on density
arc	inside the arc
BC	boundary conditions
cham	chamber
coupling	referring to the coupling method
CFD	referring to the Computational Fluid Dynamics method
DSMC	referring to the Direct Simulation Monte Carlo method
<i>energy</i>	energy
f	fluxes
in	inlet
int	internal
<i>int-energy</i>	internal energy
<i>mass</i>	mass
max	maximum value
n	normal to a planar surface
new	new value
<i>n-mom</i>	momentum in the direction normal to a surface
nozzle	inside the nozzle
old	old value
out	outlet
Q	based on a generic flow property Q
ref	reference value
s	inside the plasma source
split	limiting value used to split the continuum from the molecular region
sub	substrate
<i>sv</i>	state variables
temp	temporary
<i>tr-energy</i>	transitional energy
$t1, t2$	coordinate variables tangential to a planar surface
<i>t1-mom</i>	momentum in the direction tangential to a surface

T	based on temperature
V	based on the velocity
w	wall
x	in the x direction
y	in the y direction
0	referring to the fluid

Superscripts

CE	Chapman-Enskog
INV	invariant
L	left
Max	Maxwellian
R	right
*	dimensionless value

Summary

Multi-Scale Modeling of Gas Flows with Continuum-Rarefied Transitions

Giannandrea Abbate, Delft University of Technology

Several gas fluidic applications of current technological importance involve a gas jet supersonically expanding into vacuum or into a low pressure environment. Examples include: gas thruster nozzles and plume flows and processes of thin film deposition, etching and passivation from expanding plasma or gas jets.

An interesting issue connected to this kind of flows is the transition from the continuum to the rarefied regime. The gas in the jet is generally at relatively high pressure, and then it rapidly expands into a low pressure environment. For this reason, the gas first supersonically expands and then quickly compresses through a stationary shock wave (Mach disk). In addition, the expansion zone is surrounded by a barrel shaped shock (the so called barrel shock). Because of the low environment pressure and high thermodynamic gradients in the shock region, the flow undergoes a spatial transition from the low Knudsen number (Kn) continuum regime to the high Knudsen number rarefied regime.

Although several studies have been devoted to supersonic expansion of gas jets in vacuum or low pressure environment, full understanding of the processes governing the flow has not been reached yet. In particular, it is still not completely clear how important the influence of the rarefaction effects is on the dynamics of the flow. Another important question is whether the barrel shock, which becomes transparent to background molecules due to rarefaction effects, still protects the supersonic part of the flow.

Numerical simulation tools commonly used to study and design expanding gas jets configurations, are generally based on continuum assumptions, and therefore cannot accurately account for rarefaction effects.

Alternatively, DSMC (Direct Simulation Monte Carlo) has been used to simulate these flows. Rather than solving the Navier-Stokes equations, DSMC attempts to find approximate solutions to the Boltzmann equation by tracking the motion of

large numbers of individual computational molecules. Thus, it can account for rarefaction effects in regions with high Knudsen numbers. However, due to computational restraints it is practically impossible to accurately perform DSMC simulations in regions of low Knudsen numbers, i.e. where near-continuum conditions are present. In order to accurately simulate the above types of gas flows, one needs to construct a model that on the one hand accounts for the molecular nature of the gas flow where needed, and on the other hand uses a continuum model where allowed. The work in this thesis is a first step in fulfilling this requirement. The aim is: development, and validation of a hybrid Navier-Stokes/DSMC simulation tool, capable of modelling gas flows with spatial or temporal transitions from the continuum to the free molecular regime, and its application to expanding gas jets as applied in thin film deposition processes.

To this end, a simulation code named CROW (Continuum Rarefied flow) was developed, in which a CFD solver for the compressible Navier-Stokes equations was dynamically coupled to a DSMC solver for the rarefied regime. A Schwarz type overlapping method, with Dirichlet-Dirichlet boundary conditions, was employed for the coupling. The overlap region is dynamically and automatically adjusted to cover the zone where the flow undergoes continuum-rarefied transition (i.e. the zone around the $\text{Kn} \approx 0.05$ isosurface). The chosen coupling approach has several advantages over other coupling methods, such as non-overlapping and flux-based models most frequently used in literature. These advantages include less sensitivity to the DSMC statistical noise, and the possibility to decouple CFD and DSMC time steps.

The CFD and DSMC methods were validated against known analytical and numerical solutions from literature, independently, and then together in the hybrid CFD/DSMC coupled approach. The numerical results of the developed code were very satisfactory in all cases, leading to the conclusion that the developed hybrid CFD/DSMC approach in general, and the CROW code specifically, is a very promising tool for use in continuum-rarefied flow transitions.

Finally, the developed code was used for the simulation of an expanding gas jet in a low pressure reactor for thin film deposition. In this particular case two issues were addressed: (i) to show the importance of rarefaction effects on the flow field and (ii) the study of the presence in the supersonic region of particles coming from the subsonic part through the shock. Due to rarefaction effects, the barrel shock becomes transparent and does not preserve the supersonic part of the flow from the invasion of particles present outside it in the subsonic region. These molecules could, therefore, influence the supersonic region and its properties.

Samenvatting

Multi-scale modellering van gasstromingen met transitie van het continuu regime naar het ijle regime

Giannandrea Abbate, Delft University of Technology

Supersone gas- en plasmajets die expanderen van ongeveer atmosferische druk naar een omgeving waarin een (zeer) lage druk heerst worden veelvuldig toegepast in de techniek. Enkele voorbeelden zijn: voortstuwing via gasstoming door een straalbuis, depositie van dunne films vanuit de gasfase, etsen en passificatie van oppervlakken door middel van plasma- en gasjets.

Een interessant aspect van dit type stromingen is de transitie van continuu condities naar ijle condities. Het gas in de jet expandeert eerst supersonisch, om vervolgens snel gecompriëerd te worden door middel van een stationaire schok (Mach disk). De expansiezone is hierbij omringd door een tweede schok in de vorm van een holle cilinder (de zogenaamde barrel shock). Vanwege de lage druk en hoge temperatuurgradiënten rond de schok neemt het Knudsen getal daar plotseling sterk toe en vindt een transitie plaats van het continuu regime (lage Knudsen getallen, $Kn < 0.01$) naar het ijle regime (hoge Knudsen getallen, $Kn > 0.1$).

Ofschoon er reeds vele studies zijn verricht naar dit soort supersoon expanderende jets, ontbreekt nog een volledig begrip van de hydrodynamica. Met name is het niet volledig duidelijk welke invloed de transitie naar ijle condities heeft op het dynamisch gedrag van de stroming. Een andere belangrijke vraag is of onder dit soort condities de barrel shock ondoordringbaar blijft voor langzame deeltjes in de omgeving van de expansie, of dat deze deeltjes de expansie-zone door de schok kunnen binnendringen. De numerieke simulatiemodellen die gebruikt worden om expanderende gasjets te bestuderen en ontwerpen zijn meestal gebaseerd op continuumaannamen en kunnen daarom het effect van ijelheid op de stroming niet goed in rekening brengen.

Een alternatief om dit type stoming te simuleren is het gebruik van de DSMC (Direct Simulation Monte Carlo) methode. Door de beweging van grote aantallen discrete deeltjes te simuleren geeft deze methode een benaderende oplossing van de Boltzmann

vergelijking. Daarmee is de DSMC techniek bij uitstek geschikt voor het simuleren van gasstromingen in gebieden met een hoog Knudsen getal. De aard van de methode brengt echter met zich mee dat het een onrealistisch grote computerkracht vergt om nauwkeurige DSMC simulaties uit te voeren in gebieden waar continuüm condities heersen en het Knudsen getal laag is.

Voor de nauwkeurige en efficiënte simulatie van naar vacuüm expanderende gasjets moet dus een model geconstrueerd worden dat enerzijds – daar waar noodzakelijk – het ijle karakter van de gasstroming in rekening brengt en anderzijds – daar waar toegestaan – uitgaat van continuümaannames.

Dit proefschrift beschrijft de ontwikkeling van zo'n simulatiemodel. Het doel is: (1) ontwikkeling en validatie van een hybride Navier-Stokes/DSMC simulatiecode, die in staat is om gasstromingen te modelleren waarin temporele en/of ruimtelijke transitie plaatsvinden van het continuüm naar het ijle regime en (2) het gebruik van deze code bij de bestudering van de hydrodynamica van in vacuüm expanderende gasjets zoals die worden toegepast bij de depositie van dunne films. Hiertoe is de simulatiecode CROW (Continuum Rarefied flow) ontwikkeld, waarin een compressibele Navier-Stokes solver dynamisch gekoppeld is aan een DSMC solver. Voor deze koppeling is gebruik gemaakt van een overlapmethode van het Schwarz-type, met Dirichlet-Dirichlet randvoorwaarden. De overlapzone wordt automatisch bepaald als het gebied rond het $Kn \approx 0.05$ isoppervlak, waarin de stroming een transitie ondergaat van continuüm naar ijl of vice versa dekken en dynamisch aangepast aan veranderingen in de stromingscondities. Deze gekozen koppelmethode heeft verschillende voordelen ten opzichte van andere, niet-overlappende of flux-gebaseerde, koppelmethode zoals die beschreven zijn in de literatuur. Zo is de in dit proefschrift beschreven koppelingstechniek minder gevoelig voor statistische ruis in de DSMC simulaties en kunnen voor de CFD en de DSMC simulaties verschillende tijdstappen worden gebruikt. De ontwikkelde CFD en DSMC codes zijn allereerst onafhankelijk van elkaar gevalideerd aan de hand van analytische en numerieke oplossingen uit de literatuur. Vervolgens is de hybride CFD/DSMC code gevalideerd. Uit deze validatiestudies is geconcludeerd dat de ontwikkelde hybride CFD/DSMC aanpak, en de CROW code waarin deze is geïmplementeerd, veelbelovend zijn voor de simulatie van gasstromingen met transitie van het continuüm naar het ijle regime.

Tenslotte is de ontwikkelde code gebruikt om de expansie te simuleren van een gasjet die is gegenereerd bij ongeveer atmosferische druk en vervolgens expandeert in een lage druk (20-100 Pa) reactor zoals gebruikt voor de depositie van dunne films. Twee aspecten zijn specifiek bestudeerd: (1) het belang van ijlheidseffecten op het stromingsveld en (2) de aanwezigheid van subsone deeltjes, afkomstig uit de omgeving, in de supersone expansiezone. Geconcludeerd werd dat de barrelshock door ijlheidseffecten transparant wordt voor penetratie van subsone deeltjes. Deze kunnen daardoor de supersone expansiezone binnedringen en aldaar de stroming en temperatuur beïnvloeden.

1. Introduction

1.1 Project background

1.1.1 Numerical simulation of gas flow in different flow regimes

In many areas of science and industry, a very important tool for the design and optimization of equipment is the numerical simulation of gas flows. Most of the existing gas flows can be simulated using the continuum transport equations (Navier-Stokes), which describe the transport of mass, momentum and energy. These equations are based on the hypothesis that the mean free path length λ of the gas molecules is very small in comparison to a characteristic dimension L of the flow. This dimension can be either a physical dimension, e.g. a pipe diameter, or a flow dimension, e.g. the gradient length scale $(\frac{1}{\phi} \frac{\partial \phi}{\partial x})^{-1}$ on which some flow property ϕ changes significantly. The dimensionless Knudsen number Kn can be used to describe this situation:

$$\text{Kn} = \frac{\lambda}{L} \tag{1.1}$$

When $\text{Kn} < 0.01$, gas molecules travel only a small distance (compared to the geometry and flow dimensions) between collisions. For internal flows this means that molecules only very rarely collide with walls, and the flow is dominated by the characteristics of the inter-molecular collisions. The flow can then be described as a "continuum" flow, which means that we can safely ignore the fact that a gas consists of many small particles. The continuum Navier-Stokes (N-S) transport equations (including the continuum constitutive relations for the shear tensor and the heat flux) can be used to calculate flow properties in this case.

However, there are situations in which Kn is not so small, e.g. flows at low pressure, where λ becomes high, or flows with very small dimension L , e.g. microfluidics. The high Kn number in these flows indicate that a molecule travels a significant distance (compared to L) between collisions. For an internal flow, this implies that wall interactions occur more frequently and become important in describing the flow. The range where Kn is between ~ 0.01 and ~ 10 is called the "rarefied" or "transitional regime". In this regime, the flow can no longer be described as a continuum and the well known transport equations, or more precisely, the relations for shear tensor and

the heat flux, can no longer be used. In this regime, the particulate nature of the gas becomes important and a different simulation method must be used. The mathematical model at this level is the Boltzmann equation [1]. It provides information on the position, velocity and state of every molecule at all times. As a consequence of its complexity, the Boltzmann equation is not amenable to analytical solution for non-trivial problems.

In the continuum regime, numerical simulations can be done using (commercially available) Computational Fluid Dynamics (CFD) codes based on partial differential equations describing the transport phenomena, e.g. the Navier-Stokes equations. Especially for laminar flows, these codes can produce accurate results for Knudsen numbers up to 0.01, but start deviating from reality for higher Kn. It is generally accepted that the range of applicability of these continuum codes can be extended into the rarefied regime up to $\text{Kn} \approx 0.1$ by using special boundary conditions to take into account the possibility of a velocity slip or temperature jump at a surface [2]. In this method, however, the precise formulation of the slip velocity and temperature jump boundary conditions is strongly geometry dependent [3; 4; 5].

Gas flows with $\text{Kn} > 10$ are called "free molecular flows". In this regime, intermolecular collisions rarely occur and the flow is completely dominated by the interaction between the gas and the walls. Gas flows in the free molecular regime can be simulated using Molecular Dynamics (MD) or ballistic models.

In the intermediate ($0.01 < \text{Kn} < 10$) or rarefied regime, both collisions with solid surfaces and other gas molecules are important, and therefore have to be included in the simulation to obtain an accurate result. The Direct Simulation Monte Carlo (DSMC) method as developed by Bird [6] is the only practical engineering method that can be used in the transitional regime. The DSMC method is also valid in free molecular and continuum regimes, although the computational expenses become very large in the latter case. Its computational expenses, in fact, scale with Kn^{-4} and when the Knudsen number is less than ≈ 0.05 , they become inadmissible.

In summary, one can simulate gas flows with $\text{Kn} < 0.01$ (or, with modifications of boundary conditions < 0.1) using continuum based CFD models, and gas flows with $\text{Kn} > 0.05$ with particle based DSMC methods. In many practical applications, however, gas flows undergo spatial and/or temporal transitions from low (< 0.05) to high (> 0.05) Kn numbers, e.g. due to varying pressure or dimensions.

Different solutions have been proposed to compute flows undergoing such transitions. The best method is to use a hybrid continuum/molecular model to couple continuum solvers and molecular methods, for instance: MD and N-S equations [7], Boltzmann and N-S equations [8], DSMC and Stokes equations [9], DSMC and incompressible N-S equations [10], DSMC and Euler equations [11] and DSMC and N-S equations [12; 13; 14; 15; 16].

1.1.2 Thin film deposition based on an expanding thermal plasma

In the group of Prof. Van de Sanden at Eindhoven University of Technology, the so called remote Expanding Thermal arc Plasma (ETP) source has been developed [17]. A thermal plasma is generated at a relatively high pressure ($P_{in} \approx 0.1 - 0.6$ bar). The plasma jet rapidly expands into a low pressure chamber ($P_{out} \approx 10 - 100$ Pa). Starting from the plasma source, the plasma first supersonically expands and then quickly compresses through a stationary shock wave (figure 1.1).

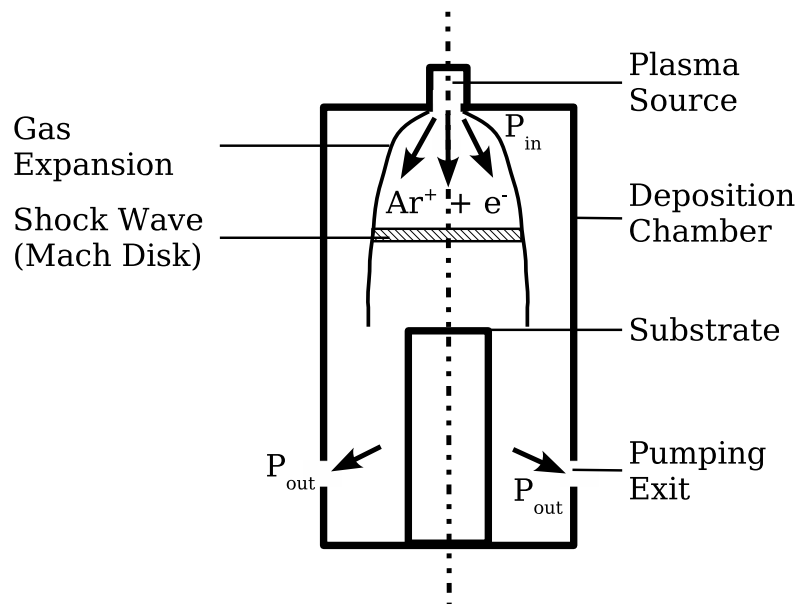


Figure 1.1: Reactor geometry.

Reactive precursor gas species are injected into the jet, that react with the ions and electrons from the plasma to form radical species. Upon impact with the substrate surface that is placed in the reactor, these radicals react to grow a thin solid film.

The application of plasma assisted deposition processes as described above has many potential advantages, such as high deposition rates at low substrate temperatures and good opportunities for "in situ" doping. Therefore it is of great interest in micro-electronics, coating technology and manufacture of LCD (Liquid Cristal Display) screens.

In order to optimize the deposition process, one needs information about the gas dynamic properties of the expanding jet flow. Although there been several studies

devoted to supersonic plasma expansion [18; 19; 20; 21; 22; 23; 24; 25; 26; 27; 28], full understanding of the processes governing the flow has not been reached jet.

In particular, it is not still completely clear how important is the influence of the rarefaction effects on the dynamics of the flow and if they must be taken into account in modelling the flow field. For example, it was supposed that, because of the rarefaction, the supersonic part of the flow is not protected by the shock that becomes transparent to the background molecules. These molecules could, therefore, invade the supersonic part of the jet, influencing the flow properties [21].

Computer simulations can be of great help to understand those phenomena, but conventional fluid dynamics simulations cannot be applied here because of the transition from continuum to rarefied flow.

1.2 Continuum-rarefied transition in supersonically expanding plasma

In order to better understand the flowfield inside the reactor, and most of all if the flow undergoes to a transition from the continuum to the rarefied regime, some preliminary calculations were performed with the commercial continuum CFD code FLUENT [29]. The code is capable of solving both subsonic and supersonic problems.

1.2.1 The reactor

The experimental set-up in which the expanding thermal plasma jet is created has been extensively described elsewhere [30]. Here only a short description is given. A cascaded arc, operating at sub-atmospheric pressure (0.1 – 0.6 bar), produces a thermal Argon plasma (source temperature $T_s \approx 0.8$ eV) that expands through a nozzle into a vessel at low pressure, typically 10 – 100 Pa. The total power given to the arc varies from 2 to 5 kW. The arc consists of four parallel insulated plates at some distance from each other, each with a 3 mm diameter hole. In this way a channel of 40 mm length is created. Three cathodes are positioned concentrically around the channel. The last plate, in which the nozzle is placed, acts as the anode. The nozzle has a straight channel with a diameter of 4 mm and a length of 10 mm. The last part of the nozzle makes an angle of 45° with the channel. The deposition chamber is a cylindrical stainless steel vessel with an inner radius $R_{\text{cham}} = 16$ cm and a length $L = 80$ cm.

1.2.2 The model

The modelled geometry and assumptions are identical to those used by Selezneva et al. [31; 32] with the exception that she was not considering the diverging part of

1.2. Continuum-rarefied transition in supersonically expanding plasma 5

the nozzle.

A 2D-axisymmetric flow was studied. The domain consists of two cylinders and a truncated cone (figure 1.2).

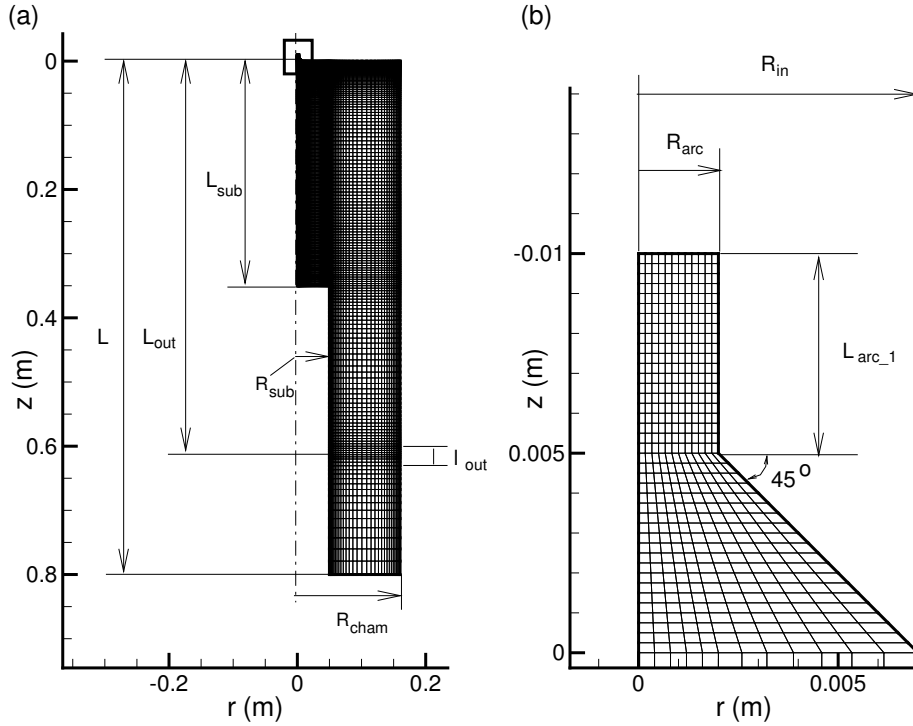


Figure 1.2: Reactor geometry and mesh. Overall geometry (a), zoom of the arc nozzle (b).

The first cylinder represents a part of the arc flow channel with radius of $R_{arc} = 2$ mm and length $L_{arc_1} = 5$ mm. The truncated cone represents the last diverging part of the nozzle where the side walls makes an angle of 45° with the axis. The second cylinder represents the expansion chamber, with radius $R_{cham} = 16$ cm and length $L = 80$ cm. The pumping exit, which is in reality a circular hole, in our two-dimensional model is represented as a circular slit in the reactor sidewall with a $l_{out} = 2$ cm width at a distance of $L_{out} = 60$ cm from the nozzle. The substrate is situated at $L_{sub} = 35$ cm from the chamber inlet and its radius is $R_{sub} = 5$ cm.

At the nozzle inlet, a pressure inlet boundary condition with a temperature $T_{nozzle} = 12000$ K and a pressure $P_{nozzle} = 0.2$ atm is imposed. Because deposition processes

are performed at a pressure ranging from 1 to 100 Pa, simulations were performed at four different pressures P_{out} in the pressure outlet: 1, 10, 20 and 100 Pa. At the wall a constant condition for the temperature was used ($T_w = 300$ K) and no-slip velocity boundary conditions. This is because we were not focusing on the near-wall flow, and so we did not set at the wall the physically more correct conditions of temperature jump and velocity slip.

In this model it was assumed that the gas is composed only of Argon atoms, neglecting the presence of electrons and ions. Also the effects of ionization and recombination on the flowfield were neglected. Because of the fact that the plasma is quenched in the expansion, both ionization and recombination are practically absent in the flow [32].

Even if the flow is partly supersonic, because the supersonic region is very small compared to the subsonic one, it was possible to solve the problem using a segregated technique. Since the flow is compressible and non-isothermal, also the energy equation was solved. The viscous heating is also taken into account. Temperature dependent viscosities and thermal conductivities are computed from kinetic theory [33].

The maximum velocity in the chamber, according to previous studies [31; 32], is about $V_{\text{max}} \approx 3000$ m/s. In the range of pressures considered (1 – 100 Pa), the Reynolds number with respect to the chamber diameter is smaller than 1800 and the flow is assumed to be laminar.

The mesh (figure 1.2) is a structured grid of 9540 quadrilateral cells. The cell size depends on the position in the chamber: it is small in the supersonic part of the expansion and within the high velocity jet region, and then it increases far from the axis. The solver used is a first-order upwind scheme. Since the pressure around the inlet quickly decreases from 20000 Pa down to 1 – 100 Pa, the simulation conditions are very stiff and it was not possible to reach the convergence with a second-order scheme. On the other hand we are interested now only in getting a preliminary solution and a qualitative view of the flow field and of the continuum-rarefied flow regime transition. For this reason we can consider the first-order upwind scheme sufficiently accurate for the moment. Convergence is supposed to be reached when residuals of all the equations become less than 10^{-5} . The use of a more strict convergence criterion, with maximum residuals of 10^{-10} , led to changes in the solution which were below 5%. The computation was also repeated on a grid with 20947 cells that was adaptively refined with respect to the density gradient; the difference in the results was less than 3%.

1.2. Continuum-rarefied transition in supersonically expanding plasma 7

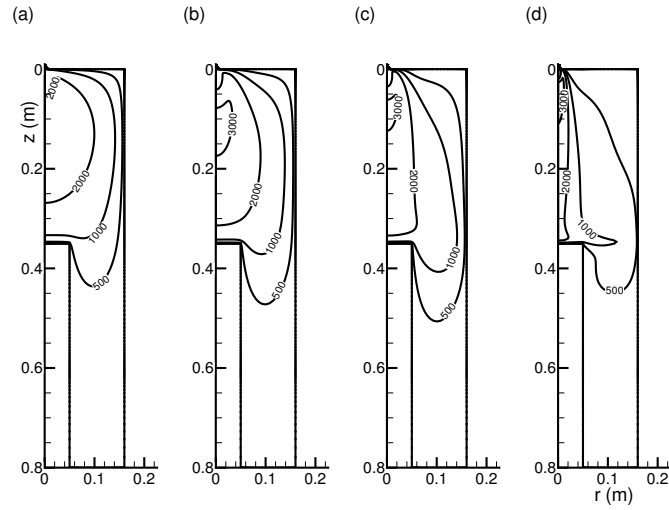


Figure 1.3: Static temperature (K) in the deposition chamber for 1 Pa (a), 10 Pa (b), 20 Pa (c) and 100 Pa (d) chamber pressure.

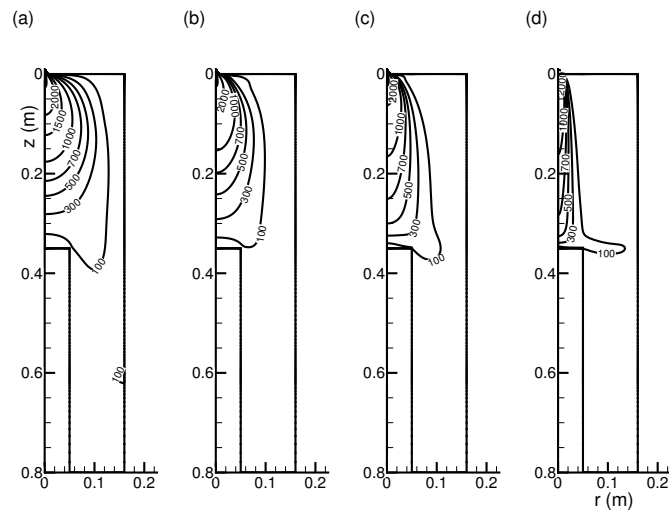


Figure 1.4: Velocity (m/s) in the deposition chamber for 1 Pa (a), 10 Pa (b), 20 Pa (c) and 100 Pa (d) chamber pressure.

1.2.3 The flowfield

All the result shown in this section are in very good agreement with those reported by Selezneva et al.[31; 32], the only difference noticed is that in our simulations FLUENT predicted a higher maximum Mach number in the expansion. The reason of that is that Selezneva et al. did not consider the diverging part of the nozzle, but they modelled it as a straight nozzle. Because the Mach number at the inlet is $M \approx 1$, the diverging part of the nozzle promotes the expansion, and so it is possible to reach higher Mach numbers.

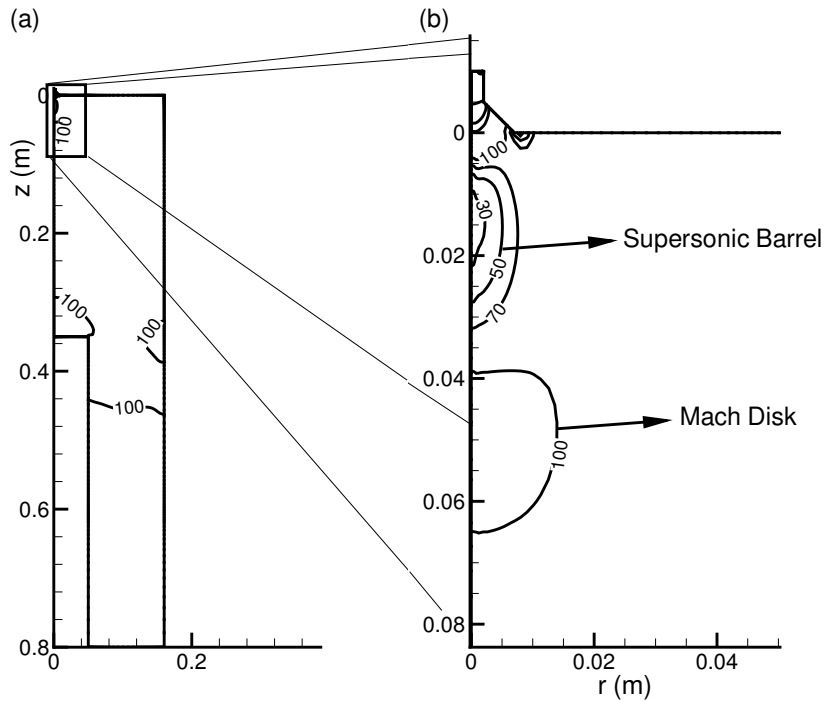


Figure 1.5: Pressure contours (Pa) in the chamber (a) and in the expansion-shock region (b) for the 100 Pa chamber pressure case.

Figures 1.3 and 1.4 show the temperature and velocity fields obtained for 1, 10, 20 and 100 Pa chamber pressures, respectively.

In all the cases, because of the low chamber pressure compared to the pressure in the discharge tube, the gas strongly expands. This strong expansion leads to the

1.2. Continuum-rarefied transition in supersonically expanding plasma 9

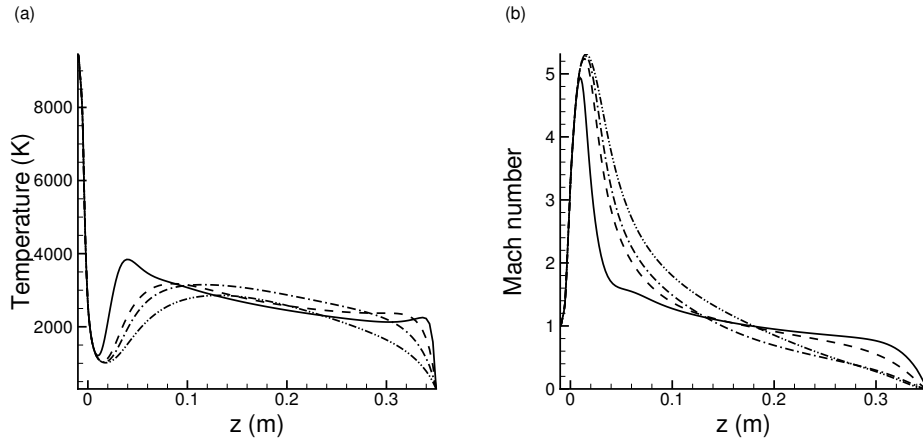


Figure 1.6: Temperature (a) and Mach number (b) profiles along z-axis at 1 Pa ($- \cdot -$), 10 Pa ($- \cdot -$), 20 Pa ($- -$), 100 Pa ($-$) chamber pressure.

formation of the jet structure with a supersonic barrel ended by a stationary normal shock wave (Mach disk), which is followed by a subsonic mixing and relaxing region. In order to better describe this structure, in figure 1.5, only for the 100 Pa chamber pressure case, we also show the pressure field in the deposition chamber focusing especially on the expansion-shock region. In this picture both the supersonic barrel and the Mach disk are clearly evident.

Comparing the four cases in figure 1.4 it is evident that the expansion becomes stronger and stronger as the chamber pressure decreases. For this reason, the jet thickness increases as the chamber pressure decreases until it fills the entire deposition chamber in the case at 1 Pa chamber pressure.

In figure 1.6 the temperature and Mach number profiles along the symmetry axis are shown.

As we reduce the pressure in the outlet, the strength of the expansion increases, increasing the maximum Mach number from almost 5 at 100 Pa to almost 5.4 at 1 Pa chamber pressure (figure 1.6(b)). Because of rarefaction effects, flow gradients reduce and consequently, the shock wave moves forward along the z-axis reducing its strength and increasing its thickness from 2.4 cm at 100 Pa to almost 10 cm at 1 Pa chamber pressure (figure 1.6(a)).

1.2.4 The continuum-rarefied flow transition

In order to predict the transition from the continuum to the rarefied flow regime it is necessary to evaluate the Knudsen number. In particular, in this analysis we use the Kn number based on the temperature gradient length scale

$$\text{Kn}_T = \frac{\lambda}{T} |\nabla T| \quad (1.2)$$

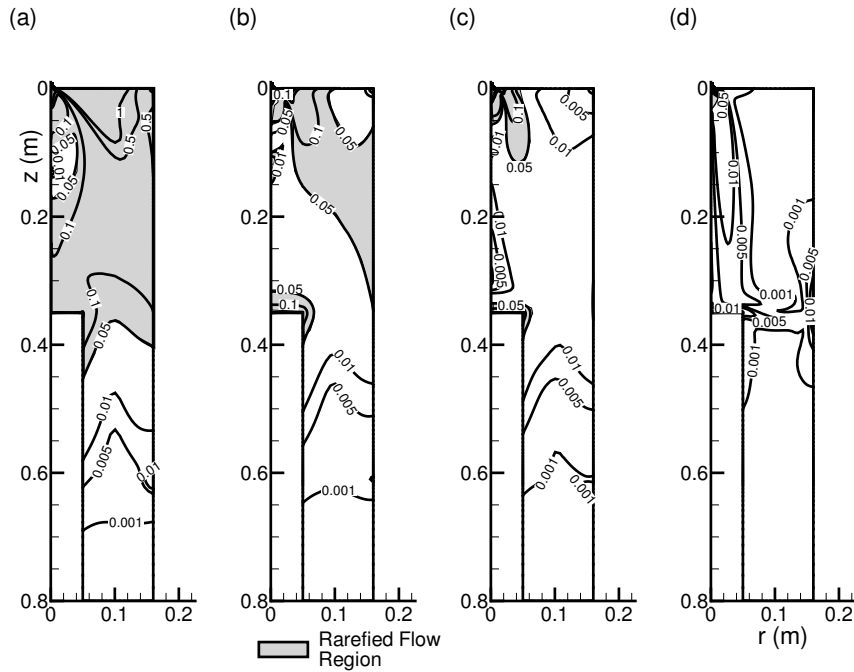


Figure 1.7: Knudsen number in the deposition chamber for 1 Pa (a), 10 Pa (b), 20 Pa (c) and 100 Pa (d) chamber pressure.

In figure 1.7 we report Kn_T in the entire domain for 1 Pa, 10 Pa, 20 Pa and 100 Pa chamber pressures. In the pictures we indicate in gray the region where it is not correct to use continuum hypothesis ($\text{Kn}_T > 0.05$). It can be clearly seen how this region grows as the chamber pressure decreases. At 100 Pa there is only a very tiny non-continuum region close to the inlet. At 20 Pa while this first region starts to grow, a second one starts to appear close to substrate. At 10 Pa both the non-continuum

regions are already very big and, finally, they invade almost $\frac{2}{3}$ of the entire domain at 1 Pa. Thus, our conclusion is that, already at 20 Pa the non-continuum region is big enough to possibly influence the flow field in the entire domain.

In figure 1.8 the Kn_T profiles along the z -axis are shown. Also from this picture it is clear that, because the rarefied region grows when we reduce the pressure, it is not possible to use a continuum model in the entire domain at low pressure conditions.

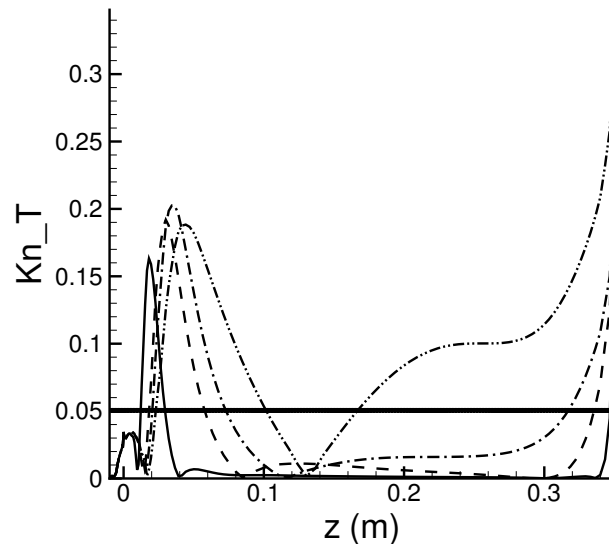


Figure 1.8: Knudsen number Kn_T profiles along the z -axis at 1 Pa ($- \cdot - \cdot -$), 10 Pa ($- \cdot \cdot -$), 20 Pa ($- -$), 100 Pa ($-$) chamber pressure.

1.3 Motivation and aim

The aim of the project described in this thesis was the development of a comprehensive simulation model for the gas flow dynamics in thin film deposition processes based on the application of an expanding thermal plasma.

From the previous section it is clear that it is not possible to model those kind of processes without taking into account the continuum-rarefied transition which the flow undergoes.

This thesis describes, therefore, the development, validation and application to thin

film deposition processes of a general purpose hybrid CFD/DSMC code thought to handle every kind of flow regime from the continuum to the free molecular one.

1.4 Rarefied flow simulations in the Department of Multi-Scale Physics

Prof. Kleijn's team at the Multi-Scale Physics Department (part of the Applied Sciences faculty of the Delft University of Technology) is working on multi-scale, multi-physics simulations of reactive flow systems, combining molecular and continuum based modelling techniques into hierarchical models for the various physical and chemical phenomena that interact at widely varying length and time scales. There is a large expertise in modelling reactive gas flow dynamics, both in the rarefied, transitional and continuum regimes, through DSMC [34], and CFD [35] techniques. To date, 4 PhD candidates have been working on the development of a DSMC code and on the study of rarefied gas flow problems. This does not only include low pressure simulations (e.g. vacuum equipment as used in Chemical Vapor Deposition applications), but also microfluidics applications (e.g. microthrusters).

The team is one of the relatively small number of groups worldwide that is involved in research of internal rarefied gas flows and has also a worldwide reputation for its modelling of thin film deposition processes [36; 37].

1.5 Thesis outline

The thesis is organized as follows.

Chapter 2 describes the details and the validation of the Navier-Stokes solver and the DSMC method.

In chapter 3, the hybrid CFD/DSMC approach is presented and validated. More specifically, in this chapter we describe how the models of the previous chapter 2 are dynamically coupled through a Schwarz method. The description of its advantages with respect to other methods, its limitations and a sensitivity analysis of the method to various parameters are also presented.

In chapter 4 the multi-scale hybrid CFD/DSMC approach is used to simulate a supersonic gas expansion for thin film deposition processes. Two different test conditions are considered. The comparison among hybrid simulation results, full CFD simulations and experimental data demonstrates the influence of rarefaction effects on both velocity and temperature fields. A full two-dimensional characterization of the supersonic gas expansion is presented.

Finally, in chapter 5 the most important conclusions from the thesis are summarized.

1.6 Acknowledgment

The idea for this project arose from discussions with Prof. Daan Schram and Richard van de Sanden of Eindhoven University of Technology. Their inspiration, continued interest and contributions to especially chapter 4 of this thesis are gratefully acknowledged.

Financial support for this project was provided by the Delft Centre for Computational Science and Engineering (DCSE). During this work, the author was a member of the J.M.Burgers Centre Research School for Fluid Mechanics (JMBC). The support of these organizations is gratefully acknowledged.

2. Numerical methods

As described in the previous chapter, the aim of this thesis is to describe the development, validation and application to thin film deposition processes of a general purpose hybrid CFD/DSMC code thought to handle every kind of flow regime from the continuum to the free molecular one.

In this chapter we first demonstrate how and under which conditions the Navier-Stokes equations can approximate the Boltzmann equation in section 2.1. Then, we describe a finite volume based scheme for explicit time integration of the compressible Navier-Stokes equations in low Kn flows in section 2.2 and a discrete, particle based Monte Carlo approach for solving the Boltzmann equations in high Kn flows in section 2.3.

The chapter has been partially published as chapter in 'Advanced Computational Method in Science and Engineering' [38], 'Hybrid Navier-Stokes/DSMC simulations of gas flows with rarefied-continuum transitions' by G. Abbate, B.J. Thijsse and C.R. Kleijn.

2.1 From Boltzmann to Navier-Stokes

The Navier-Stokes equations can be derived from the Boltzmann equation. The derivation can be found in most texts on kinetic theory, e.g. Bird [6], Chapman and Cowling [39], Grad [40], Patterson [41]. For the sake of completeness, the discussion is briefly repeated here.

Considering an ideal monatomic gas in the absence of external forces and assuming the gas sufficiently dilute for binary collision to dominate, the Boltzmann equation [1] reads

$$\frac{\partial(nf)}{\partial t} + c_k \frac{\partial(nf)}{\partial x_k} = \left[\frac{\partial(nf)}{\partial t} \right]_{\text{coll}} \quad (2.1)$$

where n is the number density, f is the velocity distribution function, c_k the molecular velocity in an inertial frame, the repeated index k denotes a sum, and the right-hand side represents the collision integral. Multiplying the Boltzmann equation by any function of molecular velocity $Q(c_i)$ and integrating over velocity space, the moment

equations are obtained

$$\frac{\partial(n \langle Q \rangle)}{\partial t} + \frac{\partial}{\partial x_k}(n \langle c_k Q \rangle) = \Delta[Q] \quad (2.2)$$

In equation 2.2, the operators $\langle Q \rangle$ and $\Delta[Q]$ are defined by

$$\langle Q \rangle = \int_{-\infty}^{\infty} \int_{-\infty}^{\infty} \int_{-\infty}^{\infty} Q f dc_1 dc_2 dc_3 \quad (2.3)$$

and

$$\Delta[Q] = \int_{-\infty}^{\infty} \int_{-\infty}^{\infty} \int_{-\infty}^{\infty} Q \left[\frac{\partial(nf)}{\partial t} \right]_{\text{coll}} dc_1 dc_2 dc_3 \quad (2.4)$$

Choosing one of the five collisional invariants $Q^{INV} = m\{1, c_i, c^2/2\}$, with m the molecular mass and c^2 the square of the velocity magnitude, as the arbitrary function of molecular velocity $Q(c_i)$, then the corresponding moment of the collision integral is identically zero, i.e. $\Delta[Q] = 0$. This general result is valid for any distribution function f and for any molecular interaction law and it leads to the conservation laws for gas dynamics

$$\frac{\partial}{\partial t}(n \langle Q^{INV} \rangle) + \frac{\partial}{\partial x_k}(n \langle c_k Q^{INV} \rangle) = 0 \quad (2.5)$$

Considering the collisional invariants in turn, the following set of equations can be written

$$\frac{\partial}{\partial t}(\rho) + \frac{\partial}{\partial x_k}(\rho \langle c_k \rangle) = 0 \quad (2.6)$$

$$\frac{\partial}{\partial t}(\rho \langle c_i \rangle) + \frac{\partial}{\partial x_k}(\rho \langle c_k c_i \rangle) = 0 \quad (2.7)$$

$$\frac{\partial}{\partial t}(\rho \langle c^2/2 \rangle) + \frac{\partial}{\partial x_k}(\rho \langle c_k c^2/2 \rangle) = 0 \quad (2.8)$$

where $\rho = mn$ is the mass density.

In terms of the thermal velocity components $C_i = (c_i - u_i)$, where the mean or fluid velocity is $u_i = \langle c_i \rangle$, the central moments can be defined

$$P_{ij} = \rho \langle C_i C_j \rangle \quad (2.9)$$

$$p = P_{kk}/3 \quad (2.10)$$

$$\tau_{ij} = -P_{ij} + p\delta_{ij} \quad (2.11)$$

$$e = \langle C^2/2 \rangle \quad (2.12)$$

$$q_i = \rho \langle C_i C^2/2 \rangle \quad (2.13)$$

where P_{ij} is the stress tensor, p is the pressure, τ_{ij} is the viscous stress tensor, e is the internal energy (translational) for a monoatomic gas, q_i is the heat flux vector for a monoatomic gas and δ_{jk} the Kronecker delta. Substituting equations 2.9-2.13 into the equations 2.6-2.8, the conservation laws for gas dynamics can then be written in the form

$$\frac{\partial}{\partial t}(\rho) + \frac{\partial}{\partial x_k}(\rho u_k) = 0 \quad (2.14)$$

$$\frac{\partial}{\partial t}(\rho u_i) + \frac{\partial}{\partial x_k}(\rho u_k u_i - \tau_{ki} + p \delta_{ki}) = 0 \quad (2.15)$$

$$\frac{\partial}{\partial t} \left[\rho \left(e + \frac{u^2}{2} \right) \right] + \frac{\partial}{\partial x_k} \left[\rho u_k \left(e + \frac{u^2}{2} \right) - \tau_{ki} u_i + p \delta_{ki} u_i + q_k \right] = 0 \quad (2.16)$$

For axi-symmetric flows in cylindrical coordinates (r, θ, z) , with $u_\theta = \frac{\partial}{\partial \theta} = 0$, the equations 2.14-2.16 can be rewritten as

$$\frac{\partial}{\partial t}(\rho) + \frac{\partial}{\partial r}(\rho u_r) + \frac{\rho u_r}{r} + \frac{\partial}{\partial z}(\rho u_z) = 0 \quad (2.17)$$

$$\begin{aligned} \frac{\partial}{\partial t}(\rho u_r) + \frac{\partial}{\partial r}(\rho u_r^2 + p - \tau_{rr}) + \frac{\rho u_r^2 - \tau_{rr}}{r} + \frac{\partial}{\partial z}(\rho u_r u_z - \tau_{rz}) + \\ + \frac{\tau_{\theta\theta}}{r} = 0 \end{aligned} \quad (2.18)$$

$$\frac{\partial}{\partial t}(\rho u_z) + \frac{\partial}{\partial r}(\rho u_r u_z - \tau_{rz}) + \frac{\rho u_r u_z - \tau_{rz}}{r} + \frac{\partial}{\partial z}(\rho u_z^2 + p - \tau_{zz}) = 0 \quad (2.19)$$

$$\begin{aligned} \frac{\partial}{\partial t} \left[\rho \left(e + \frac{u^2}{2} \right) \right] + \frac{\partial}{\partial r} \left[\rho u_r \left(e + \frac{u^2}{2} \right) + p u_r - \tau_{rr} u_r - \tau_{rz} u_z + q_r \right] + \\ + \frac{1}{r} \left[\rho u_r \left(e + \frac{u^2}{2} \right) + p u_r - \tau_{rr} u_r - \tau_{rz} u_z + q_r \right] + \frac{\partial}{\partial z} \left[\rho u_z \left(e + \frac{u^2}{2} \right) + \right. \\ \left. + p u_z - \tau_{rz} u_r - \tau_{zz} u_z + q_z \right] = 0 \end{aligned} \quad (2.20)$$

For polyatomic gases the above procedure is not valid anymore and, therefore, must be modified. The problem is rather difficult, because it includes the question of what equation replaces equation 2.1, and it becomes necessary to make use of a suitable approximation.

The energy $mc^2/2$ does not properly account for the amount of energy that is carried by a particle with internal structure, and it must be replaced by $(mc^2/2 + \varepsilon)$, where ε is the additional internal energy per particle. Therefore, the collisional invariants become

$$Q^{INV} = \{m, mc_i, (mc^2/2 + \varepsilon)\} \quad (2.21)$$

Assuming that equation 2.1 continues to hold for the extended distribution function $f(c_i, \varepsilon)$, when applying to both equations 2.3 and 2.4, an additional integral over

ε is required. The quantities in equation 2.21 must continue to be conserved in a collision, and consequently, equation 2.4 still evaluates to zero; thus, equation 2.5 remains unchanged.

Since integration over ε can be taken first and independently from the c_i integration, evaluating the left hand side of equation 2.5, identical results to those obtained for the monoatomic gas will be found for all quantities that contain polynomials in c_i alone. Therefore equations 2.6 and 2.7 and, consequently, 2.14 and 2.15 are fully recovered. The same conclusion also applies to the first term in the quantity $(mc^2/2 + \varepsilon)$ and so, equation 2.8 is replaced by

$$\frac{\partial}{\partial t}(\rho \langle c^2/2 \rangle + n \langle \varepsilon \rangle) + \frac{\partial}{\partial x_k}(\rho \langle c_k c^2/2 \rangle + n \langle c_k \varepsilon \rangle) = 0 \quad (2.22)$$

The unknown term $me_{int} = \langle \varepsilon \rangle$ is the additional internal energy. A simple approach is to assume that all internal molecular energy modes are in equilibrium, both internally and with the translational degrees of freedom. Thus, e_{int} can be expressed in terms of the translational temperature T by the equilibrium relation

$$e_{int} = \frac{1}{2} \left(\frac{5 - 3\gamma}{\gamma - 1} \right) RT \quad (2.23)$$

with R the gas constant and where the additional internal energy is accounted for through the introduction of the ratio of specific heats γ . Clearly, in the case of a monoatomic gas the additional internal energy evaluates to zero, i.e. $e_{int} = 0$.

If we substitute equations 2.9-2.13 into equation 2.5 we will get once again equations 2.14 and 2.15, but instead of 2.16 it will lead to

$$\begin{aligned} & \frac{\partial}{\partial t} \left[\rho \left(e + e_{int} + \frac{u^2}{2} \right) \right] + \\ & + \frac{\partial}{\partial x_k} \left[\rho u_k \left(e + e_{int} + \frac{u^2}{2} \right) + P_{ki} u_i + q_k + (n \langle C_k \varepsilon \rangle) \right] = 0 \end{aligned} \quad (2.24)$$

However, if we replace equation 2.12 with

$$e = (\langle C^2/2 \rangle + e_{int}) \quad (2.25)$$

and 2.13 with

$$q_i = \rho \langle C_i C^2/2 \rangle + n \langle C_i \varepsilon \rangle \quad (2.26)$$

we will recover equation 2.16 as well.

We conclude that, if definitions 2.25 and 2.26 are employed in the case where the gas possesses internal structure and a state of equilibrium exists between the internal modes and the translational degrees of freedom, equations 2.14-2.16 can be used.

The set of conservation equations 2.14-2.16 can be developed for any general fluid

through the use of phenomenological arguments alone and, therefore, is more general than the kinetic theory derivation would indicate. Since we are only interested in treating an ideal gas flow, however, the kinetic theory approach is necessary because it shows that the obtained set of equations is valid for any degree of translational nonequilibrium, that is, for any translational velocity distribution function one cares to consider. In case of the equilibrium distribution, namely the Maxwellian distribution f^{Max} [2; 42], then the set becomes the Euler equations, because viscous stress and heat flux are identically zero in this case. On the contrary if one chooses a Chapman-Enskog (CE) distribution f^{CE} [39; 43; 44], then the set becomes the Navier-Stokes equations.

The CE distribution is an approximate solution of the Boltzmann equation (for a simple gas) and is expressed as a product of a local Maxwellian and a polynomial function of the thermal velocity components C_i

$$f^{CE} = f^{Max}(1 + \phi_1 + \phi_2) \quad (2.27)$$

where

$$f^{Max} = (2\pi RT)^{-3/2} \exp(-C^2/2RT) \quad (2.28)$$

$$\phi_1 = -\left(\frac{\rho}{p^2}\right) \left(K^{(1)} \frac{\partial T}{\partial x_k}\right) C_k (C^2/5RT - 1) \quad (2.29)$$

$$\phi_2 = -\left(\frac{\rho}{p^2}\right) \left(\mu^{(1)} \frac{\partial u_j}{\partial x_k}\right) \left(C_j C_k - \frac{1}{3} C^2 \delta_{jk}\right) \quad (2.30)$$

with $K^{(1)}$ the coefficient of thermal conductivity, $\mu^{(1)}$ the coefficient of viscosity as determined by the first-order Chapman-Enskog procedure, $C^2 = C_k \cdot C_k$, and δ_{jk} the Kronecker delta. When f^{CE} is chosen, the stress and the heat flux are given by the corresponding Chapman-Enskog expressions

$$q_i^{CE} = -K^{(1)} \frac{\partial T}{\partial x_i} \quad (2.31)$$

$$\tau_{ij}^{CE} = \mu^{(1)} \left(\frac{\partial u_i}{\partial x_j} + \frac{\partial u_j}{\partial x_i} \right) - \frac{2}{3} \mu^{(1)} \left(\frac{\partial u_k}{\partial x_k} \right) \delta_{ij} \quad (2.32)$$

For axi-symmetric flow, in a (r, θ, z) cylindrical reference system, equation 2.32 becomes

$$\tau_{rr} = \mu^{(1)} \left[2 \frac{\partial u_r}{\partial r} - \frac{2}{3} \left(\frac{\partial u_r}{\partial r} + \frac{u_r}{r} + \frac{\partial u_z}{\partial z} \right) \right] \quad (2.33)$$

$$\tau_{\theta\theta} = \mu^{(1)} \left[\frac{2u_r}{r} - \frac{2}{3} \left(\frac{\partial u_r}{\partial r} + \frac{u_r}{r} + \frac{\partial u_z}{\partial z} \right) \right] \quad (2.34)$$

$$\tau_{zz} = \mu^{(1)} \left[2 \frac{\partial u_z}{\partial z} - \frac{2}{3} \left(\frac{\partial u_r}{\partial r} + \frac{u_r}{r} + \frac{\partial u_z}{\partial z} \right) \right] \quad (2.35)$$

$$\tau_{rz} = \mu^{(1)} \left(\frac{\partial u_z}{\partial r} + \frac{\partial u_r}{\partial z} \right) \quad (2.36)$$

In summary, the conservation equations 2.14-2.16 are not the N-S equations until one introduces f^{CE} . In fact, one is free to choose any translational velocity distribution function in the equation 2.5 or in the sets of equations 2.6-2.8 and 2.14-2.16, and in this way the set becomes closed, as long as f is fully specified. Otherwise, if f remains general, one is faced with a closure problem, because τ_{ij} and q_i are unknown quantities.

Since f^{CE} is an $O(\text{Kn})$ expansion of the exact solution of f , the resulting N-S equations are an accurate approximation for $\text{Kn} \ll 1$ only. For large Kn , solutions to the N-S equations no longer accurately describe the real behavior of the gas. This is most clearly visible through the occurrence of wall-slip and wall-temperature jumps at high Kn , neither of which is found through N-S.

2.2 Finite volume scheme for compressible Navier-Stokes equations

The aim of this section is to describe a Navier-Stokes solver that will be coupled to a DSMC (Direct Simulation Monte Carlo) algorithm, in order to create a hybrid solver for gas flows with temporal and spatial transitions from continuum to rarefied conditions.

The CROW-CFD (Continuum Rarefied flow - CFD) code developed in this work is a code for unsteady gas flow simulations based on a finite volume formulation in compressible form; steady-state conditions are reached by integrating the transient solution in time from $t = 0$ to the long-time steady solution. The code can solve 1-D, 2-D and 2-D axi-symmetric geometries. It uses an explicit, second-order, kinetic flux-splitting, MUSCL scheme for the Navier-Stokes equations [45; 46; 47]. This choice was based on the following arguments:

- Since DSMC has the characteristics of a time-dependent finite-volume scheme, compatibility suggests the use of the same scheme for the N-S portion.
- An explicit time integration scheme was used because it is more accurate. Although explicit schemes are generally more expensive than implicit schemes, it is expected that the most time consuming part of the simulations will be in the DSMC solver, and therefore the speed of the CFD solver is not critical.
- Because the DSMC method is based on kinetic theory, it is preferable that the same would be used for the definition of the split fluxes.

2.2.1 Finite volume discretization

Each of the five separate moment equations represented by either sets of equations 2.6-2.8 or 2.14-2.16 can be expressed through the form

$$\frac{\partial U}{\partial t} + \frac{\partial F_k}{\partial x_k} = 0 \quad (2.37)$$

Using the notation of equation 2.5

$$U = n \langle Q^{INV} \rangle \quad (2.38)$$

is the state vector, and

$$F_n = n \langle c_n Q^{INV} \rangle \quad (2.39)$$

the total flux vector, with c_n the component of the molecular velocity normal to the planar surface.

Finite volume integration of the above model equation over an arbitrary control volume V , and using Gauss' divergence theorem leads to

$$\frac{\partial}{\partial t} \int_V U dV + \int_S F_n dS = 0 \quad (2.40)$$

where S encloses the volume V and F_n is the projection of F_i onto the unit outward pointing normal for the surface element dS .

Considering a Cartesian grid, equation 2.40 can be written as

$$\Delta V \frac{\partial \vec{U}_{ijk}}{\partial t} = (-\vec{F} \Delta A) \Big|_{i-1/2,j,k}^{i+1/2,j,k} + (-\vec{F} \Delta A) \Big|_{i,j-1/2,k}^{i,j+1/2,k} + (-\vec{F} \Delta A) \Big|_{i,j,k-1/2}^{i,j,k+1/2} \quad (2.41)$$

where e.g. $(\cdot) \Big|_{i-1/2,j,k}^{i+1/2,j,k} = (\cdot)_{i+1/2,j,k} - (\cdot)_{i-1/2,j,k}$ and x_1, x_2 and x_3 are the spatial coordinates in the directions i, j and k respectively, ΔV and \vec{U} are the volume and state variables averaged in the i^{th} cell, ΔA and \vec{F} are the area and the averaged total flux on the relevant cell face.

2.2.2 Time discretization

The finite volume integration of equation 2.41 over a control volume V must be augmented with a further integration over a finite time step Δt . Considering a first order accurate Euler forward time integration, the 1-D version of equation 2.41 reads

$$\Delta V (\vec{U}_i^{n+1} - \vec{U}_i^n) = \int_t^{t+\Delta t} (-\vec{F} \Delta A) \Big|_{i-1/2}^{i+1/2} dt \quad (2.42)$$

where n refers at time t and $n + 1$ at time $t + \Delta t$. To evaluate the right hand side of the above equation we need to make an assumption. We could use the values at time t or at time $t + \Delta t$ to calculate the integral or, alternatively, a combination of both. We may generalize the approach by means of a weighting parameter θ between 0 and 1 and write the integral with respect to time as

$$\int_t^{t+\Delta t} (-\vec{F}\Delta A)\Big|_{i-1/2}^{i+1/2} dt = -\Delta t\Delta A \left[\theta \left(\vec{F}\Big|_{i-1/2}^{i+1/2} \right)^{n+1} + (1-\theta) \left(\vec{F}\Big|_{i-1/2}^{i+1/2} \right)^n \right] \quad (2.43)$$

The exact form of the eventual discretized equation depends on the value of θ . When θ is zero, only values at the old time t are used at the right hand side of the equation 2.42 to evaluate \vec{U} at the new time; resulting in an explicit scheme. When $0 < \theta < 1$ values at the new time level are used on both sides of the equation; the resulting schemes are called implicit. The extreme case of $\theta = 1$ is termed fully implicit and the case corresponding to $\theta = 0.5$ is called Crank-Nicolson scheme. The latter scheme is second-order accurate in time.

Here we considered a first-order explicit scheme in time which uses values at time t , and so equation 2.42 becomes

$$\vec{U}_i^{n+1} = \vec{U}_i^n - \frac{\Delta t}{\Delta V} \Delta A (\vec{F}_{i+1/2} - \vec{F}_{i-1/2})^n \quad (2.44)$$

2.2.3 The MUSCL discretization scheme

To solve equation 2.44 we must now evaluate the total flux on the relevant cell face $\vec{F}_{i+1/2}$ (and similar for other cell faces), that will be a function of the state variables U at the same cell interface

$$\vec{F}_{i+1/2} = F(U_{i+1/2}) \quad (2.45)$$

This means that we should estimate $F(U_{i+1/2})$ starting from state variables averaged in the grid cells \vec{U} . The flux spitting method consists in splitting the total flux in its positive and negative parts

$$\vec{F}_{i+1/2} = \vec{F}_{i+1/2}^+ + \vec{F}_{i+1/2}^- \quad (2.46)$$

where the positive and negative parts of the total flux will be functions of the state variables respectively at the left or right of the cell interface (figure 2.1)

$$\vec{F}_{i+1/2}^+ = F^+(U_{i+1/2}^L) \quad (2.47)$$

$$\vec{F}_{i+1/2}^- = F^-(U_{i+1/2}^R) \quad (2.48)$$

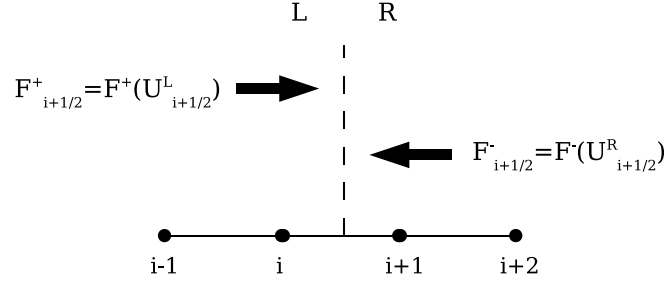


Figure 2.1: MUSCL Scheme

In the second-order spatially accurate MUSCL (Monotone Upstream-centered Scheme for Conservation Laws) scheme [48], the state variables left and right of the cell interface are approximated by

$$U_{i+1/2}^L = \vec{U}_i + \frac{1}{4} \left[(1-k)\Delta U_{i-1/2}^- + (1+k)\Delta U_{i+1/2}^+ \right] \quad (2.49)$$

$$U_{i+1/2}^R = \vec{U}_{i+1} - \frac{1}{4} \left[(1+k)\Delta U_{i-1/2}^- + (1-k)\Delta U_{i+1/2}^+ \right] \quad (2.50)$$

where

$$\Delta U_{i+1/2}^- = \text{limiter}(\Delta U_{i+1/2}, \beta \Delta U_{i+3/2}) \quad (2.51)$$

$$\Delta U_{i+1/2}^+ = \text{limiter}(\Delta U_{i+3/2}, \beta \Delta U_{i+1/2}) \quad (2.52)$$

with

$$\Delta U_{i+1/2} = \vec{U}_{i+1} - \vec{U}_i \quad (2.53)$$

and β is a compression parameter whose value is generally in the range

$$1 < \beta < \frac{3-k}{1-k} \quad (2.54)$$

In equations 2.51-2.52, "limiter" is a so-called flux-limiting function and it is used

in a second-order discretization scheme to control the amount of anti-diffusion on a first-order upwind approximation [49]. In particular in our code a value of $k = -1$ was chosen and we fixed $\beta = 1.5$. As flux-limiting "limiter" function in equations 2.51-2.52, the *minmod* function was implemented [49]

$$\text{limiter}(a, b) = \text{minmod}(a, b) = \begin{cases} a & \text{if } |a| < |b|; a \cdot b > 0 \\ b & \text{if } |a| > |b|; a \cdot b > 0 \\ 0 & \text{if } a \cdot b < 0 \end{cases} \quad (2.55)$$

2.2.4 Chapman-Enskog split fluxes

We need now to evaluate an expression for the one-side fluxes based on a fixed interface. This is done in a way proposed by Chou and Baganoff [46] and by Lou et al. [47]. The approach is briefly repeated here for the sake of completeness. From equation 2.39, introducing a Cartesian coordinate system $(n, t1, t2)$ with axes normal to and in two tangential directions of an arbitrary fixed planar surface, and replacing both the temperature gradient and the velocity-gradient tensor by the Chapman-Enskog expression for stress and heat flux [33]

$$q_i^{CE} = -K^{(1)} \frac{\partial T}{\partial x_i} \quad (2.56)$$

$$\tau_{ij}^{CE} = \mu^{(1)} \left(\frac{\partial u_i}{\partial x_j} + \frac{\partial u_j}{\partial x_i} \right) - \frac{2}{3} \mu^{(1)} \left(\frac{\partial u_k}{\partial x_k} \right) \delta_{ij} \quad (2.57)$$

we obtain

$$F_{mass}^{\pm} = \rho \sqrt{RT/2} [(1 \pm \alpha_1) S_n \pm \alpha_2 (1 - \chi_1)] \quad (2.58)$$

$$F_{n-mom}^{\pm} = p [(1 \pm \alpha_1) (S_n^2 + \frac{1}{2} (1 - \hat{\tau}_{nn}^{CE})) \pm \alpha_2 (S_n + \hat{q}_n^{CE})] \quad (2.59)$$

$$F_{t1-mom}^{\pm} = \sqrt{2RT} [S_{t1} F_{mass}^{\pm}] + \frac{1}{2} p [-(1 \pm \alpha_1) \hat{\tau}_{nt1}^{CE} \pm \alpha_2 \hat{q}_{t1}^{CE}] \quad (2.60)$$

$$F_{tr-energy}^{\pm} = p \sqrt{RT/2} [(1 \pm \alpha_1) (S_n (\frac{5}{2} + S^2) + \chi_2) \pm \alpha_2 (2 + S^2 + \chi_3)] \quad (2.61)$$

$$F_{int-energy}^{\pm} = (\Delta q_{Eucken}^{\pm} + \rho u_n e_{int}^{\pm}) = \frac{1}{2} \left(\frac{5 - 3\gamma}{\gamma - 1} \right) RT F_{mass}^{\pm} \quad (2.62)$$

$$F_{energy}^{\pm} = F_{tr-energy}^{\pm} + F_{int-energy}^{\pm} \quad (2.63)$$

where γ is the gas ratio of specific heats and

$$\alpha_1 = \operatorname{erf}(S_n) \quad (2.64)$$

$$\alpha_2 = \frac{1}{\sqrt{\pi}} e^{-S_n^2} \quad (2.65)$$

$$\chi_1 = S_n \hat{q}_n^{CE} + \frac{1}{2} \hat{\tau}_{nn}^{CE} \quad (2.66)$$

$$\chi_2 = \frac{5}{2} \hat{q}_n^{CE} - (S_n \hat{\tau}_{nn}^{CE} + S_{t1} \hat{\tau}_{nt1}^{CE} + S_{t2} \hat{\tau}_{nt2}^{CE}) \quad (2.67)$$

$$\chi_3 = S_{t1} \hat{q}_{t1}^{CE} + S_{t2} \hat{q}_{t2}^{CE} - \chi_1 (1 + S_{t1}^2 + S_{t2}^2) - \hat{\tau}_{nn}^{CE} \quad (2.68)$$

$$S_n = u_n / \sqrt{2RT} \quad (2.69)$$

$$S^2 = S_n^2 + S_{t1}^2 + S_{t2}^2 \quad (2.70)$$

$$\hat{\tau}_{nn}^{CE} = \tau_{nn}^{CE} / p \quad (2.71)$$

$$\hat{q}_n^{CE} = \frac{2}{5} q_n^{CE} / (p \sqrt{2RT}) \quad (2.72)$$

Since the individual component of S_i , $\hat{\tau}_{ij}$ and \hat{q}_i along the axis of the defined Cartesian coordinate system ($n, t1, t2$) are all nondimensionalized the same way, they are not all listed. It is interesting to note that we refer to the speed ratio $S = u / \sqrt{2RT}$ instead of the Mach number as frequently in use in kinetic theory. It is simple to check that if we sum the positive and negative parts, we will get once again the total fluxes

$$F_{mass} = \rho u_n \quad (2.73)$$

$$F_{n-mom} = \rho u_n^2 + p - \tau_{nn}^{CE} \quad (2.74)$$

$$F_{t1-mom} = \rho u_n u_{t1} - \tau_{nt1}^{CE} \quad (2.75)$$

$$F_{tr-energy} = \rho u_n \left(\frac{3}{2} RT + \frac{u^2}{2} \right) + p u_n - (\tau_{nn}^{CE} u_n + \tau_{nt1}^{CE} u_{t1} + \tau_{nt2}^{CE} u_{t2}) + q_n^{CE} \quad (2.76)$$

$$F_{int-energy} = (\Delta q_{Eucken} + \rho u_n e_{int}) = \frac{1}{2} \left(\frac{5 - 3\gamma}{\gamma - 1} \right) p u_n \quad (2.77)$$

2.2.5 Boundary conditions

In order to solve the equations described in the previous section, boundary conditions on the complete boundary of the simulated domain are needed. There are two principal ways to impose boundary conditions: Dirichlet [50] and Neumann [51] boundary conditions. The first consists of imposing to a variable ϕ its value ϕ_0 on

the boundary, whereas in the second the value of its gradient normal to the surface is imposed as $\partial\phi/\partial n = \phi'_0$.

By combining these two basic types of boundary conditions for pressure, velocity and temperature, a wide variety of possible boundary conditions has been implemented

- Isothermal walls,
- Walls with Neumann heat flux boundary condition, including adiabatic walls,
- Sliding walls,
- Porous walls,
- Walls with velocity slip and temperature jump for transitional regime,
- Symmetry axis,
- Mass flow inlet,
- Pressure inlet,
- Pressure outlet.

2.2.6 Validation

The developed CFD code (CROW-CFD) has been validated against both theoretical results and numerical results obtained with the commercially available code FLUENT [29].

The test cases have been chosen in order to validate and show the potentials of the code for steady and transient, compressible and incompressible, one-dimensional and multi-dimensional flows.

2.2.6.1 Sod's problem

We apply the CROW-CFD code to a transient one-dimensional shock-tube problem, or, as it is also known in the literature, Sod's problem [45; 48; 54; 55]. It is a classical test case for the validation of unsteady compressible CFD methods.

We model the flow field inside a $L = 1$ m long tube linking two tanks of the same fluid (air) under different thermodynamic conditions (figure 2.2). A membrane in the middle of the tube divides the two regions where the fluid is in different conditions: in the left region the gas is at a pressure $P_1 = 1$ atm with a density $\rho_1 = 1$ kg/m³, while in the right region it is at a pressure $P_2 = 0.1$ atm with a density $\rho_2 = 0.125$ kg/m³. At time $t = 0$ the membrane breaks and the fluid can flow from one region

2.2. Finite volume scheme for compressible Navier-Stokes equations 27

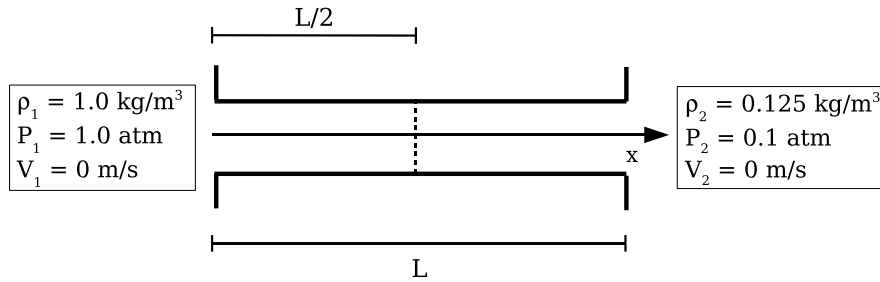


Figure 2.2: Sod's problem test case. The dashed line indicates the membrane which is broken at the instant $t = 0$.

to the other. Three different waves will start travelling in the tube with three different velocities: a rarefaction or expansion wave moving from right to left, a shock wave travelling from the left to the right and between them a contact discontinuity. The rarefaction wave produces a gradual decrease of density and pressure of the gas passing through it, while the shock wave produces a rapid increase of the density and pressure. Through the third one, the contact discontinuity, the flow undergoes only a density, and not a pressure, variation.

The grid is composed of 100 cells in the x direction and 1 cell in the y direction.

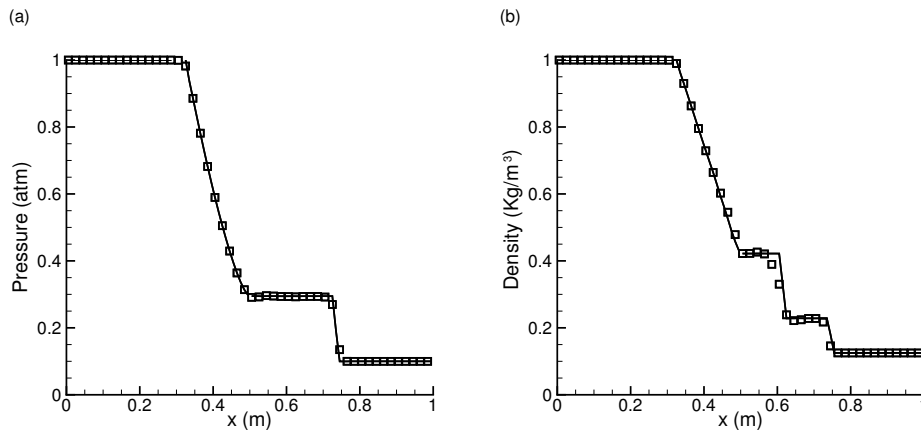


Figure 2.3: Sod's problem: pressure (a) and density (b) profiles in the tube. Theory (—), CROW-CFD (\square)

The results of simulated pressure and density profiles along the tube are compared with the theory in figure 2.3 at the instant where the shock wave moving to the right has approximately reached $x = 0.75$ m. It is clear that both for the pressure and density, the simulation profiles slightly differ from the theory. In the simulation profiles the two discontinuities are smoother than in the theory. The reason of these differences is that the theoretical solution is valid for non-viscous flows, while our code solves the Navier-Stokes equations and not the Euler equations. The effect of viscosity is clearly to reduce the strength of the shocks making them smoother. Considering this, it can be concluded that CROW-CFD performs very well in this validation case.

2.2.6.2 Poiseuille flow

In this section, we use the CROW-CFD code to simulate a plane Poiseuille flow (figure 2.4).

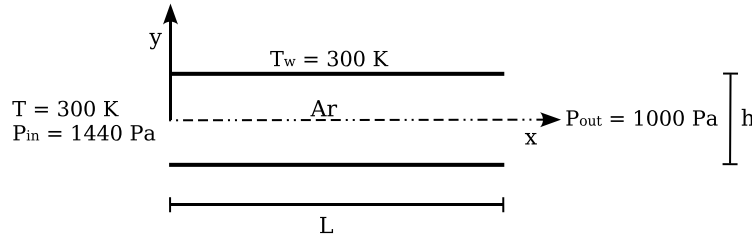


Figure 2.4: Poiseuille flow test case.

We consider a flow of Argon at a temperature $T = 300$ K in a channel of height $h = 0.001$ m and length $L = 100h$. The pressure at the inlet is $P_{in} = 1440$ Pa and at the outlet $P_{out} = 1000$ Pa. The wall temperature is $T_w = 300$ K. At a sufficiently large distance from the inlet the flow is a Poiseuille flow: its solution is known and characterized by a linear pressure decay in the x direction and a parabolic velocity profile in the y direction [56; 57]. For the studied flow, with Reynolds number $Re \approx 100$, the velocity profile will be fully developed for $\frac{x}{h} > 0.04Re = 4$. Because of symmetry we limit the simulation domain to the upper half of the channel. The grid is composed of 100 cells in the x direction and 10 cells in the y direction.

At the symmetry plane the velocity is

$$V_0 = \frac{\left(\frac{h}{2}\right)^2}{2\mu} \frac{\Delta P}{L} \approx 105 \text{ m/s} \quad (2.78)$$

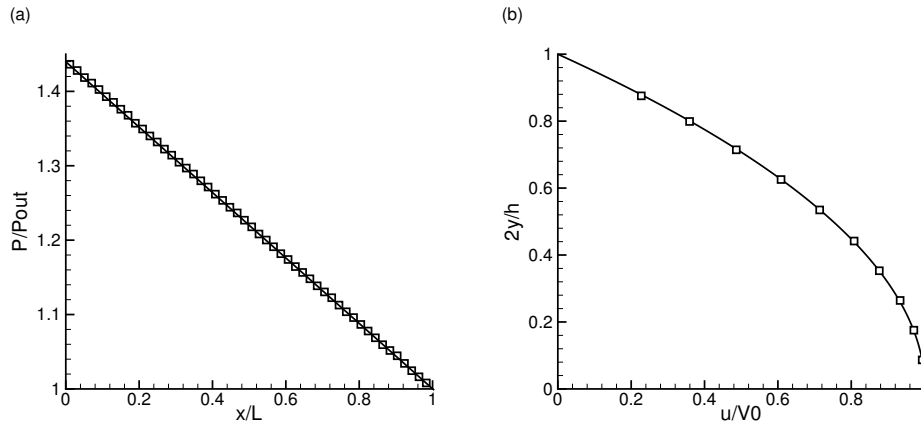


Figure 2.5: Poiseuille flow: pressure drop along the x axis (a) and velocity profile at $\frac{x}{h} = 80$ (b). Theory (—), CROW-CFD (\square)

with μ the viscosity of the fluid and $\Delta P = P_{in} - P_{out}$.

As shown in figure 2.5(a) the pressure drop along the x direction predicted by the CROW-CFD is in very good agreement with the theoretical linear pressure drop.

In figure 2.5(b) the velocity profile at $\frac{x}{h} = 80$ predicted by the CROW-CFD code is compared to the Poiseuille flow parabolic analytical solution.

From figure 2.5 it can be concluded that CROW-CFD code was performing very well also in this second test case.

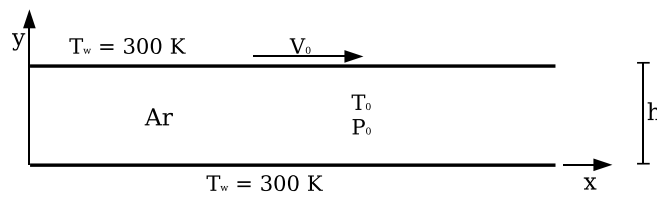


Figure 2.6: Couette flow test case.

2.2.6.3 Couette flow

Another classical test case is the incompressible Couette flow (figure 2.6) [58]. We consider a flow of Argon gas between two infinitely long parallel flat plates at a mutual distance $h = 0.005$ m. The bottom plate is at rest, while the upper one moves from left to the right with velocity $V_0 = 100$ m/s. The plates are at the same temperature of the gas $T_w = T_0 = 300$ K.

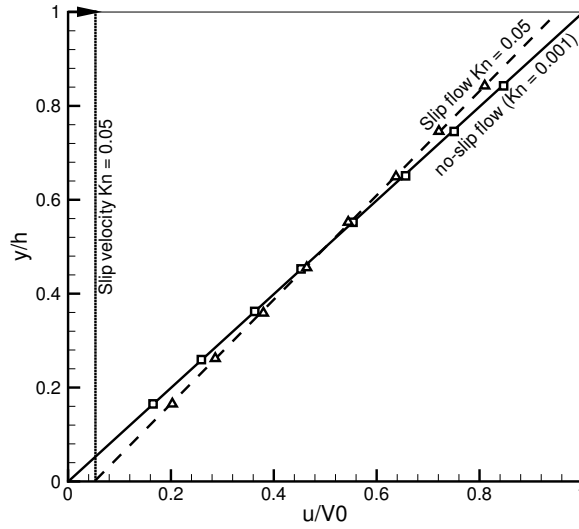


Figure 2.7: Couette flow: velocity profile at $x = 0.025$ m. Theory with no-slip BC (—), theory with slip velocity BC at $\text{Kn} = 0.05$ (---), CROW-CFD at $\text{Kn} = 0.001$ (\square), CROW-CFD at $\text{Kn} = 0.05$ (\triangle)

We consider two different values of Kn with respect to the distance between the plates h : $\text{Kn} = 0.001$ and $\text{Kn} = 0.05$. To vary Kn , two different conditions for the gas pressure P_0 are considered, respectively 500 Pa and 10 Pa. In the first case, the mean free path is $\lambda \approx 5 \cdot 10^{-6}$ m and, because we are in the continuum regime, no-slip boundary conditions are imposed at the wall, whereas in the second case the mean free path is $\lambda \approx 2.5 \cdot 10^{-4}$ m and a slip velocity is imposed at the wall according to [85]

$$V_{\text{slip}} = \lambda \left| \frac{du}{dy} \right| = \lambda \frac{V_0}{h} = \text{Kn} V_0 \approx 5 \text{ m/s} \quad (2.79)$$

where u the velocity component in the x direction.

The computational domain is extended for a length $L = 0.05 \text{ m} = 10 h$ in the x direction to avoid the influence of the boundaries at the center line $x = 0.025 \text{ m} = 5 h$. For this reason we expect to get a linear Couette flow velocity profile at this position. The grid is composed of 50 cells in the x direction and 10 cells in the y direction.

In figure 2.7 the velocity profiles at $x = 0.025 \text{ m}$ for both $\text{Kn} = 0.001$ and $\text{Kn} = 0.05$ obtained by CROW-CFD are shown. In the same picture also the theoretical linear profiles [58] for no-slip flow and for a slip flow at $\text{Kn} = 0.05$ are reported.

From figure 2.7 it is evident that both at $\text{Kn} = 0.001$ (with no-slip boundary conditions) and at $\text{Kn} = 0.05$ (with velocity slip boundary conditions) the CROW-CFD is in very good agreement with the theoretical solutions.

2.2.6.4 Jet expansion in a cylindrical chamber

In this section a comparison between CROW-CFD and the commercially available code FLUENT [29] is presented.

We model an Argon jet expansion in a cylindrical chamber (figure 2.8).

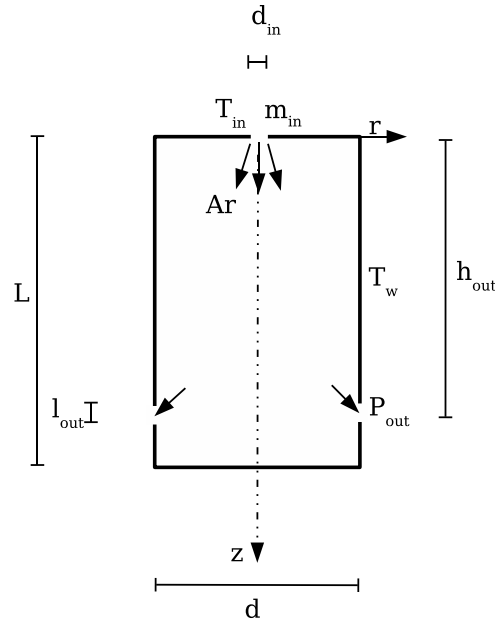


Figure 2.8: Jet expansion geometry and flow conditions.

An Argon jet with mass flow $\dot{m} = 0.065 \text{ kg}/(\text{m}^2\text{s})$ at a temperature of $T_{\text{in}} = 1400 \text{ K}$ is injected from the top in a cylindrical chamber of height $L = 0.8 \text{ m}$ and diameter $d = 0.32 \text{ m}$ through a circular hole of diameter $d_{\text{in}} = 0.032 \text{ m}$. The pumping exit is a circular slit in the chamber sidewall with a $l_{\text{out}} = 0.04 \text{ m}$ width at a distance of $h_{\text{out}} = 0.6 \text{ m}$ from the nozzle where the pressure is kept at a value $P_{\text{out}} = 100 \text{ Pa}$. The walls of the chamber are at a temperature $T_w = 700 \text{ K}$.

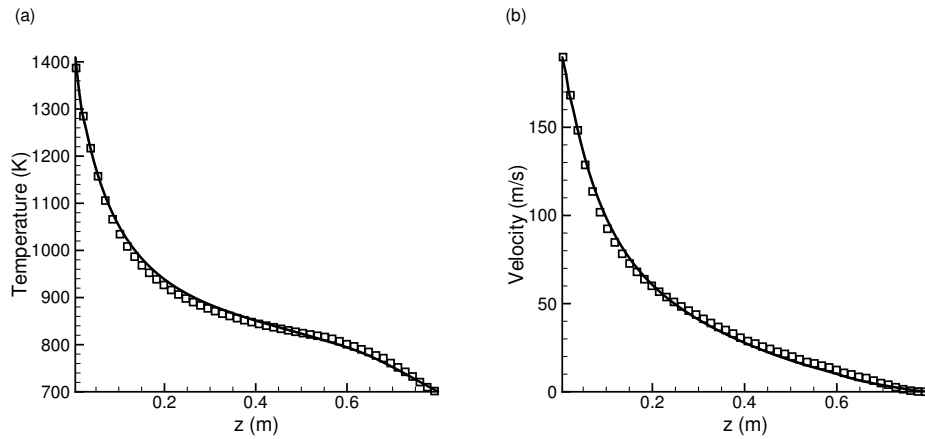


Figure 2.9: Jet expansion: temperature (a) and velocity (b) profiles along the axis. FLUENT(—), CROW-CFD (\square)

Inside the chamber we suppose the flow to be 2-D axisymmetric, and because of that only half of the flow field is simulated. The grid is composed of 100 cells in the axial direction and 50 cells in the radial direction.

The gas pressure is computed from the ideal gas law, whereas its viscosity and thermal conductivity are taken to be temperature dependent in a way as computed from kinetic theory.

A comparison between the results of CROW-CFD and FLUENT can be seen in figures 2.9 and 2.10. In particular, the temperature and velocity axial profiles are shown in figure 2.9, while in figure 2.10 the temperature and velocity radial profile at positions $z = 0.05 \text{ m}$, $z = 0.1 \text{ m}$, $z = 0.2 \text{ m}$ and $z = 0.4 \text{ m}$ are presented.

The figures clearly show that the simulation results of CROW-CFD and FLUENT are in very good agreement.

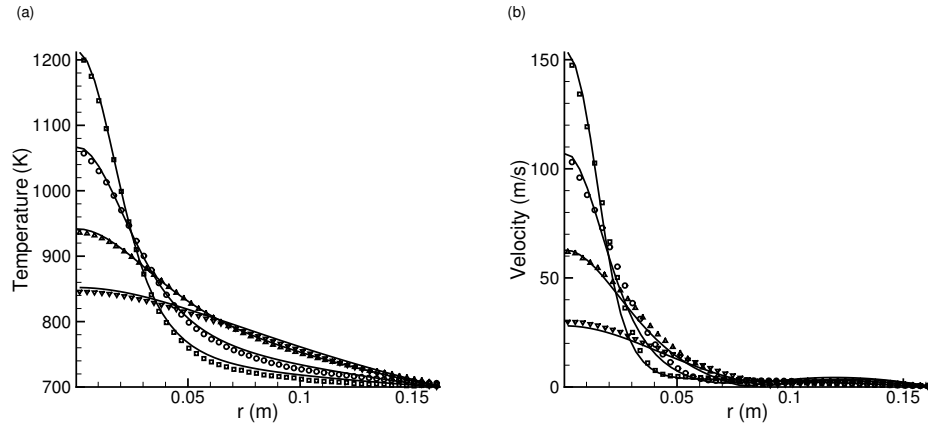


Figure 2.10: Jet expansion: temperature (a) and velocity (b) radial profiles computed by CROW-CFD at $z = 0.05$ m (\square), $z = 0.1$ m (\circ), $z = 0.2$ m (\triangle) and $z = 0.4$ m (∇), compared to results from FLUENT(—).

2.2.6.5 Concluding remarks

At the end of this section, it can be concluded that the CROW-CFD performs well in all validation cases. The results given by the code match with analytical solutions and results given by the commercial code FLUENT in all cases.

2.3 Direct Simulation Monte Carlo scheme for rarefied gas flows

The aim of this section is to describe the basics of the CROW-DSMC (Continuum Rarefied fLOW - DSMC) code for numerical simulations of rarefied gas flows.

The Boltzmann equation can be solved analytically for some simple problems only. Numerically, solutions can be obtained for a somewhat broader range of problems. For engineering problems involving complex geometries, however, it is next to impossible to solve the Boltzmann equation, even numerically. Another disadvantage of the Boltzmann equation is the fact that its definition does not include the possibility for chemical reactions.

The Direct Simulation Monte Carlo (DSMC) method [6], which is closely related to the Boltzmann equation, does not suffer from these shortcomings, and it is therefore the preferred method for simulations of engineering type rarefied gas flows. Rather than solving continuum based partial differential equations like the Navier-Stokes equations, the DSMC method aims at modeling gas flows by calculating the movements and collisions of computational particles which represent molecules in the real flow.

Like the Boltzmann equation [1], the DSMC method assumes a dilute gas and molecular chaos. In a dilute gas, the molecules occupy only a small fraction of the total gas volume. Consequently, the position and velocity distributions of two colliding particles are uncorrelated, which is the definition of molecular chaos. The DSMC method is inherently transient, and steady state solutions are obtained by letting a transient simulation evolve into the long-time, steady state. During the transient calculations, the position, velocity and internal energy of the computational particles are stored and updated each time step. It has been shown [59] that solutions obtained with the DSMC method converge to solutions of the Boltzmann equation in the limit of infinitely small cell size and time step, and infinite number of computational particles. In addition to the two assumptions mentioned above, the DSMC method involves two more main assumptions:

- It is not necessary to calculate the path of every real molecule, but a relatively small statistical sample of N particles suffices. Typically, $N = 10^5 - 10^7$, which may be compared to e.g. 10^{15} molecules in 1 mm^3 of atmospheric air. The ratio F_{num} , which is defined as the ratio between the number of molecules in the real flow and the number N of simulation particles, can be a very large number (e.g. $10^{10} - 10^{20}$). In a simulation with multiple species, each computational particle thus represents F_{num} particles of a certain (single) species in the real flow.
- The translation of the computational particles can be decoupled from their collisions with other computational particles. This implies that each simulation time step can be split into two steps:

- A translation step in which all particles are displaced and interactions with boundaries are computed;
- A collision step in which inter-particle collisions are modelled.

The translation step is purely deterministic, whereas the collision step involves a Monte Carlo type approach, hence the name Direct Simulation Monte Carlo.

A typical DSMC calculation involves:

- Initialization,
- Particle movement,
- Particle collisions,
- Sampling.

They will be discussed in the following sections.

More specifically, the CROW-DSMC code, developed in this work, has the following properties and features:

- 2D plane and axisymmetric,
- Pressure inlet and outlet; diffuse, specular and Cercignani-Lampis-Lord [61; 62; 63] walls and symmetry plane,
- VHS [64] and VSS [65; 66] collision models
- Radial weighting factors

These features are discussed in the present section.

2.3.1 Initialization

At the start of a computation, particles are generated in the flow domain according to the prescribed initial conditions. These include the geometry of the flow domain, the initial temperature T , the initial number density n , and the initial mass-average velocity \vec{V}_{ma} . From the prescribed value of F_{num} and the initial flow density the number of computational particles is calculated. Each of these particles is then assigned a location and a velocity. For the most common case of a uniform initial density, the location of the particles is chosen such that they are evenly distributed in the entire domain. The velocities of individual particles are usually sampled from the Maxwellian distribution f^{Max} (equation 2.28) belonging to the initial temperature. Alternatively, a Chapman-Enskog distribution can be used f^{CE} (equation 2.27).

2.3.2 Particle movement and boundary interaction

In each DSMC time step, the translation of all particles is calculated in a fully deterministic way from the old location \vec{X}_t and velocity \vec{V} of the particle:

$$\vec{X}_{t+\Delta t} = \vec{X}_t + \vec{V}\Delta t \quad (2.80)$$

For one-dimensional flows, only one location variable is required to define the position of a computational particle, and equation 2.80 reduces to a scalar equation. A similar reasoning holds for two-dimensional flows. However, because of the requirements of the inter-particle collision treatment, the particles velocities are in both cases treated in three dimensions. Of these, only the relevant components are used in equation 2.80.

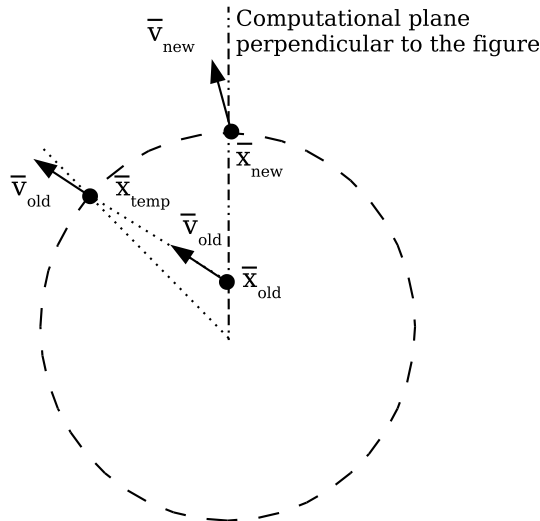


Figure 2.11: Schematic explanation of the displacement of a particle in 2D axisymmetric flows. Shown is a cross section of the flow normal to the flow axis. (based on [34])

As schematically shown in figure 2.11 taken from [34], in the case of two-dimensional axisymmetric flows the movement of a computational particle is first treated completely three-dimensionally in cartesian coordinates, and then the new location is

transferred back to the two-dimensional axisymmetric plane. The location of a computational particle in the computational plane (figure 2.11) is described by only two position variables. According to equation 2.80, during the movement phase a particle will move from a position \vec{x}_{old} to a location \vec{x}_{temp} , thus leaving the computational plane. It is then necessary to transfer the particle back to the computational plane (position \vec{x}_{new}) without changing neither its axial and radial coordinates, nor its axial, radial and circumferential velocity components. Therefore, the Cartesian velocity must be changed from \vec{v}_{old} to \vec{v}_{new} . If, during its displacement, the path of a computational particle intersects with a solid surface, the interaction with this surface is calculated as fully diffuse, fully specular [2] or using the Cercignani-Lampis-Lord [61; 62; 63] model. A symmetry plane is treated identical to a specular surface. In the diffusive model, the particle is reflected with a velocity sampled from the equilibrium velocity distribution f^{Max} (equation 2.28) with the surface temperature, thus it is fully accommodated at the surface temperature. On the contrary, using a specular model, all particle properties remain equal, but the velocity component normal to the wall is reversed. To overcome the limitations of these extreme and unrealistic models, a Cercignani-Lampis-Lord (CLL) model [61; 62; 63] can be used, which is intermediate between the specular and diffusive models, but far more general than a simple combination of them. It allows for the independent specification of the accommodation coefficients for the normal and tangential momentums.

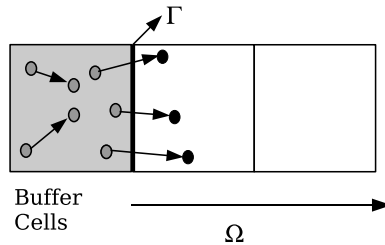


Figure 2.12: Buffer zone approach for inlet (outlet) boundary conditions.

During the movement phase of the calculation, new particles are also entered into the domain through open boundaries. For the implementation of these boundaries, a "buffer zone" or "particle reservoir" approach is used [67]. Some "buffer cells" are considered across the open boundary outside the simulation domain. Every time step, a number of particles, according to the density ρ_{BC} at the boundary, are generated inside these buffer cells with an average temperature T_{BC} and velocity V_{BC} . A Maxwellian (equation 2.28) or Chapman-Enskog (equation 2.27) distribution is used to create these particles. The created particles are then moved for one time step.

Particles that remain in the buffer cells are deleted. The molecules that move into the simulation domain are inserted in the simulation (figure 2.12).

For a pressure inlet, the temperature and pressure, and therefore the density, are fixed while the velocity is unknown. For a pressure outlet, only the pressure is fixed and the temperature and velocity are unknown. For each "buffer cell" the unknown variables are interpolated from the first cell in the flow nearest to the "buffer cell".

2.3.3 Particle collisions

For the purpose of calculating the collisions between computational particles through a Monte Carlo type of approach, the simulation domain is divided into cells with maximum dimensions $\Delta x, \Delta y, \Delta z < \lambda/3$. Here, λ is the particles' mean free path length. Typically, the total number of computational particles is chosen such that the average number of particles in each cell is larger than ~ 30 .

In each time step, the collisions between the N computational particles in a cell can be calculated using the number of pairs N_c and the collision probability P for each pair:

$$N_c = \frac{N(N-1)}{2} \quad (2.81)$$

$$P = F_{\text{num}} \frac{\Delta t \sigma_T c_r}{V} \quad (2.82)$$

The fraction $\frac{\Delta t \sigma_T c_r}{V}$ is the probability that the computational particles will collide in a time step, with σ_T the total collision cross-section of the two particles, c_r their relative speed, Δt the time step and V the cell volume. By multiplying this probability with the ratio F_{num} between the number of real molecules and the number of computational particles, the correct collision frequency for the real gas is obtained. The probability P is evaluated for each pair and a collision is accepted or rejected by comparing P to a random number.

This method of calculating collisions is not very efficient as the value of P is usually very small. DSMC calculations therefore use an adapted method in which the number of pairs is reduced such that the collision probability for a pair can be increased:

$$N_c = \frac{1}{2} N^2 F_{\text{num}} \frac{\Delta t (\sigma_T c_r)_{\text{max}}}{V} \quad (2.83)$$

$$P = \frac{\sigma_T c_r}{(\sigma_T c_r)_{\text{max}}} \quad (2.84)$$

The value of $(\sigma_T c_r)_{\text{max}}$ is estimated at the start of a calculation, and is adjusted if a higher value is found during the calculations. For $F_{\text{num}} N$ large compared to unity, the second method of calculating the collisions (equations 2.83 and 2.84) approaches

the first (equations 2.81 and 2.82) and is therefore physically correct, while computationally much more efficient.

For each of the total number of pairs, a pair of computational particles is selected from the cell at random. The colliding particles do not have to be close in physical space (as long as they are within the same computational cell), nor do their paths need to intersect. As long as the cell dimensions are smaller than $\lambda/3$, this does not have a significant effect on the results. To further decrease the effect of separation, a cell may be divided into sub-cells, and a pair is selected from the same sub-cell if possible.

2.3.3.1 Collision models

In order to determine the collision cross-section σ_T and the post-collision velocities and internal energies of the computational particles, various collision models can be used.

The parameters of the collision model determine, macroscopically, the diffusion coefficient, thermal diffusivity and viscosity of the gas and, microscopically, the collision frequency of particles and the transfer of momentum and energy during a collision. The most used collision models in DSMC are the one-parameter Variable Hard Sphere (VHS) [64] model, and the two-parameters Variable Soft Sphere (VSS) [65; 66] model. Both models calculate a collision cross section σ_T as

$$\sigma_T = \frac{\pi}{4} d^2 \quad (2.85)$$

with d the collision diameter

$$d = d_{\text{ref}} \left[\left(\frac{2k_B T_{\text{ref}}}{m_r c_r^2} \right)^{\omega - \frac{1}{2}} \frac{1}{\Gamma(\frac{5}{2} - \omega)} \right]^{\frac{1}{2}} \quad (2.86)$$

and, k_B the Boltzmann constant, c_r the relative velocity of the two molecules and m_r the reduced mass, defined as

$$m_r = \frac{m_1 \cdot m_2}{m_1 + m_2} \quad (2.87)$$

The parameter d_{ref} is the diameter at a reference temperature T_{ref} , and ω is the viscosity-temperature exponent, viz. $\mu \propto T^\omega$.

The deflection angle χ in a collision is calculated as

$$\cos\left(\frac{\chi}{2}\right) = \left(\frac{b}{d}\right)^{\frac{1}{\alpha}} \quad (2.88)$$

from which

$$\cos(\chi) = 2\left(\frac{b}{d}\right)^{\frac{2}{\alpha}} - 1 \quad (2.89)$$

where b is the miss distance or impact parameter and α is a VSS model parameter ($\alpha = 1$, for the VHS model). Since in DSMC the paths of the computational particles do not cross during a collision, b is unknown. However, since for the selected pair of particles the ratio $(\frac{b}{d})^2$ is uniformly distributed between 0 and 1, the cosine of the deflection angle χ can be calculated as

$$\cos(\chi) = 2\left(\mathbf{R}\right)^{\frac{2}{\alpha}} - 1 \quad (2.90)$$

with \mathbf{R} a random number.

With the VHS model it is possible to accurately reproduce the temperature dependence of the viscosity. The introduction of the parameter α in the VSS model allows for the reproduction of the temperature dependence of (thermal) diffusivities as well.

2.3.4 Sampling

Due to the relatively low number of computational particles (compared to the number of molecules in a physical system), DSMC results suffer from statistical noise. The amount of noise is reduced by sampling the molecular properties during many time steps (for a steady problem) or many ensembles (for an unsteady problem). For steady state flow problems, sampling of the flow properties is performed inside the time step loop and over many time steps once steady state has been reached. Because two consecutive samples are usually highly correlated, sampling is usually done once every ~ 4 time steps. Flow properties are averaged over the same cells as used for the collision routines. Within one cell and at one sampling time, the following particle properties are accumulated:

- number of particles N ,
- the sum of their velocities $\sum \vec{V}_i$,
- the sum of the square of their velocities $\sum (\vec{V} \cdot \vec{V})_i$

All relevant flow data such as the mass-average velocity \vec{V}_{ma} , the temperature T and the density ρ can be calculated from these data.

The density is calculated as:

$$\rho = F_{\text{num}} \frac{Nm}{V} \quad (2.91)$$

The equation for the mass-average velocity is:

$$\vec{V}_{ma} = \frac{\sum \vec{V}_i}{N} \quad (2.92)$$

Finally, the temperature is determined as:

$$T = \frac{m[\sum(\vec{V} \cdot \vec{V})_i - \vec{V}_{ma} \cdot \vec{V}_{ma}]}{3k_B} \quad (2.93)$$

For unsteady flows, sampling during many time steps is not possible. In this case, many ensembles are calculated, and the flow properties are derived by averaging over all ensembles the samples taken at a specific time. This can be time and memory consuming due to the large number of ensembles which are needed and the necessity of storing sample data also as a function of time.

2.3.5 Radial weighting factors

In a simulation of a uniform two-dimensional axisymmetric flow with cells evenly spaced in the radial direction the number of particles is very small in the cell at the axis and very large in the cell furthest from the axis. Thus, in order to have a decent statistical sample of the flow near the axis, we would need to use an unpractically large number of particles at large radial position r . A classical approach to solve this problem is the introduction of radial weighting factors.

When radial weighting factors are in use, each particle represents W real molecules depending on its radial position r , according to

$$W = \frac{r}{r_{\text{ref}}} F_{\text{num}} \quad (2.94)$$

with r_{ref} a reference radius.

Using this approach we impose that a particle far away from the axis is representative of a higher number of real molecules than a particle close to the axis. According to that, a particle moving away from the axis has some probability to be removed from the simulation and similarly a particle moving toward the axis has some probability to be duplicated, depending on its old and new values of W .

The clear advantage of this approach is the even distribution of the particles over the cells in the two-dimensional computational domain.

The use of radial weighting factors formally implies the necessity of changing the collision routine. Due to the finite dimension of a cell in the radial direction even particles within the same cell have different weights. However, it has been shown [6], that the use of equal weighting for all particles within a cell and an unchanged collision routine has a negligible effect on the flow.

2.3.6 Validation

The developed CROW-DSMC code has been validated against both theoretical results and numerical results coming from the DSMC1, DSMC1U and DSMC2 codes by Bird [6], respectively for one-dimensional steady, one-dimensional transient and two-dimensional flow simulations.

The test cases have been chosen in order to validate and show all the potentials of the code for steady and transient, low and high Mach number, one-dimensional and multi-dimensional flows.

2.3.6.1 Fluid between two flat plates at different temperature

As first test to validate our CROW-DSMC code a classical test case for rarefied flow is considered [75; 76; 77; 78; 79; 80; 81].

We simulate Argon between two parallel plates of infinite dimension. The left plate is at temperature $T_{w_1} = 300$ K and the right one is at $T_{w_2} = 400$ K. The gas is macroscopically at rest. The pressure of the fluid is $P = 0.1$ Pa and the mean free path is $\lambda \approx 0.025$ m. In order to vary the Knudsen number ($\text{Kn} = 0.01$, $\text{Kn} = 0.1$ and $\text{Kn} = 1$), we considered three different values for the distance L between the plates, and respectively $L = 2.5$ m, $L = 0.25$ m and $L = 0.025$ m.

The grid is composed by 100 cells in the x direction and 1 in the y direction. The VHS model was used for the collisions and the two plates were modelled as diffusive walls.

We can define the dimensionless temperature as

$$T^* = \frac{T - T_{w_1}}{T_{w_2} - T_{w_1}} \quad (2.95)$$

In the theoretical solution under continuum conditions ($\text{Kn} = 0.01$), T^* increases linearly from zero at the left wall, to unity at the right one. On the contrary, in rarefied conditions we expect on both walls a temperature jump. For $\text{Kn} \leq 0.1$ the temperature jump can be analytically calculated as

$$\Delta T = T - T_w = C_T \frac{dT}{dn} \quad (2.96)$$

with T_w the wall temperature, n the direction normal to the wall and C_T the jump length. Maxwell [2] estimated the jump length to be proportional to the mean free path length λ :

$$C_T = \frac{15\sqrt{\pi}}{16} \lambda \quad (2.97)$$

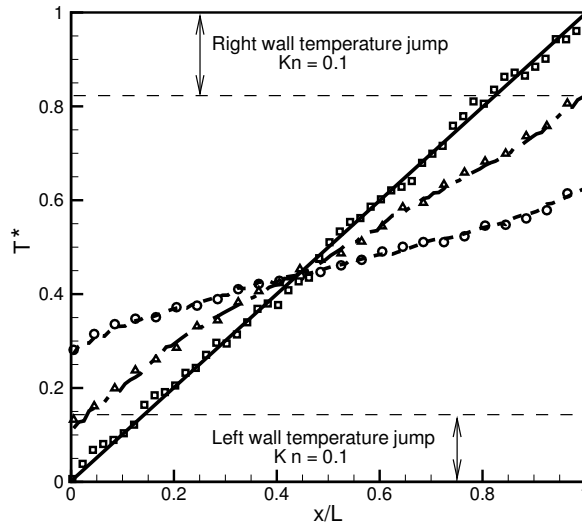


Figure 2.13: Dimensionless temperature of a fluid between flat plates. Theory ($\text{Kn} \leq 0.01$) (—), DSMC1 at $\text{Kn} = 0.1$ (- · -), DSMC1 at $\text{Kn} = 1$ (- -), CROW-DSMC at $\text{Kn} = 0.01$ (□), CROW-DSMC at $\text{Kn} = 0.1$ (Δ), CROW-DSMC at $\text{Kn} = 1$ (○)

In figure 2.13 we compare the dimensionless temperature T^* between the two plates calculated by CROW-DSMC to the theoretical linear trend for $\text{Kn} = 0.01$ and to the results obtained by DSMC1 by Bird [6] for $\text{Kn} = 0.1$ and $\text{Kn} = 1$. In the same picture we also show the theoretically predicted temperature jumps on both walls for $\text{Kn} = 0.1$. Please note that, since λ varies with T and therefore with x , the temperature jump is not the same at both walls.

There is a very good agreement between predictions by the DSMC1 code by Bird and CROW-DSMC for $\text{Kn} = 1$ and $\text{Kn} = 0.1$, and between CROW-DSMC and the theoretical linear trend for $\text{Kn} = 0.01$. For $\text{Kn} = 0.1$, CROW-DSMC predicts the same temperature jump on both walls as equation 2.96. Therefore from figure 2.13 it is clear that CROW-DSMC is performing very well in this test case.

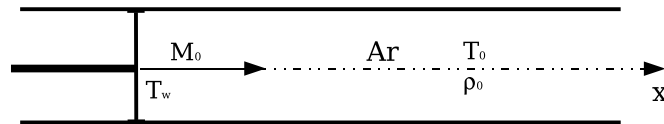
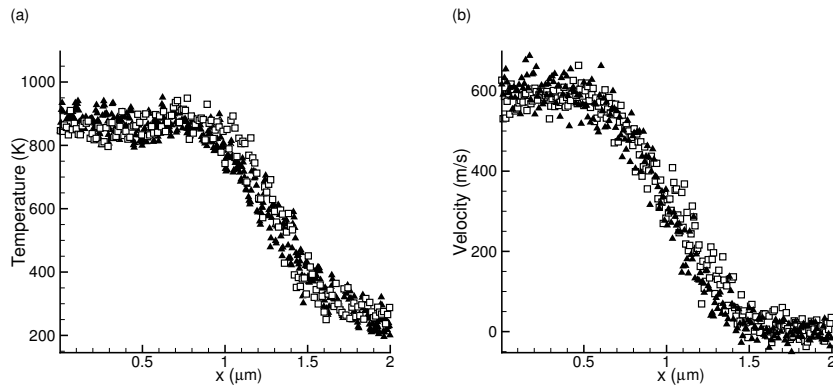


Figure 2.14: Impulsive piston test case.

2.3.6.2 The impulsive piston

In this section we will compare predictions by CROW-DSMC to predictions by Bird's DSMC1U code [6] for the 'impulsive piston' problem (figure 2.14). This is a classical test case for unsteady one-dimensional compressible gas flow simulations in both continuum and rarefied conditions [6; 12; 82; 83; 84].

Figure 2.15: Impulsive piston: temperature (a) and velocity (b) profiles after 1×10^{-9} s. DSMC1U (\square), CROW-DSMC (\blacktriangle).

We simulate a flow of Argon at initial density $\rho_0 = 1.8 \times 10^{-3}$ kg/m³ and temperature $T_0 = 273$ K, moving at Mach $M_0 = 2$ toward a wall held at a fixed temperature of

$T_w = 1000$ K. This is equivalent to an impulsively started piston travelling at Mach M_0 into Argon initially at rest in the reference frame of the piston.

The grid contains 500 cells in the x direction and 1 cell in the y direction. The VHS model was used for the collisions and the diffusive wall model was used for the piston. The number of runs for the ensemble average is 50. Yet there still is quite some statistical scatter in the results.

In figure 2.15 we compare the temperatures and velocities at $t = 1 \times 10^{-9}$ s predicted by CROW-DSMC to those obtained by DSMC1U. Within the bands of statistical scatter, the results of both codes are in very good agreement also in this test case.

2.3.6.3 Rarefied Poiseuille flow

In this section, we use the CROW-DSMC code to simulate a rarefied low Mach number plane Poiseuille flow (figure 2.16). The test case is very similar to the one described in section 2.2.6.2, but we decreased the pressure in order to increase the average Knudsen number to $Kn = 0.15$.

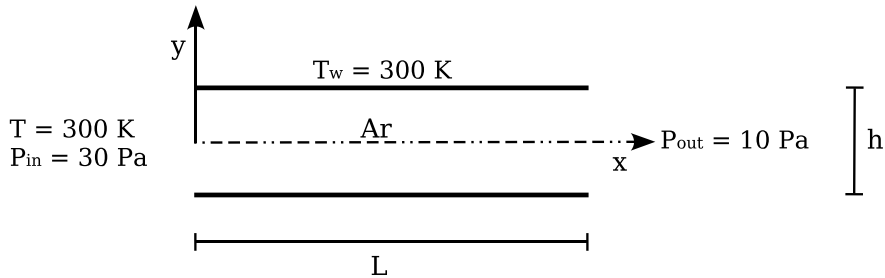


Figure 2.16: Rarefied Poiseuille flow test case.

We consider a flow of Argon at a temperature $T = 300$ K in a channel of height $h = 0.002$ m and length $L = 0.005$ m. The pressure at the inlet is $P_{in} = 30$ Pa and at the outlet $P_{out} = 10$ Pa. The wall temperature is $T_w = 300$ K. At a sufficient distance from the inlet, the flow is a Poiseuille flow: its solution under continuum conditions is known and characterized by a linear pressure decay in the x direction and a parabolic velocity profile in the y direction [56; 57]. Because of symmetry, we limit the simulation domain to the upper half of the channel. The grid is composed by 50 cells in the x direction and 20 cells in the y direction. The VHS model was used for the collisions and the diffusive wall model was used for the walls of the channel. In figure 2.17(a) we compare the pressure drop along the x direction predicted by the CROW-DSMC to results obtained by the DSMC2 code by Bird [6]. In the same

picture also the theoretical linear pressure drop for continuum conditions is shown. From the picture, it is clear that CROW-DSMC and DSMC2 are in good agreement with each other and they both show the non linear pressure drop which is known to prevail for rarefied Poiseuille flow [85; 86].

In figure 2.17(b) we show the fully developed velocity profile at the position $\frac{x}{h} = 2$, normalized the maximum velocity V_0 under continuum conditions

$$V_0 = \frac{\left(\frac{h}{2}\right)^2}{2\mu} \frac{\Delta P}{L} \approx 95 \text{ m/s} \quad (2.98)$$

with μ the viscosity of the fluid and $\Delta P = P_{\text{in}} - P_{\text{out}}$.

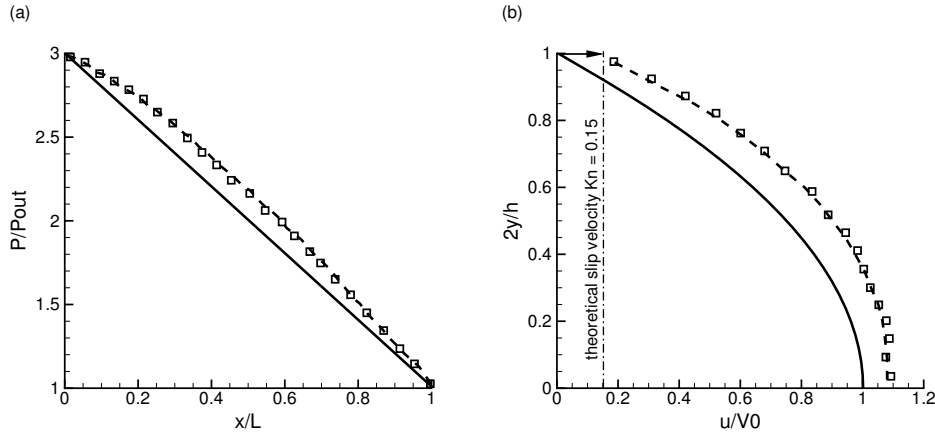


Figure 2.17: Rarefied Poiseuille flow: pressure (a) and velocity profile at $\frac{x}{h} = 2$ (b). Theoretical continuum Poiseuille solution (—), DSMC2 (---), CROW-DSMC (\square)

The velocity profile predicted by the CROW-DSMC code is compared to the solution obtained using DSMC2, to the parabolic analytical solution for continuum Poiseuille flow, and to the theoretical slip flow velocity at the wall for $\text{Kn} = 0.15$ according to equation 2.79. The CROW-DSMC and the DSMC2 give very similar results for the velocity profile, and the computed slip velocity agrees very well with the theoretically predicted value [85]. The slip effect increases the average velocity in the channel at given total pressure drop and reduces the curvature of the velocity profile with respect to the continuum solution [85]. It can be concluded that CROW-DSMC code was performing very well also in this test case.

2.3.6.4 Rarefied Couette flow

We apply the CROW-DSMC code to simulate the rarefied low Mach number plane Couette flow (figure 2.6) in the test case already described in section 2.2.6.3, with a value of the Knudsen number $Kn = 0.05$.

We consider a flow of Argon between two infinite parallel flat plates at a distance $h = 0.005$ m. The bottom plate is at rest, while the upper one moves from left to the right with velocity $V_0 = 100$ m/s. The plates are at the same temperature of the gas $T_w = T_0 = 300$ K. The gas between the plates is at a pressure $P_0 = 10$ Pa and the mean free path is $\lambda \approx 2.5 \cdot 10^{-4}$ m.

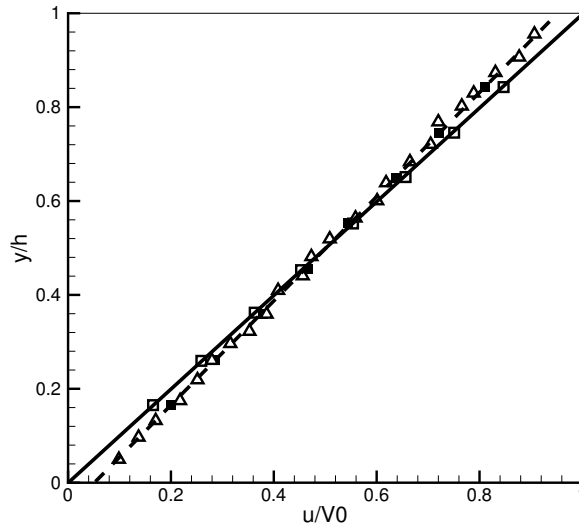


Figure 2.18: Couette flow: velocity profile at $x = 5h$. Theory with no-slip BC (—), theory with slip velocity BC at $Kn = 0.05$ (---), CROW-CFD with no-slip BC (\square), CROW-CFD with slip BC at $Kn = 0.05$ (\blacksquare), CROW-DSMC (\triangle)

The computational domain is extended for a length $L = 10h$ in the x direction to avoid the influence of the boundaries. The grid is composed by 200 cells in the x direction and 50 cells in the y direction.

In figure 2.18 the velocity profiles at $x = 5h$ obtained by CROW-DSMC is compared with the theoretical slip flow solution and the results of CROW-CFD with slip flow boundary conditions. In the same picture also the theoretical linear profiles for no-slip

flow and the results of CROW-CFD with no-slip boundary conditions are reported. From figure 2.18 it is evident that the CROW-DSMC is in very good agreement with the theoretical slip flow solution and the solution of CROW-CFD in the same conditions and with slip boundary conditions.

2.3.6.5 Concluding remarks

At the end of this section, it can be concluded that the CROW-DSMC performs well in all validation cases. The results given by the code match with analytical equations and results given by the DSMC1, DSMC1U and DSMC2 codes by Bird [6] in all cases.

3. Development of a hybrid N-S/DSMC solver

In this chapter the hybrid CFD/DSMC approach is presented. We describe how the models of the previous sections 2.2 and 2.3 are coupled through a Schwarz method [10; 14]. The strategy implemented for coupling the Navier-Stokes based CFD code and the DSMC code for steady flow simulations is presented in section 3.3, whereas the approach for unsteady flow simulations is presented in section 3.4. In section 3.5 we present a validation and a sensitivity analysis of the method to various parameters. Most of this chapter has been published in *Advanced Computational Method in Science and Engineering* [38], Hybrid Navier-Stokes/DSMC simulations of gas flows with rarefied-continuum transitions by G. Abbate, B.J. Thijsse and C.R. Kleijn, and as 'Validation of a Hybrid Navier-Stokes/DSMC Method for Multiscale Transient and Steady-State Gas Flows' by G. Abbate, B.J. Thijsse and C.R. Kleijn in the SMMS 2007 special issue of *Int. J. Multiscale Comput. Eng.* [101].

3.1 Introduction

As already highlighted in chapter 1, numerical simulations are an increasingly important tool for the design, improvement and optimization of gas flow equipment. Although in many interesting applications gas flows can be simulated solving the Navier-Stokes equations, there is a wide set of cases where these equations are not applicable.

From chapter 2 it is clear that the Navier-Stokes (N-S) equations give an accurate description of the gas behavior as long as the Chapman-Enskog velocity distribution f^{CE} is a good approximation of the exact velocity distribution f for the particles of the gas. Defining the Knudsen number (Kn) as the ratio between the mean free path and a relevant macroscopic length scale, since f^{CE} is an $O(\text{Kn})$ expansion of the exact solution f , the N-S equations are an accurate model of the flow for $\text{Kn} \ll 1$ only.

Summarizing what has been already discussed in the previous chapters, a gas flow with $\text{Kn} < 0.01$ (or, with modifications of boundary conditions < 0.1) can be simulated using Navier-Stokes based Computational Fluid Dynamics (CFD) models, whereas

gas flows with $\text{Kn} > 0.05$ can be simulated using particle based Direct Simulation Monte Carlo (DSMC) methods. Since DSMC computational costs scale with Kn^{-4} , they become prohibitively large when Kn becomes lower than ≈ 0.05 .

However, in many practical applications, gas flows undergo spatial and/or temporal transitions from low (< 0.01) to high (> 0.05) Kn numbers, e.g. due to varying pressure or dimensions. Examples include: flow around vehicles at high altitudes, particularly re-entry of vehicles in a planetary atmosphere [96], flow through microfluidic gas devices [9], small cold gas thruster nozzle and plume flows [97], and low pressure thin film deposition processes from expanding plasma or gas jets [17].

To accurately and efficiently simulate such gas flows, it is necessary to construct a model that on the one hand accounts for the molecular nature of the gas flow where needed, and on the other hand uses a continuum model where allowed. Such a hybrid model will provide sufficient accuracy at the molecular level, while being sufficiently efficient to model large scale devices.

To compute these kind of flows, different hybrid models have been proposed to couple different kind of continuum and atomistic approaches, for instance: Molecular Dynamics (MD) and Navier-Stokes (N-S) equations [7], Boltzmann and Euler equations [87], Boltzmann and N-S equations [8; 88], Direct Simulation Monte Carlo (DSMC) and Stokes equations [9], DSMC and incompressible N-S equations [10], DSMC and Euler equations [10; 11; 89] and DSMC and N-S equations [12; 13; 14; 15; 16; 90; 91; 92; 93; 94].

In the current work we have decided to couple a compressible Navier-Stokes CFD solver in the continuum region, because of its very wide range of applicability compared to e.g. Euler and incompressible N-S equations, to a DSMC algorithm in the rarefied region, because it is the only practical engineering method that can be used in the rarefied regime.

It is interesting to note that the vast majority of the cited hybrid models can be applied only to steady-state gas flows [7; 8; 9; 13; 14; 15; 16; 87; 88; 90; 91; 92; 93; 94]. The most common coupling technique for unsteady gas flows [10; 11; 12; 89] is a flux-based coupling method with no overlapping between the continuum and the DSMC regions. This approach suffers from three main disadvantages which reduce its efficiency.

The first disadvantage is that using a flux-based coupling approach, it is not possible to decouple the global (CFD) and molecular (DSMC) time scales [10]. Because the fluxes at the interface between the two approaches must be exchanged every time step, both CFD and DSMC must be run using the same time step, the size of which is to be chosen as the smallest of the two allowed by the CFD solver and the DSMC solver, Δt_{CFD} and Δt_{DSMC} respectively. Since in general $\Delta t_{\text{DSMC}} \ll \Delta t_{\text{CFD}}$, this implies the necessity to run also the CFD solver with the same molecular time step, thus reducing the efficiency of the method [10].

The absence of an overlapping region is a second disadvantage of the flux-based

method. Since the exchange of information between the continuum and molecular approaches takes place at the position of their interface, its exact location is important [10; 15; 16]. Thus, in a flux-based coupling method, simulation results strongly depend on the interface location.

The third disadvantage is connected with the DSMC statistical scatter involved in determining fluxes, which is much higher than that associated with the macroscopic state variables. As a result, it has been demonstrated that flux-based coupling methods require a high number of samples to reduce the DSMC statistical noise [10; 16]. In this chapter we propose a strategy to efficiently and accurately couple a compressible N-S solver to a DSMC solver for steady and unsteady flows, using Dirichlet-Dirichlet boundary conditions coupling with an overlapped Schwarz method [10; 14]. In section 3.5.1.1 we will show that this method overcomes most of the problems described above. Thus, given the disadvantages of flux-based coupling methods without overlap, our work is a clear step forward in the evolution of hybrid continuum-molecular approaches.

3.2 Breakdown parameter

The first issue in developing a coupled N-S/DSMC method is how to determine the appropriate computational domains for the DSMC and N-S solvers, and the proper interface boundary between these two domains. As a criterion for discriminating the continuum from the rarefied regime and for consequently selecting the proper solver, the continuum breakdown parameter Kn_{\max} [98] is employed

$$\text{Kn}_{\max} = \max[\text{Kn}_{\rho}, \text{Kn}_V, \text{Kn}_T] \quad (3.1)$$

where Kn_{ρ} , Kn_V and Kn_T are the local Knudsen numbers based on density, velocity and temperature length scales, according to

$$\text{Kn}_Q = \frac{\lambda}{Q_{\text{ref}}} |\nabla Q| \quad (3.2)$$

Here, Q is a flow property (density, velocity or temperature) and λ is the local mean free path length. Q_{ref} is a reference value for Q , which can either be its local value (for temperature or pressure), or a typical value (for the velocity). In the region where the continuum breakdown parameter Kn_{\max} exceeds a limiting value Kn_{split} , the N-S equations cannot be applied to accurately model the flow, and DSMC has to be used. In the following sections the two different strategies implemented for coupling the Navier-Stokes based CFD code and the DSMC code will be described: The first can be applied for steady state flow simulations, the second for unsteady flow simulations.

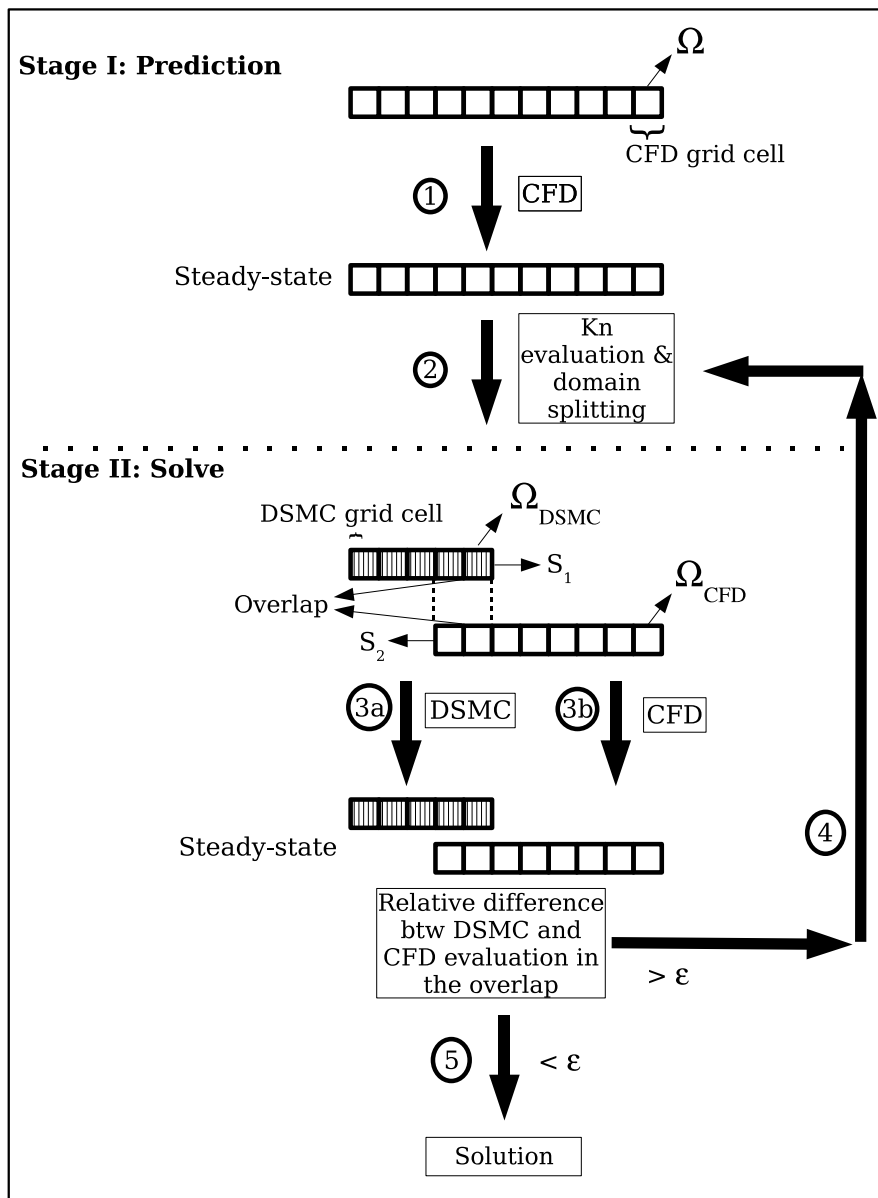


Figure 3.1: Scheme of the coupling method for steady-state flows.

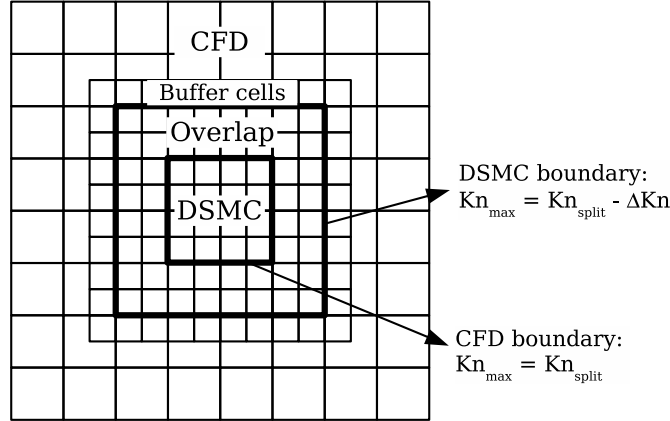


Figure 3.2: Illustration of the Schwarz coupling method in a 2-D geometry.

3.3 Steady-state formulation

The proposed coupling method for steady flows is based on the Schwarz method [10; 14] and it consists of two stages, as illustrated in figure 3.1.

The first stage is a prediction stage, where (1) the unsteady N-S equations are integrated in time on the entire domain Ω until a steady state is reached. From this steady state solution, (2) the continuum breakdown parameter Kn_{\max} is computed and its values are used to split Ω in the subdomains Ω_{DSMC} ($\text{Kn}_{\max} > \text{Kn}_{\text{split}} - \Delta\text{Kn}$), where the flow field will be evaluated using DSMC, and Ω_{CFD} ($\text{Kn}_{\max} < \text{Kn}_{\text{split}}$), where N-S equation will be solved. For Kn_{split} a value of 0.05 was used. Between the DSMC and CFD regions an overlap region ($\text{Kn}_{\text{split}} - \Delta\text{Kn} < \text{Kn}_{\max} < \text{Kn}_{\text{split}}$) is considered, where the flow is computed with both the DSMC and the CFD solver (figure 3.2). ΔKn is a value that was varied in order to vary the overlapping region size (section 3.5.1.1).

In the second stage, DSMC and CFD are run in their respective subdomains with their own time steps (Δt_{DSMC} and Δt_{CFD} , respectively), until a steady state is reached. First DSMC is applied (3a); molecules are allocated to the DSMC subdomain, created from a Chapman-Enskog velocity distribution, according to the density, velocity and temperature obtained from the initial CFD prediction. The grid is automatically refined in the DSMC region in order to respect the DSMC requirements ($\Delta x, \Delta y, \Delta z < \frac{\lambda}{3}$). At the CFD/DSMC interface S_1 the boundary conditions to the DSMC region come from the solution in the CFD region. As described in section 2.3.2 "particle reservoir cells" are considered outside the overlap region. In these cells

molecules are created according to the density, velocity, temperature and their gradients in the CFD solution with a Chapman-Enskog velocity distribution.

After running the DSMC, (3b) the N-S equations are solved in the CFD region. The boundary conditions to the CFD region at the CFD/DSMC interface S_2 come from the solution in the DSMC region, averaged over the initial CFD grid cells.

Once a steady state solution has been obtained in both the DSMC and N-S regions, the continuum breakdown parameter Kn_{\max} is re-evaluated and a new boundary between the two regions is computed. This second stage (4) is iterated until in the overlap region the relative difference between the DSMC and CFD solutions

$$\max_{\text{overlap}} \left| \frac{\Delta Q}{Q_{\text{DSMC}}} \right| = \max_{\text{overlap}} \left| \frac{Q_{\text{CFD}} - Q_{\text{DSMC}}}{Q_{\text{DSMC}}} \right| \quad (3.3)$$

with Q a flow property (e.g. pressure or temperature), (5) is less than a prescribed value ε (typically, $\varepsilon \approx 0.001$ [9]).

3.4 Unsteady formulation

In the unsteady formulation, the coupling method described above is iterated every coupling time step $\Delta t_{\text{coupling}} > \Delta t_{\text{CFD}} \gg \Delta t_{\text{DSMC}}$, starting from the solution at the previous time step.

At the beginning of a coupling time step, the predicted DSMC region is compared to the one of the previous coupling time step. In the cells that belong to both the previous and the predicted DSMC regions, we consider the same molecules of the previous coupling time step, whose properties were recorded. In these cells, it is important to consider the same molecules of the previous time step rather than sampling them from continuum variables (temperature, density and velocity) with a Maxwellian or a Chapman-Enskog velocity distribution. This is a clear difference with the procedure in [12], where every time step the molecules in the DSMC cells are sampled from continuum variables with a Chapman-Enskog velocity distribution. The use of a Maxwellian or a Chapman-Enskog velocity distribution presumes either equilibrium or near-equilibrium conditions, which is not necessarily true in these cells. Molecules that are in the cells that no longer belong to the DSMC region are deleted. In cells that have changed from being a CFD cell into a DSMC cell, new molecules are created with a Chapman-Enskog velocity distribution, according to the density, velocity and temperature of the CFD solution at the previous time step.

At the end of every coupling step, molecule properties are recorded to set the initial conditions in the DSMC region for the next coupling step.

The first clear advantage of using a Schwarz method with Dirichlet-Dirichlet boundary conditions, instead of the more common flux-based boundary conditions coupling technique [10; 11; 12; 89], is the possibility to decouple the global (CFD) and molecular (DSMC) time scales [10]. Since it is possible to couple the continuum and molecular

approaches every coupling time step $\Delta t_{\text{coupling}} > \Delta t_{\text{CFD}} \gg \Delta t_{\text{DSMC}}$, in fact, CFD and DSMC can both be run in their respective subdomains with their own time steps (Δt_{DSMC} and Δt_{CFD} , respectively), thus improving the efficiency of the method.

On the contrary, as already highlighted in section 3.1, in the flux-based methods [10; 11; 12; 89], the continuum and molecular approaches must be coupled every single time step, the size of which is to be chosen as the smallest one allowed by both the CFD and the DSMC solver. Since the molecular time step is generally much smaller than the continuum one, then $\Delta t_{\text{coupling}} = \Delta t_{\text{CFD}} = \Delta t_{\text{DSMC}}$.

The second advantage of the Schwarz coupling approach is the use of an overlap region to couple the CFD method to DSMC. Thus, the information exchange between the two methods does not take place at the exact interface position between them, as for the most common flux-based coupling approach [10; 11; 12; 89], but through the entire overlap region. For this reason the simulation results are not strongly influenced by the exact interface location.

The third advantage of using a Schwarz method with Dirichlet-Dirichlet boundary conditions, instead of the more common flux-based boundary conditions coupling technique [10; 11; 12; 89], is that the latter requires a much higher number of samples in the DSMC region than the Schwarz method [10; 15; 16]. It has been shown [16] that in a DSMC simulation the relation between the relative noise on fluxes E_f and that on the state variables E_{sv} is

$$E_f \sim \frac{E_{sv}}{\text{Kn}} \quad (3.4)$$

Since at the continuum-molecular interface $\text{Kn} \approx 0.01 - 0.05$, then $E_f \approx 10 - 20 E_{sv}$ and a 10 – 20 times higher number of samples are necessary to reduce the DSMC statistical scatter in a flux-based coupling approach than in a Schwarz coupling method with Dirichlet-Dirichlet boundary conditions.

3.5 Results and discussion

In this section we will apply our hybrid, dynamically coupled, CFD/DSMC solver to one-dimensional and multi-dimensional, transient and steady-state flows, and we will present a sensitivity analysis of the method to various parameters.

3.5.1 Unsteady shock-tube problem

The unsteady coupling method was applied to an unsteady shock tube test case (figure 3.3).

We have simulated the flow field inside a 0.5 m long tube, connecting two infinitely large tanks filled with Argon at different thermodynamic conditions. A membrane at

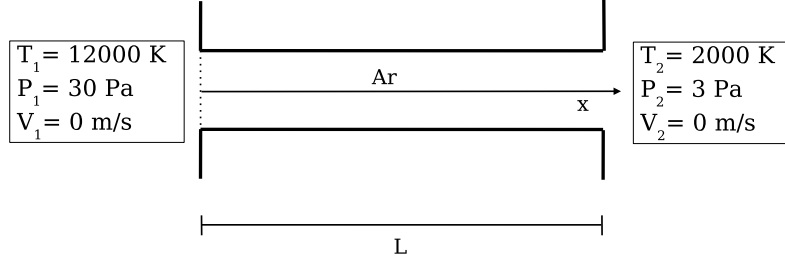


Figure 3.3: Shock tube test case. The dashed line on the left indicates the membrane which is broken at the instant $t = 0$.

the interface between the first tank and the tube divides the two regions where the fluid is in different conditions. In the left tank it is at a pressure $P_1 = 30$ Pa and at a temperature $T_1 = 12000$ K. In the right tank and in the tube it is at a pressure $P_2 = 3$ Pa and at a temperature $T_2 = 2000$ K. These conditions imply that the mean free path (which approximately scales with $T^{1.3}/P$) is everywhere $\lambda \approx 0.01$ m.

At the instant $t = 0$ the membrane breaks and the fluid can flow from one region to the other. Two different waves will start travelling in the tube from the left to the right with two different velocities: a shock wave and a contact discontinuity. The shock wave produces a rapid increase of the temperature and pressure of the gas passing through it, while through the contact discontinuity, the flow undergoes only a temperature, and not a pressure, variation [48; 54; 55].

The thermodynamic conditions inside the infinitely large tanks remain constant. For this reason the two tanks can be modeled with an inlet and an outlet boundary condition.

Inside the tube, we suppose that the flow is one-dimensional. Upstream (left) from the shock, the gas has a high temperature and relatively high pressure, and gradient length scales are small. Downstream (right) from the shock, both temperature and pressure are much lower, and gradient length scales are large. As a result, the continuum breakdown parameter Kn_{\max} (using local values of Q_{ref}) is high upstream from the shock, and low downstream of it. In the hybrid CFD/DSMC approach, DSMC is therefore applied upstream, and CFD is applied downstream. For Kn_{split} a value of 0.05 was used. Rather than setting a value for ΔKn , as discussed in section 3.3, the size of the overlap region was set to 2λ . The initial grid is composed of 100 cells in the x direction and 1 cell in the y direction, while the code automatically refines the mesh in the DSMC region to fulfill its requirements.

The coupling time step was chosen as $\Delta t_{\text{coupling}} = 4.0 \times 10^{-6}$ s and ensemble averages of the DSMC solution were made on 30 repeated runs. It is important to note that, thanks to the time decoupling possibility of the Schwarz method, the CFD and

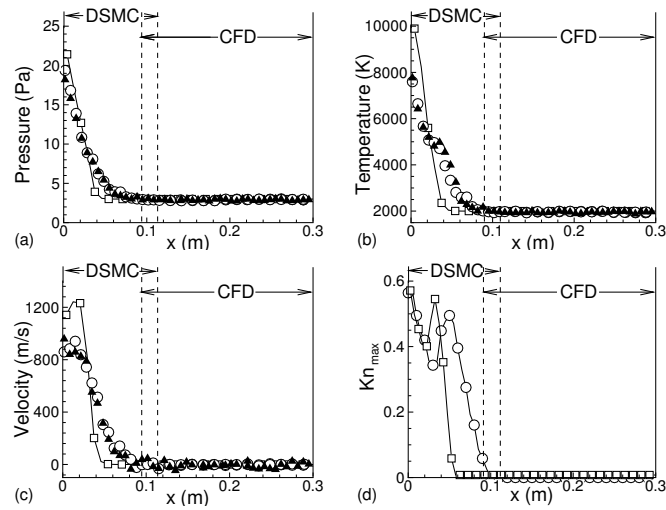


Figure 3.4: Pressure (a), temperature (b), velocity (c) and continuum breakdown parameter Kn_{max} (d) in the tube after 1.5×10^{-5} s. CFD (\square), DSMC (\blacktriangle), Hybrid (\circ).

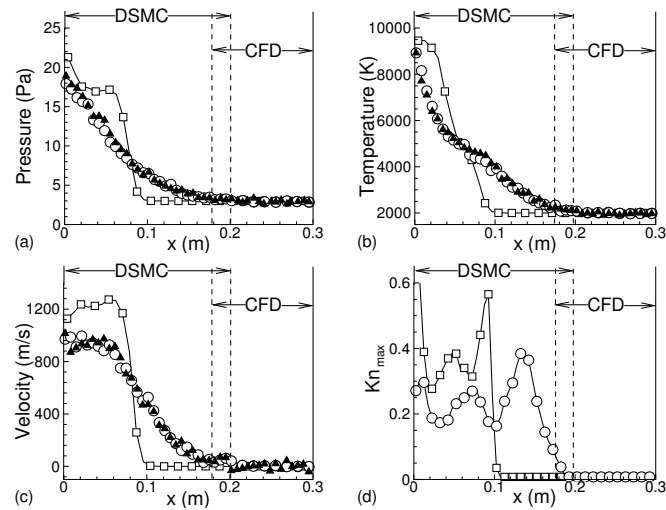


Figure 3.5: Pressure (a), temperature (b), velocity (c) and continuum breakdown parameter Kn_{max} (d) in the tube after 3.0×10^{-5} s. CFD (\square), DSMC (\blacktriangle), Hybrid (\circ).

DSMC approaches were run with $\Delta t_{\text{CFD}} \approx 2.0 \times 10^{-6}$ s and $\Delta t_{\text{DSMC}} \approx 4.0 \times 10^{-7}$ s respectively. When time step decoupling would not have been possible, we should also have run the CFD solver, and have coupled it to the DSMC solver, with a time step of $O(10^{-7})$ s.

In figures 3.4 and 3.5 the pressure (a), temperature (b), and velocity (c) inside the tube after 1.5×10^{-5} s and 3.0×10^{-5} s, evaluated with the coupled CFD/DSMC method, are compared to the results of a full DSMC simulation. The latter was feasible because of the 1-D nature of the problem. Results obtained with a full CFD simulation are shown as well. The full DSMC solution is considered to be the most accurate of the three. In figures 3.4(d) and 3.5(d) the continuum breakdown parameter, computed using the coupled method, is compared to that same parameter computed with the full CFD simulation.

From the results shown in figures 3.4 and 3.5, it is clear that the full CFD approach fails due to the high values of the local Knudsen number caused by the presence of the shock. It predicts a shock thickness of ≈ 2 cm, which is approximately two times the local mean free path ($\lambda \approx 1$ cm) and therefore unrealistic since even in continuum conditions the shock thickness is one order of magnitude greater than the mean free path [99]. In the full DSMC approach, therefore, the shock is smeared over almost 10 cm. The results obtained with the hybrid approach are virtually identical to those obtained with the full DSMC solver, but were obtained in less than one fifth of the CPU time.

Comparing figures 3.4 and 3.5 it is also possible to see how the DSMC and CFD regions adapt in time to the flow field evolution.

3.5.1.1 Sensitivity to numerical parameters

In this section, the sensitivity of the coupled approach to various numerical parameters is addressed for the 1-D shock-tube problem described in section 3.5.1. In particular, the influence of the size of the overlap region, the DSMC noise, and the Courant number, based on the time interval at which DSMC and CFD are coupled, are analyzed.

Overlap region: The sensitivity of our method to the size and position of the overlap region is investigated.

Both DSMC and N-S equations are solved in the overlap region (figure 3.2). The dependence of the results on the size of the overlap region is investigated by considering various overlap sizes: $\lambda/3$, 2λ , 6λ , 12λ , where λ is the mean free path length. In section 3.5.1 an overlap size of 2λ was used.

Figure 3.6 shows the evolution in time of respectively the shock velocity (a) and the shock thickness (b), evaluated using the different overlap sizes. From this picture it is clear that the overlap size does not strongly influence the results of

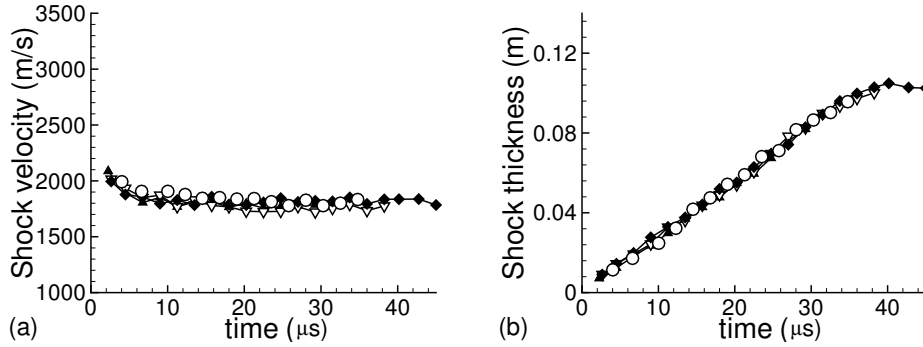


Figure 3.6: Computed shock velocity (a) and shock thickness (b) as a function of time, for different sizes of the overlap region. $\lambda/3$ (\blacktriangle), 2λ (∇), 6λ (\blacklozenge), 12λ (\circ).

the simulation.

During this analysis, for all the considered sizes of the overlap region, two cases were tested: in the first, since the overlap was centered around the position where $\text{Kn} = 0.05$, it could extend also into the $\text{Kn} > 0.05$ region, whereas in the second the overlap was positioned such that it extended entirely in the $\text{Kn} \leq 0.05$ region. It was noted that in the first case, if the overlap region is large, it is important to use an asymmetric overlap that is bounded on one side by the location where $\text{Kn} = 0.1$. Otherwise, if the overlap region would extend into regions where $\text{Kn} > 0.1$, the program would solve the N-S equations in a region where the continuum hypotheses are no longer valid. As a result, instability problems appear (figure 3.7). The appearance of strong fluctuations due to instability produces two effects: the establishment of incorrect boundary conditions to both the CFD and DSMC solvers, and an increase of the local gradients. The increase of the local gradients and the resulting reduction of the gradient length scales implies an incorrect determination of the CFD/DSMC interface. As a consequence, the CFD/DSMC interface rapidly moves into the low Kn number region and together with the wrong boundary conditions produces the rapid propagation of the instability.

This section demonstrates an important advantage of the Schwarz coupling with Dirichlet-Dirichlet boundary conditions. Because of the presence of an overlap region, the information exchange between CFD and DSMC does not take place just at one precise location, as in the flux-based coupling approaches [10; 11; 12; 89]. For this reason as long as we ensure that we run the CFD within its region of applicability ($\text{Kn} \lesssim 0.1$), the exact position and size of the

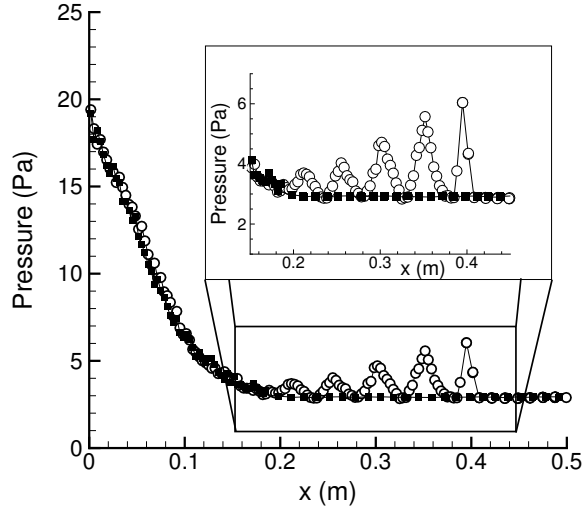


Figure 3.7: Instability problems for an overlap region extending in the $\text{Kn} > 0.1$ region. Overlap entirely in the $\text{Kn} < 0.1$ region (■), overlap partially in the $\text{Kn} > 0.1$ region (○).

overlap region is not crucial.

Number of repeated runs for the ensemble average: To analyze the effect of the noise in the DSMC solution on the coupling method we considered different number of repeated runs for the ensemble average: 5, 30 and 50 runs.

From a comparison (not shown) of the evolution of the shock velocity and thickness, similar to the one in figure 3.6, it became clear that also the number of repeated runs over which we average does not strongly influence the results of the method.

The limited sensitivity of our method to the noise demonstrates a clear advantage of our Dirichlet-Dirichlet coupling method as compared to flux-based coupling schemes [10; 11; 12; 89], which show a strong sensitivity to noise.

Courant number based on the coupling time step: In this section we study the effect of varying the coupling Courant number defined as:

$$C = C_r \frac{\Delta t_{\text{coupling}}}{\Delta x_{\text{CFD}}} \quad (3.5)$$

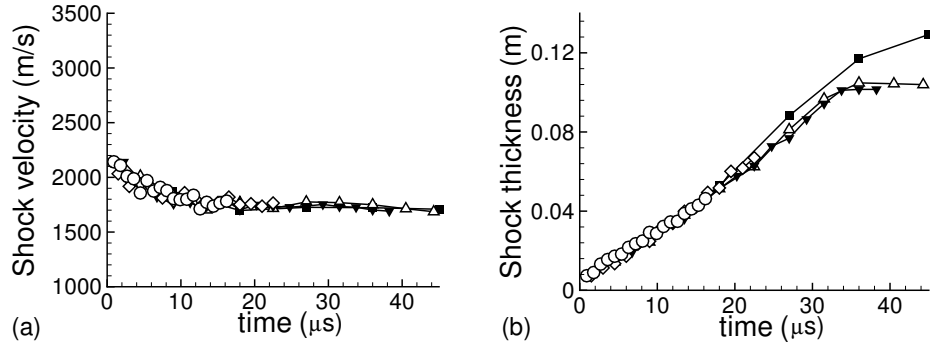


Figure 3.8: Computed shock velocity (a) and shock thickness (b) for different coupling Courant numbers. $C = 1.46$ (■), $C = 0.73$ (△), $C = 0.36$ (▼), $C = 0.24$ (◇), $C = 0.15$ (○).

where Δx_{CFD} is the size of CFD cells and C_r the most probable molecular velocity.

In figure 3.8 we present the evolution in time of both the shock velocity (a) and its thickness (b) for different coupling Courant numbers: 0.15, 0.24, 0.36, 0.73 and 1.46. In order to vary the Courant number, with $C_r = 912$ m/s, we fixed $\Delta x_{\text{CFD}} = 0.005$ m and we considered different values of the coupling time step between 8.0×10^{-7} s and 8.0×10^{-6} s. In terms of multiples of the mean collision time, which is approximately $\Delta t_c \approx 6.0 \times 10^{-6}$ s, this corresponds respectively to $0.13\Delta t_c - 1.3\Delta t_c$. Only in the case where the Courant number $C = 1.46 > 1$, the solution is found to deviate from the other solutions. In this case in fact the shock thickness is higher than for the other cases and the error is due to the appearance of instability effects (figure 3.9).

In order to be sure about the Courant number effect, we also varied the Courant number by varying Δx_{CFD} at fixed $\Delta t_{\text{coupling}}$ and fixed C_r , and by varying C_r (through the temperature) at fixed Δx_{CFD} and $\Delta t_{\text{coupling}}$.

In all cases, instabilities were found to arise when $C > 1$, as expected. It is therefore necessary to keep the Courant number smaller than 1.

This section demonstrates a further advantage of our overlapped Dirichlet-Dirichlet coupling method as compared to flux-based coupling schemes [10; 11; 12; 89]. In the flux-based coupling techniques the impossibility of decoupling the continuum and molecular time scales imposes the necessity to run both the CFD and the DSMC with the molecular time step Δt_{DSMC} , which should be less than $0.1\Delta t_c$ and to couple them with that same time step. The Schwarz coupling, on the other hand, allows us to run the CFD and DSMC with their

own time steps, and to couple them every coupling time step $\Delta t_{\text{coupling}}$ as long as we respect the condition $C < 1$. In the present example this led to $\Delta t_{\text{coupling}}$ up to $0.7\Delta t_c$, a gain of a factor ≈ 7 compared to $\Delta t_{\text{DSMC}} = 0.1\Delta t_c$.

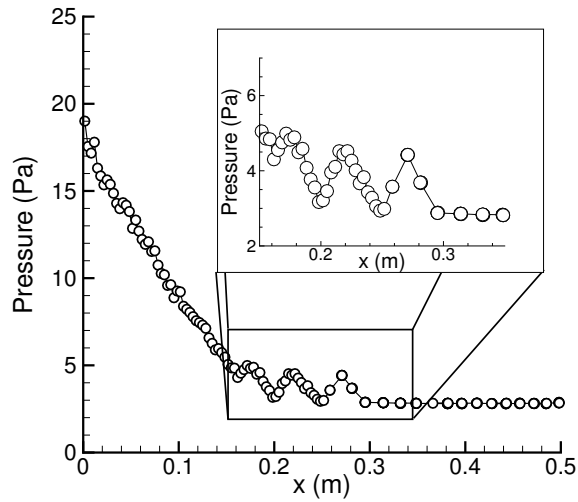


Figure 3.9: Instability problems for Courant number $C = 1.46$.

3.5.2 Unsteady pressure-driven slit flow

To test our unsteady hybrid method in a multidimensional problem, it was applied to an unsteady pressure-driven slit flow test case (figure 3.10). The present test case is very similar to the test case used by Roveda et al. to present their flux-based without overlap hybrid Euler/DSMC method in [102].

We consider a jet of Argon as it evolves following its initial burst from a slit of height $h = 0.05$ m in a wall at temperature $T_w = 500$ K. Before breaking, a membrane closes the slit dividing two regions where the fluid is in different conditions. In the left tank it is at a pressure $P_1 = 16$ Pa and a temperature $T_1 = 500$ K, and the mean free path length is $\lambda_1 \approx 3.0 \cdot 10^{-4}$ m. In the environment (right) it is at a pressure $P_2 = 1.6$ Pa and a temperature $T_2 = 500$ K, and the mean free path is $\lambda_2 \approx 0.003$ m.

At the instant $t = 0$ the membrane breaks, the gas can flow from left to right and a complex jet structure begins to develop. It is important to note that for the chosen

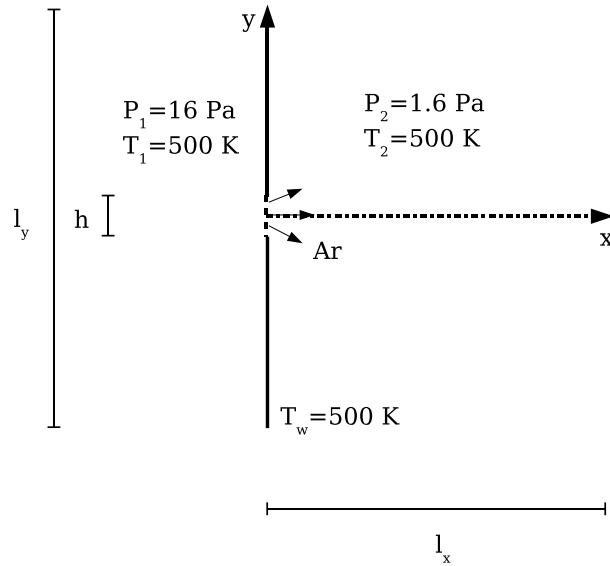


Figure 3.10: Pressure-driven slit flow. The dashed line on the left indicates the membrane which is broken at the instant $t = 0$.

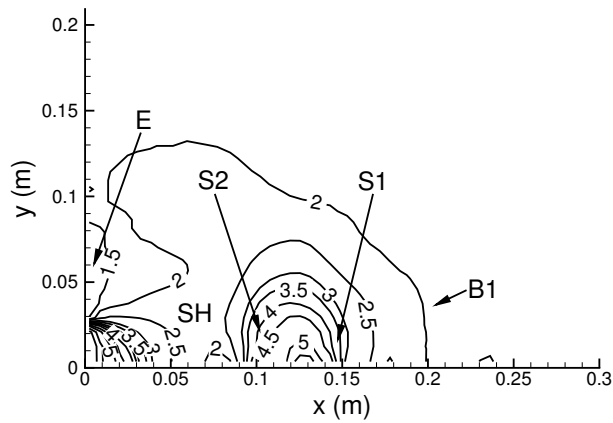


Figure 3.11: Density field (10^{-5} kg/m^3) in the jet after $5.25 \times 10^{-4} \text{ s}$ computed by a full DSMC simulation and illustrating the jet structure: Initial weak shock wave (B1), jet front (S1), normal shock (S2), shear layer (SH) and expansion region (E).

pressure ratio $P_{1-2} = P_1/P_2 = 10$, a supersonic jet develops downstream the slit [102].

Figure 3.11 shows the density field after 5.25×10^{-4} s, as evaluated by a full DSMC simulation on a grid of 200×300 cells, with a time step $\Delta t = 5 \times 10^{-7}$ s and $\approx 2 \times 10^6$ particles, illustrating the structure of the jet. In particular, one recognizes the initial weak shock wave (B1), the jet front (S1), a normal shock (S2), a shear layer (SH) and the starting evolution of an expansion region near the lips of the slit (E) according to the description in [102].

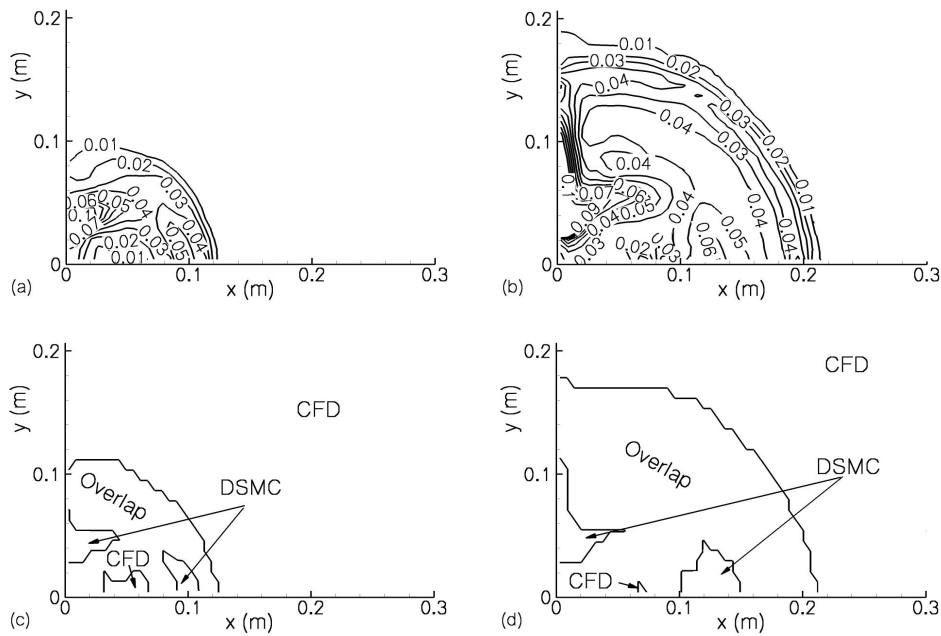


Figure 3.12: Contours of the continuum breakdown parameter Kn_{max} after 2.10×10^{-4} s (a) and after 5.25×10^{-4} s (b), and CFD/DSMC domain splitting after 2.10×10^{-4} s (c) and after 5.25×10^{-4} s (d).

From symmetry considerations we limit the simulation domain to the upper half of the flow domain which extends for a length $l_x = 0.4$ m in the x direction and $l_y = 0.5$ m in the y direction.

The thermodynamic conditions inside the infinitely large left tank remain constant, thus it can be modelled with an inlet boundary condition.

The initial grid is composed of 120 cells in the x direction and 60 cells in the y di-

rection. The code automatically refines the mesh in the DSMC region to fulfill its requirements. The coupling time step is $\Delta t_{\text{coupling}} = 2.0 \times 10^{-6}$ s, which corresponds to a coupling Courant number $C \approx 0.75$. The ensemble averages of the DSMC solution were made on 50 repeated runs.

In figure 3.12 the continuum breakdown parameter Kn_{max} in the jet is shown after 2.10×10^{-4} s (a) and 5.25×10^{-4} s (b), together with the division between the DSMC, CFD and overlap regions in the hybrid CFD/DSMC approach. Outside the jet, because of the absence of gradients, gradient length scales are large and Kn_{max} (using local values of Q_{ref}) is low. In the complex structure of the jet, Kn_{max} is particularly high in the expansion region E (where the mean free path is higher), in the shocks (B1 and S2) and in the jet front (S1) because of the small gradient length scales due to the high gradients. In the hybrid CFD/DSMC approach, CFD is therefore particularly applied outside the jet, whereas the use of DSMC is especially required in the expansion E and in the region of the jet front S1 and the shock S2. Comparing figures 3.12(c) and 3.12(d), it is possible to see the adaptation of the DSMC and CFD regions to the evolution of the flow field.

In figure 3.13 the density fields evaluated by the hybrid CFD/DSMC approach after 2.10×10^{-4} s and 5.25×10^{-4} s are compared to the results of full DSMC and CFD simulations. The full DSMC solution is considered to be the most accurate of the three.

Comparing figures 3.13(a), (b) and (c) to figures 3.13(d), (e) and (f) respectively, one can see the evolution of the jet in time, predicted by the three methods. It is interesting to note how the elements of the jet, that are not clearly distinguishable after 2.10×10^{-4} s begin to have a clear shape and identity after 5.25×10^{-4} s.

In figure 3.13, the hybrid method results in much better agreement with the DSMC than the full CFD simulations. The differences between the CFD and the other two methods increase in time and after 5.25×10^{-4} s the jet predicted by the CFD method covers a too wide region and the density after the shock S2 is too low if compared to the DSMC results.

In order to have a more quantitative validation of the hybrid approach, figure 3.14 shows the density along the x direction for the hybrid method, the full CFD simulation and the full DSMC simulation after 2.10×10^{-4} s (a) and 5.25×10^{-4} s (b). While the results obtained with the hybrid approach are virtually identical to those obtained with the full DSMC solver, significant differences, which increase in time, can be observed between the full CFD and DSMC approaches. In particular in the full CFD results the jet travels slightly faster and the density after the shock S2 is lower.

Finally, the crucial fact to emphasize is that the hybrid results were obtained in $\sim 1/10$ of the CPU time needed by the full DSMC method.

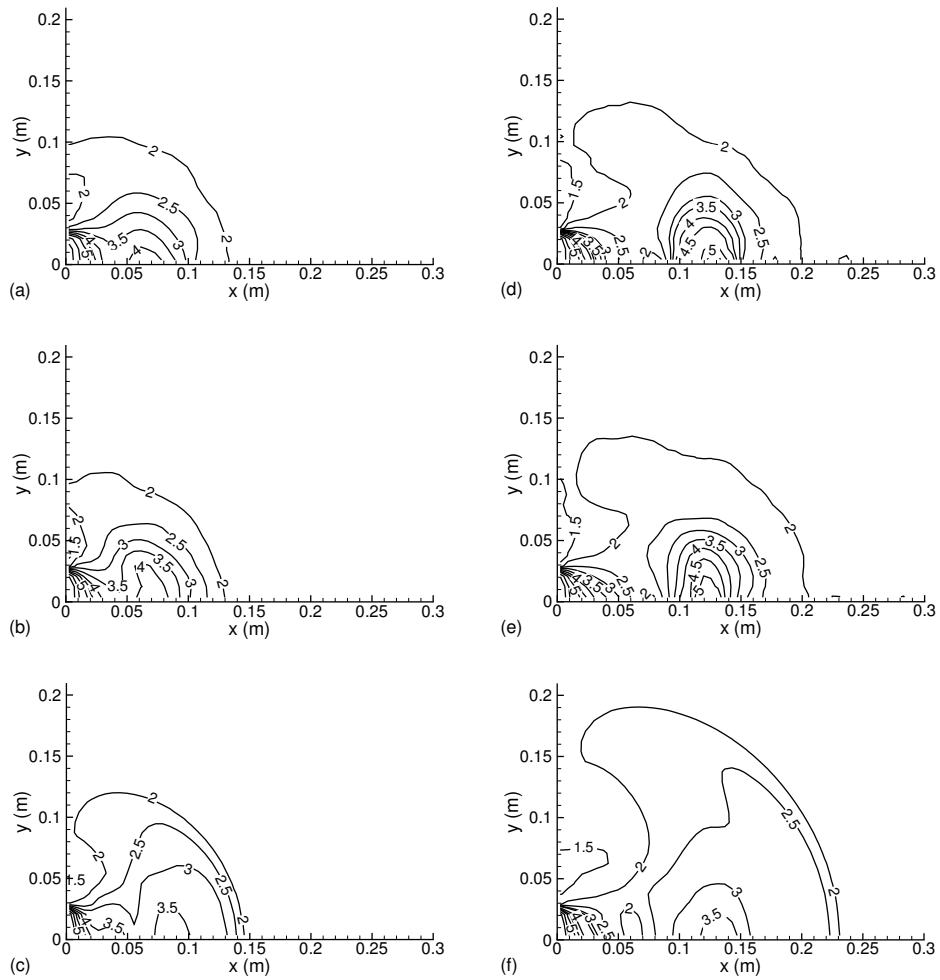


Figure 3.13: Density field (10^{-5} kg/m³) in the jet after 2.10×10^{-4} s evaluated by DSMC (a), hybrid simulations (b) and CFD (c), and after 5.25×10^{-4} s evaluated by DSMC (d), hybrid simulations (e) and CFD (f).

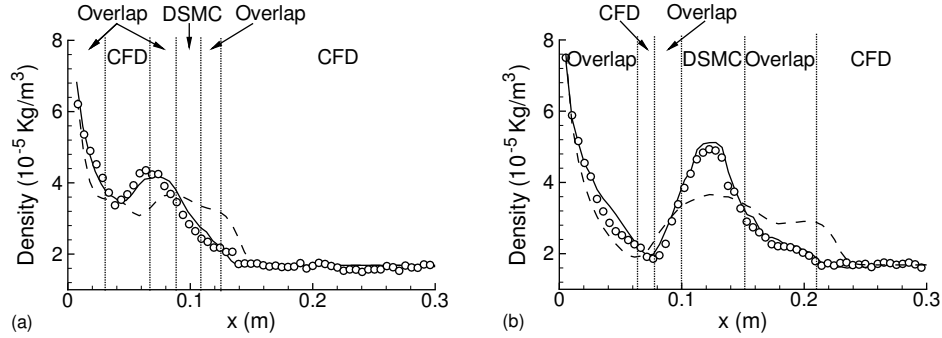


Figure 3.14: Density profile along the x direction after 2.10×10^{-4} s (a) and after 5.25×10^{-4} s (b). DSMC (\circ), Hybrid simulations ($-$), CFD ($- -$).

3.5.3 Rarefied Poiseuille flow

The steady-state coupling method in two dimensions was applied to a plane Poiseuille flow (figure 3.15).

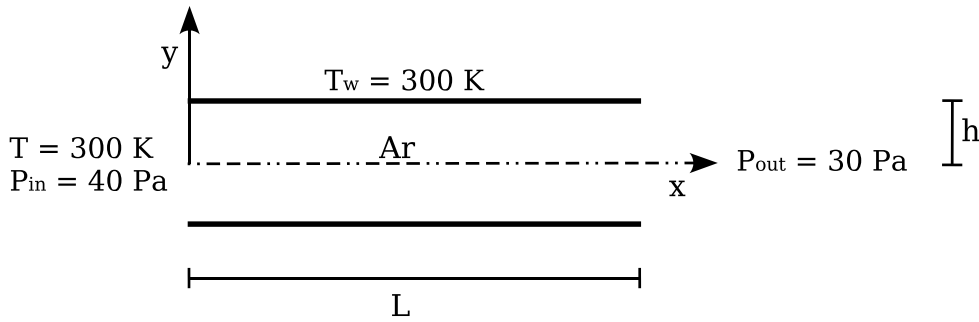


Figure 3.15: Rarefied Poiseuille flow.

We consider a flow of Argon at a temperature $T = 300$ K in a small channel of height $2h = 0.01$ m and length $L = 0.05$ m. The pressure at the inlet is $P_{\text{in}} = 40$ Pa and at the outlet $P_{\text{out}} = 30$ Pa. The average mean free path is approximately $\lambda \approx 10^{-4}$ m. The wall temperature is $T_w = 300$ K. At a sufficient distance from the inlet the flow is a Poiseuille flow: its solution under continuum conditions is known and characterized by a linear pressure decay in the x direction and a parabolic velocity profile in the y direction. From symmetry considerations we limit the simulation domain to

the upper half of the channel. The continuum grid is composed of 50 cells in the x direction and 10 cells in the y direction.

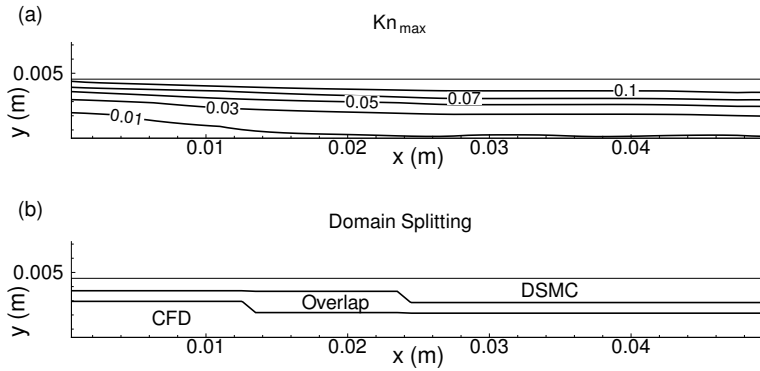


Figure 3.16: Rarefied Poiseuille flow: Contours of the continuum breakdown parameter Kn_{\max} (a) and CFD/DSMC domain splitting (b)

In figure 3.16(a) the continuum breakdown parameter is shown. Since temperature, pressure and density do not vary strongly throughout the domain, the continuum breakdown parameter identifies with the Knudsen number based on the local velocity gradient length scale ($\text{Kn}_{\max} = \text{Kn}_V$)

$$\text{Kn}_V = \frac{\lambda}{V_0} |\nabla V| \quad (3.6)$$

As a reference velocity, we used V_0 at the symmetry plane under continuum conditions, rather than the local velocity V , since the latter approaches zero near the wall

$$V_0 = \frac{h^2}{2\mu} \frac{\Delta P}{L} \quad (3.7)$$

where μ is the viscosity of the fluid and $\Delta P = P_{\text{in}} - P_{\text{out}}$.

The velocity gradient is small near the axis and large near the wall. This means that the continuum breakdown parameter is high near the wall and low near the axis. In figure 3.16(b), the resulting division between the DSMC, CFD and overlapping regions is shown.

In figure 3.17(a) we compare the pressure drop along the x direction predicted by the hybrid method to the pressure drop obtained from a full DSMC simulation. Results obtained with a full CFD simulation with no-slip, as well as with velocity slip boundary conditions, and the theoretical linear pressure drop for continuum conditions are

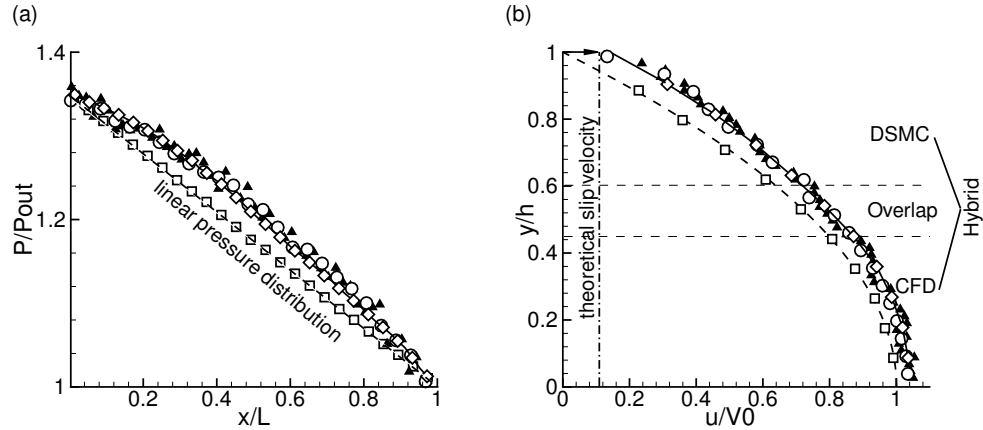


Figure 3.17: Poiseuille flow pressure drop in the x direction (a) and velocity profile at $x = 0.04$ m (b). Theoretical continuum Poiseuille solution with no-slip BC (---), CFD with no-slip BC (\square), CFD with velocity slip BC ($-\diamond-$), DSMC (\blacktriangle), Hybrid (\circ).

also shown.

From figure 3.17(a), it is clear that while the full CFD approach with no-slip boundary conditions predicts a linear pressure drop, the hybrid approach, the DSMC method and the full continuum simulation with velocity slip boundary conditions show the non linear pressure drop which is known to be present in rarefied Poiseuille flow [85; 86]. In figure 3.17(b) the velocity profile at $x = 0.04$ m from the hybrid CFD/DSMC method is compared to the results of a full DSMC simulation, results obtained with a full CFD simulation both with no-slip and with velocity slip boundary conditions, and the theoretical solution for continuum Poiseuille flow.

The coupled CFD/DSMC method, the full DSMC simulation and the full CFD simulations with slip boundary conditions give very similar results for the velocity profile, describing a slip velocity at the wall. The computed slip velocity agrees very well with the theoretical prediction [85]. It is also obvious that the slip effect increases the average velocity in the channel at given total pressure drop and reduces the curvature of the velocity profile with respect to the continuum solution [85].

3.6 Conclusions

In this chapter the development and validation of a hybrid continuum-rarefied method for multiscale flow simulation was presented.

The method couples a compressible Navier-Stokes description of a macroscale continuum gas flow with a molecular scale DSMC description of a rarefied gas flow in both

steady-state and unsteady conditions.

Transient simulations of a one-dimensional shock-tube and a two-dimensional pressure-driven slit flow with the proposed method were successfully validated against full DSMC simulations. The same has been done for two-dimensional steady state simulations of a rarefied Poiseuille flow.

The results of the method were found to be independent of the size of the overlap region and the CFD/DSMC interface position as long as we ensure to run the CFD in the limits of its applicability ($Kn \lesssim 0.1$). The method also has limited sensitivity to noise, as demonstrated by its insensitivity to the number of DSMC runs for ensemble averaging to reduce scatter. However, in order to avoid instability effects the coupling time step and the CFD cell size should be chosen such, that the Courant number based on these quantities and on the molecular most probable velocity is ≤ 1 . These validation studies illustrate the potential of the method for steady and transient, one-dimensional and multi-dimensional flows.

4. Influence of rarefaction on a supersonic hot gas expansion

In this chapter the hybrid CFD/DSMC approach described and validated in the previous chapter is used to study the gas dynamics of a stationary hot gas jet supersonically expanding into a low pressure environment. Our study demonstrates: (i) the necessity of applying a molecular approach where rarefaction effects are present in order to correctly model the flow, and (ii) an invasion of the supersonic part of the flow by background particles.

Most of the chapter has been published as 'The influence of rarefaction on the flow dynamics of a stationary supersonic hot gas expansion' by G. Abbate, B.J. Thijsse, R. Engeln, M.C.M. van de Sanden, D.C. Schram and C.R. Kleijn in *Phys. Rev. E* [104], and as 'Multi-Scale Modelling of the two-dimensional Flow Dynamics in a Stationary Supersonic Hot Gas Expansion' by G. Abbate, B.J. Thijsse, and C.R. Kleijn in *LNCS* [112].

4.1 Introduction

Several gas fluidic applications of current technological importance involve a gas jet supersonically expanding into vacuum or into a low pressure environment. Examples include: gas thruster nozzles and plume flows [97] and processes of thin film deposition, etching and passivation from expanding plasma or gas jets [105].

An interesting issue connected to this kind of flows is the transition from continuum to rarefied regime. The gas in the jet is generally at relatively high pressure, and then it rapidly expands into a low pressure environment. For this reason, the gas first supersonically expands and then quickly compresses through a stationary shock wave (the so called Mach disk). In addition, the expansion zone is surrounded by a barrel shaped shock (the so called barrel shock) as depicted in figure 4.1. Because of the low environment pressure and high thermodynamic gradients in the shock region, the flow undergoes a spatial transition from the low Knudsen number (Kn) continuum regime to the high Knudsen number rarefied regime.

Although several studies have been devoted to supersonic expansion of gas jets in

72 Chapter 4. Influence of rarefaction on a supersonic hot gas expansion

vacuum or low pressure environment [18; 19; 20; 21; 22; 23; 24; 25; 26; 28; 31; 106; 107; 108; 109; 110; 111; 115], full understanding of the processes governing the flow has not been reached yet. In particular, it is still not completely clear how important the influence of the rarefaction effects is on the dynamics of the flow [31]. Another important question is whether the barrel shock, which becomes transparent to background molecules due to rarefaction effects, still protects the supersonic part of the flow [21]. We call background molecules the molecules that are present outside the expansion-shock region. These background molecules could, therefore, invade the supersonic part of the jet, influencing its properties. Already Fenn and Anderson in 1966 [106] and Campargue in 1970 [107] predicted this phenomenon, but a full understanding of it has not yet been given.

In the current chapter these last two issues will be addressed: (i) the importance of rarefaction effects on the flow field and (ii) the study of the presence of background particles in the supersonic region. These issues will be studied through detailed numerical simulations of the flow, pressure and temperature distributions in the expanding jet and its surroundings.

It has been shown [31] that, because of rarefaction effects, the continuum CFD (Computational Fluid Dynamics) approach fails in predicting temperature and velocity fields in the shock region. These can be correctly studied only with the help of kinetic simulations accounting for rarefaction and non-equilibrium effects. For this reason, in the past, DSMC (Direct Simulation Monte Carlo) has been used [31], but with a too coarse mesh in the near-inlet region. However, because DSMC computational expenses scale with Kn^{-4} , it is practically impossible to fulfill the DSMC requirements (e.g. the mesh size should be smaller than one third of the mean free path), especially near the inlet, where the Knudsen number is quite low [31].

In order to overcome this problem and to accurately simulate the above types of gas flows, one needs to construct a model that on the one hand accounts for the molecular nature of the gas flow where needed, and on the other hand uses a continuum model where allowed. In the past years several hybrid continuum/molecular models have been proposed [7; 8; 10; 12; 14; 16; 101].

In particular in our work we use a hybrid coupled continuum-DSMC approach [101] to model the problem; we apply the continuum CFD approach in the wide continuum region in order to save computational time, and DSMC only in the expansion-shock region where it is necessary in order to correctly model the rarefied nature of the flow. In section 4.2 we first describe the studied configuration and experiments used to validate our simulations. A brief explanation of the hybrid numerical simulation method, already extensively described in the previous chapter, is given in section 4.3. The results of our simulations of a stationary supersonic hot gas expansion are presented in section 4.4 and compared against (published) experimental data [21; 113; 114; 115]. In particular in this section we focus on the rarefaction effects, and we show a numerical demonstration of the invasion of the supersonic region by the background

molecules.

4.2 Studied configuration and measurement technique

In order to have an experimental support to our conclusions, all our numerical results will be validated by comparing them to experimental measurement by Engeln et al. [21], Mazouffre et al. [113], Vankan et al. [114] and Gabriel et al. [115].

The measurements described in [21; 113; 114; 115] were performed on an expanding thermal plasma jet. Nevertheless, because of the low ionization degree ($< 0.1\%$ due to the admixture of a few % of H_2 [20]), they can be used to validate our present results on a neutral gas flow, composed only of Argon atoms, neglecting the presence of H_2 , electrons and ions [21] and the effects of ionization and recombination on the flow field. It has been shown, in fact, that ionization is practically absent in this flow [21], and even if the recombination can be significant, it affects only the electron temperature field and not the gas temperature and velocity fields [32].

The experimental set-up in which the expanding thermal plasma jet is created has been extensively described elsewhere [30].

Two techniques, the Thomson-Rayleigh and the laser induced fluorescence spectroscopy (LIF), have been used to study the flow. The latter provided detailed, two-dimensional information on the velocity field. A description of the two techniques is given in [21; 114].

Although the LIF measurements are performed on Argon atoms in the metastable and resonant states, it is argued in [21] that the velocity distribution of these atoms reflects the velocity distribution of the ground state atoms.

4.3 Numerical simulation method

As already described in the previous chapters, in order to properly characterize the various regimes in the gas flow, the Knudsen number Kn is defined as the ratio between the mean free path and a relevant macroscopic length scale. When Knudsen is small ($Kn < 0.01$), the gas may be treated as a continuum and the gas flow may be modelled using CFD (Computational Fluid Dynamics). When Knudsen is large ($Kn > 10$), the gas behavior is entirely molecular and may be modelled using Molecular Dynamics techniques. In the intermediate regime, the DSMC (Direct Simulation Monte Carlo) approach is the most commonly used simulation technique. However, its computational expenses scale with Kn^{-4} , and become very time demanding for Kn smaller than ≈ 0.05 .

In order to overcome this dilemma and accurately solve the flow throughout the expanding gas jet, we use the hybrid CFD/DSMC model presented in the previous chapter, which takes into account the molecular nature of the gas flow where needed,

and uses a continuum model where allowed.

In the CFD code, temperature dependent viscosities and thermal conductivities are computed from kinetic theory [33]. The pressure is computed from the ideal gas law. In the DSMC code, in order to accurately model viscous effects, the Variable Soft Spheres (VSS) model is used to calculate particle cross sections. For the implementation of inlet or outlet boundary conditions, a "buffer zone" or "particle reservoir" approach is used [67]. A Chapman-Enskog [44] distribution is used to create particles in those reservoirs. The Chapman-Enskog distribution is obtained as an approximate solution of the Boltzmann equation and is expressed as a product of a local Maxwellian and a polynomial function of the thermal velocity components. It has been demonstrated that in a hybrid continuum-DSMC method a Chapman-Enskog distribution, rather than a simple Maxwellian distribution, is required when the viscous fluxes are taken into account [12; 100].

As discussed in section 3.2, an important issue in a hybrid continuum-DSMC simulation is how to determine the appropriate computational domains for the DSMC and continuum solvers, and the proper interface boundary between these two domains. The continuum breakdown parameter Kn_{\max} [98] is employed in the present study as a criterion for selecting the proper solver

$$\text{Kn}_{\max} = \max[\text{Kn}_{\rho}, \text{Kn}_V, \text{Kn}_T] \quad (4.1)$$

where Kn_{ρ} , Kn_V and Kn_T are the local Knudsen numbers based on density, velocity and temperature length scales, according to

$$\text{Kn}_Q = \frac{\lambda}{Q_{\text{ref}}} |\nabla Q| \quad (4.2)$$

Here, Q is a flow property (density ρ , velocity V or temperature T) and λ is the local mean free path length. Q_{ref} is a reference value for Q , which can either be its local value, or a typical value. If the calculated value of the continuum breakdown parameter in a region is larger than a limiting value Kn_{split} , then that region cannot be accurately modelled using the continuum approach, and DSMC has to be used. For Kn_{split} a value of 0.05 was used. The described Schwarz method has been found to be rather insensitive to the precise CFD/DSMC interface location w.r.t. Kn_{split} , as shown in the previous chapter.

Between the DSMC and CFD regions an overlap region is considered, where the flow is computed with both the DSMC and the CFD solver. This overlap region is chosen to be located entirely in the $\text{Kn}_{\max} > \text{Kn}_{\text{split}}$ region.

4.3.1 Modelled geometry

The computational domain (figure 4.1) is a $d = 32$ cm diameter cylinder of length $L = 50$ cm. From a circular hole of diameter $d_{\text{in}} = 8$ mm, on its top, a flow of 56 sccs of

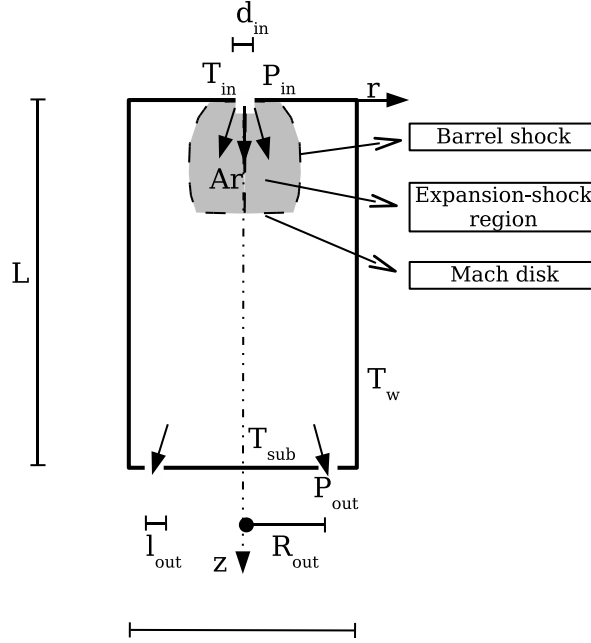


Figure 4.1: Scheme of the low pressure chamber. (Diagram not to scale).

Argon is injected at a temperature $T_{in} = 8000$ K. Uniform velocity and temperature profiles are imposed at the inlet for two reasons. (i) It has been experimentally observed that the hot plasma does experience slip at the nozzle wall [31]. (ii) Upstream from the inlet, the flow passes through a channel of length $l = 4$ cm and diameter $d = 4$ mm. Since the Reynolds number in the channel is $Re \approx 1500$, the necessary length to develop a parabolic profile is $0.04 Re d \approx 24$ cm $\gg l$. Therefore, we do not expect to experience a parabolic profile at the inlet of the chamber.

The top and lateral walls are at a temperature $T_w = 400$ K, while the bottom wall, which represents the substrate, is at a temperature $T_{sub} = 600$ K.

The pumping exit, which in reality is a circular hole, in our 2-D model has been represented as a $l_{out} = 2$ cm wide ring on the bottom of the cylinder at a distance of $R_{out} = 12$ cm from the axis. Two different pressures P_{out} in the exit have been considered, respectively 20 and 100 Pa, since for these outlet pressures a large amount of experimental data is available [21; 113; 115].

Inside the chamber we suppose the flow to be 2-D axi-symmetric. The continuum grid is composed of 100 cells in the radial direction and 200 cells in the axial direction.

76 Chapter 4. Influence of rarefaction on a supersonic hot gas expansion

The cells are slightly stretched in the radial direction with a ratio of 1.65 between the size of the last and the first cell. Grid independence has been tested by doubling the continuum grid in each of the two directions, leading to variations in the solution below 3%. The code automatically refines the mesh in the DSMC region to fulfill its requirements as explained in chapter 2. The number of simulated particle in the DSMC region is $N \approx 8 \cdot 10^5$.

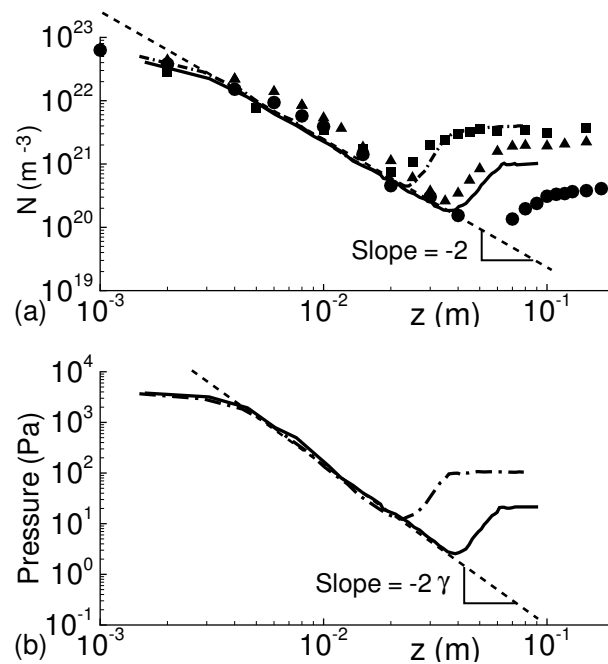


Figure 4.2: Number density (a) and pressure (b) distributions along z -axis in the expansion-shock region. Hybrid approach at 20 Pa (—), Hybrid approach at 100 Pa (- · -), Theoretical trend in the expansion (---), Experimental number density distribution from [114] at 10 Pa (●) and at 40 Pa (▲), and from [113] at 100 Pa (■).

4.4 Results and discussion

4.4.1 General flowfield characteristics and rarefaction effects

In figure 4.2 the number density (a) and pressure (b) profiles along the z -axis in the expansion-shock region, as evaluated by the hybrid approach for the two considered chamber pressure conditions (respectively 20 and 100 Pa) are shown. It is

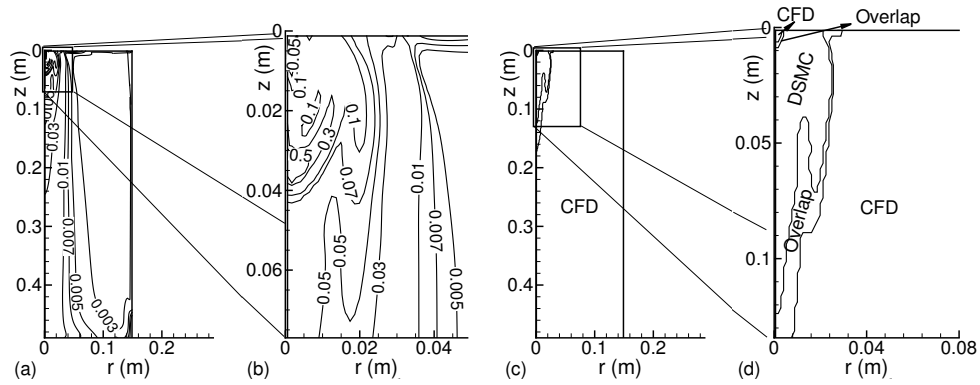


Figure 4.3: Contours of the continuum breakdown parameter Kn_{max} in the entire chamber (a), and zoomed in to the expansion-shock region (b), CFD/DSMC domains splitting in the entire chamber (c), and zoomed in to the expansion-shock region (d), for 20 Pa chamber pressure.

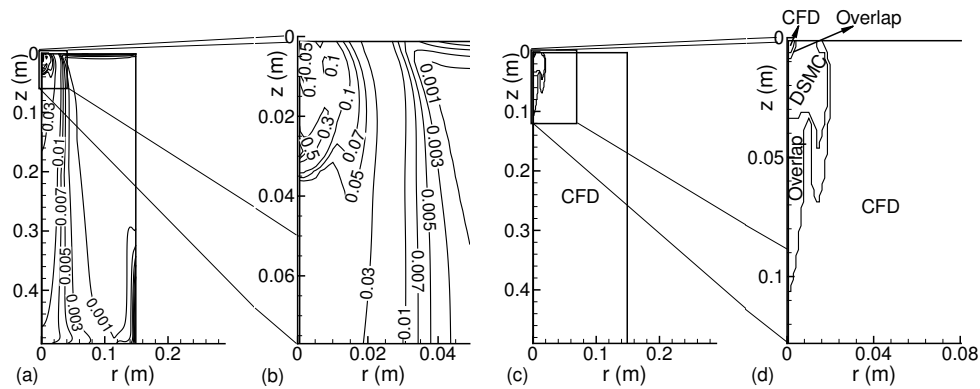


Figure 4.4: Contours of the continuum breakdown parameter Kn_{max} in the entire chamber (a), and zoomed in to the expansion-shock region (b), CFD/DSMC domains splitting in the entire chamber (c), and zoomed in to the expansion-shock region (d), for 100 Pa chamber pressure.

well known [116] that, in the expansion, the density decreases quadratically with the distance z to the inlet ($1/z^2$), whereas the pressure has a $1/z^{2\gamma}$ dependence, where γ is the specific heat ratio (for Argon $\gamma = 1.67$). In figure 4.2(a), the number density profiles measured with the Thomson-Rayleigh technique by Mazouffre et al. [113] at 100 Pa, and by Vankan et al. [114] at 40 and 10 Pa chamber pressures are also presented. The present hybrid results are in very good agreement with experimental data by Mazouffre et al. at 100 Pa [113], and even if no density measurements were available at 20 Pa chamber pressure, the present hybrid results are exactly between the experimental data at 40 and 10 Pa chamber pressures measured by Vankan et al. [114].

In order to describe the effects of rarefaction on the flow field, it is important to identify the region where these effects take place.

For this reason, in figures 4.3 and 4.4 we show the continuum breakdown parameter Kn_{max} in the chamber and the consequent division between the DSMC, continuum and overlapping regions in our hybrid method, respectively for 20 and 100 Pa chamber pressures.

In both 20 and 100 Pa chamber pressure cases, there are various counteracting effects influencing the value of Kn_{max} : as a result of the decrease in pressure, the mean free path increases from the inlet to the exit of the chamber. As a result of the cooling of the gas, the temperature decreases from the inlet to the exit of the chamber and the opposite effect occurs. And finally, smaller local gradient length scales are present near the inlet and in the shock, than in the rest of the chamber. The overall effect is that the continuum breakdown parameter is small near the inlet, then it increases becoming high in the expansion-shock region, and finally it becomes low again in the rest of the chamber. Also near the substrate wall the continuum breakdown parameter increases, due to steep velocity and temperature gradients, but not to values exceeding Kn_{split} . This means that the flow first undergoes a continuum-rarefied transition in the near-inlet region, and then a rarefied-continuum transition downstream of the shock (figures 4.3(b) and 4.4(b)). By comparing figure 4.3(a) to figure 4.4(a), it is also clear that, as expected, the overall values of the continuum breakdown parameter decrease if we increase the pressure in the chamber. As a consequence of that, going from 20 Pa to 100 Pa, the size of the region where the use of DSMC is necessary to correctly model the flow is reduced (figures 4.3(d) and 4.4(d)).

Temperature and velocity fields obtained with the hybrid CFD/DSMC at 20 and 100 Pa chamber pressures are compared to results from a full continuum CFD simulation in figures 4.5-4.7.

It should be noted that DSMC simulations intrinsically contain statistical scatter, explaining why the contours in the hybrid simulations are less smooth than in the continuum simulations. From an analysis of the figures, it is evident that far away from the expansion-shock region, the continuum and hybrid methods give very similar results (figure 4.5(a) and (c), and figures 4.6(a) and (c)). The use of DSMC in the

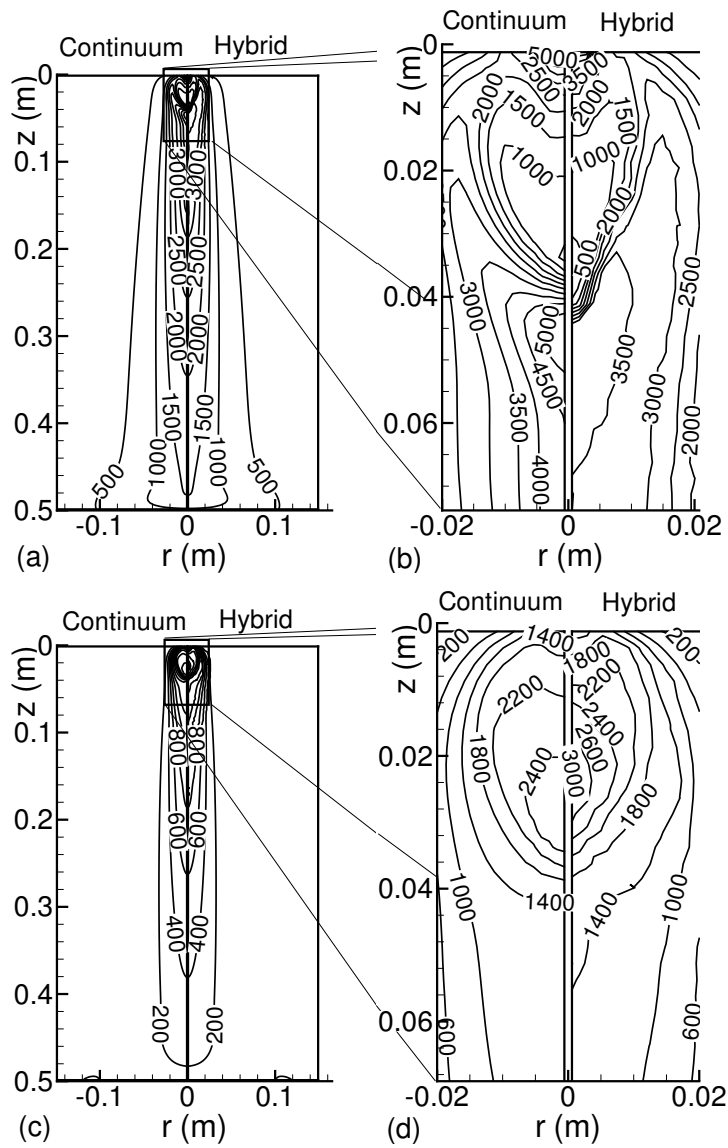


Figure 4.5: Temperature field (K) in the entire chamber (a), and zoomed in to the expansion-shock region (b) and velocity field (m/s) in the entire chamber (c), and zoomed in to the expansion-shock region (d), for 20 Pa chamber pressure.

hybrid method influences only the region where rarefaction effects are present. Far away from the expansion-shock region, the influence of rarefaction effects is negligible. As expected, the continuum and hybrid approaches differ more at 20 Pa chamber pressure than at 100 Pa, since stronger rarefaction effects are present at 20 Pa than at 100 Pa.

For the case of 20 Pa chamber pressure, it was also possible to compare the results of the present hybrid simulations to a detailed two-dimensional picture of the velocity field in the expansion-shock region measured by Gabriel et al. [115], and to results from full DSMC simulations by Selezneva et al. [31].

Figure 4.7(a) indicates the region where the comparison has been performed and the division between the DSMC, continuum and overlapping regions in our hybrid method. In figures 4.7(b)-(e) the comparison between experimental data from [115], results from the present hybrid method, results from full DSMC simulations performed by Selezneva et al. [31], and results from present continuum simulations for the two-dimensional velocity field in the expansion-shock region are presented. The velocity contours in figure 4.7(b) are the result of an interpolation of measured velocities at various positions in the expansion-shock region [115]. The hybrid method is in much better agreement with experimental data than the other approaches. The reason why the hybrid approach predicts experimental data even better than the full DSMC simulations is that, as discussed in section 4.1 and as already highlighted by Selezneva et al. [31], in the full DSMC simulations it was not possible to respect DSMC requirements in the near inlet region and a too coarse mesh had to be used.

If we first compare the experimental data from [115] (figure 4.7(b)) to the results of the full CFD approach (figure 4.7(e)), the velocity predicted by the continuum approach in the expansion-shock region is significantly (200 – 500 m/s) lower than the experimental one. Because of rarefaction, in fact, upstream of the shock the expansion is stronger, reaching higher velocity values.

If we compare the experimental data from [115] (figure 4.7(b)) to the full DSMC simulations by Selezneva et al. [31] (figure 4.7(d)), we can notice that the DSMC predicts correct velocity values in the expansion, but the maximum velocity along the z -axis is moved ≈ 1 cm upstream with respect to the experimental data.

Finally, hybrid simulations (figure 4.7(c)) result in a very good agreement with the experiments (figure 4.7(b)); The hybrid approach, in fact, was able to predict the correct velocity values and the right position for the velocity peak in the expansion. Summarizing, at 20 Pa the hybrid method predicts a stronger expansion compared to the continuum method, reaching a lower temperature (figure 4.5(b)) and higher velocity (figure 4.7). Also, compared to the full continuum simulation, the shock is slightly moved downstream along the z axis in the hybrid simulation. Finally, after the shock the temperature predicted by the hybrid method is significantly (500 – 1500 K) lower than the one calculated by the continuum approach.

At 100 Pa only small differences between the continuum and hybrid methods are

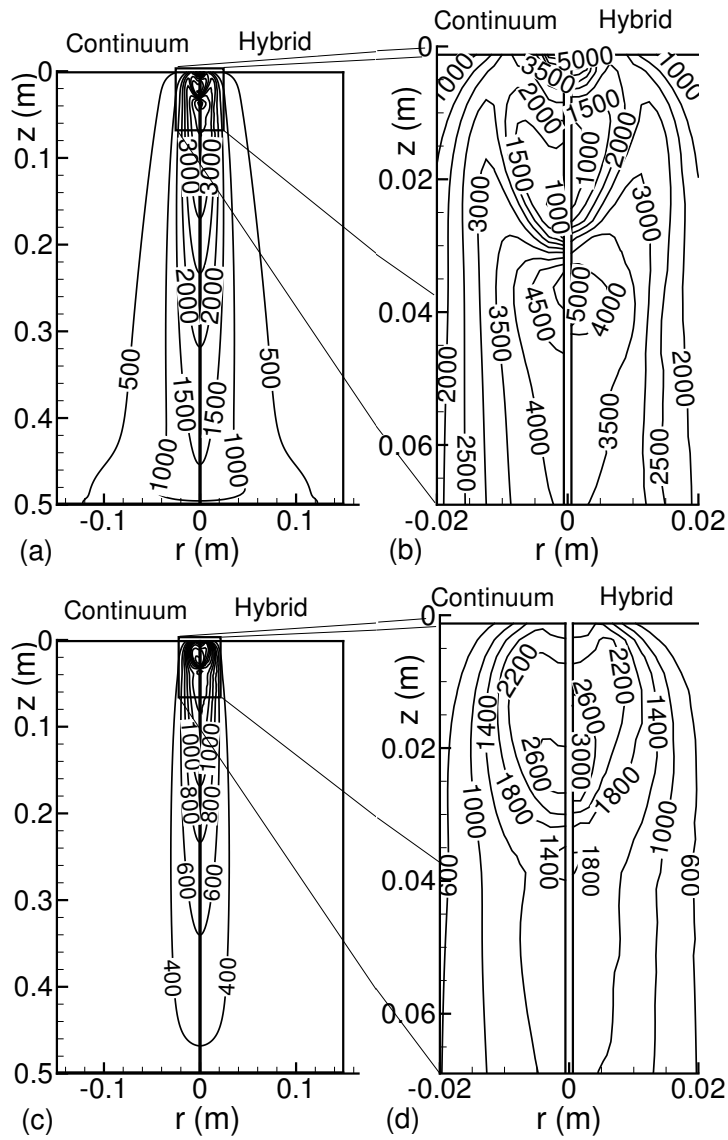


Figure 4.6: Temperature field (K) in the entire chamber (a), and zoomed in to the expansion-shock region (b) and velocity field (m/s) in the entire chamber (c), and zoomed in to the expansion-shock region (d), for 100 Pa chamber pressure.

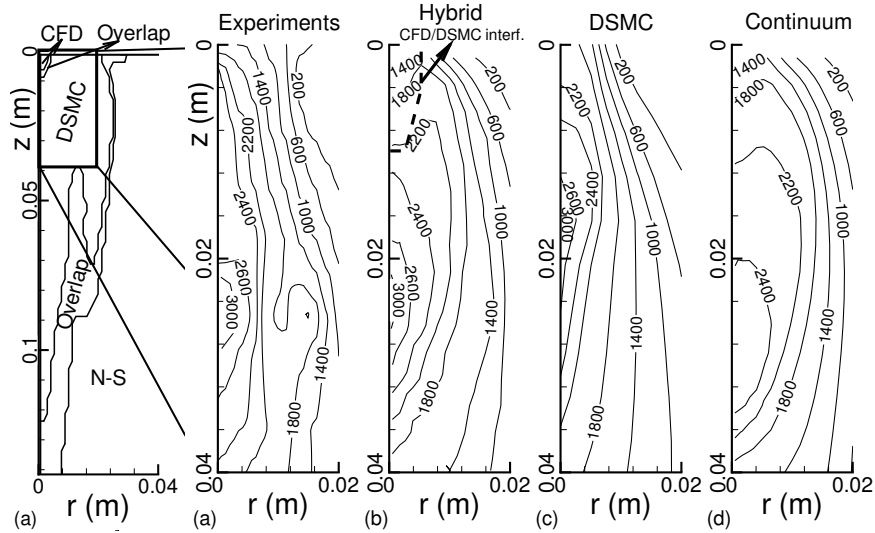


Figure 4.7: CFD/DSMC domains splitting (a) and velocity field (m/s) zoomed in the expansion-shock region at 20 Pa chamber pressure. Experimental data from [115] (b), present hybrid simulations (c), DSMC data from [31] (d), present continuum simulations (e).

present in the temperature fields (figure 4.6(b)). The differences in the velocity fields, on the contrary, are more significant (figure 4.6(d)); in the expansion, in fact, the hybrid method reaches higher values of the velocity than the continuum approach. The position of the shock is the same and both methods describe a further small expansion and shock after the first stronger ones.

In order to further clarify the effects of rarefaction on the flow field, and to have a more quantitative validation of the hybrid approach, figures 4.8 and 4.9 show, respectively for the temperature and the velocity along the z axis, a comparison between the present hybrid method, the present continuum simulation, results from full DSMC simulations performed by Selezneva et al. [31], and experimental data from [21] at both 20 Pa (a) and 100 Pa (b) chamber pressures. Although there is quite some scattering in the experimental data, in all cases it is clear that the hybrid method predicts the experimental data better than the other approaches.

If we first compare the results of the hybrid CFD/DSMC approach to those of the full CFD approach, figure 4.8(b) shows that even at 100 Pa chamber pressure, the hybrid approach follows much better than the continuum approach the experimental data in the shock and after-shock region. As we reduce the chamber pressure (figure 4.8(a)), we further increase the rarefaction effects. In the continuum approach the shock wave

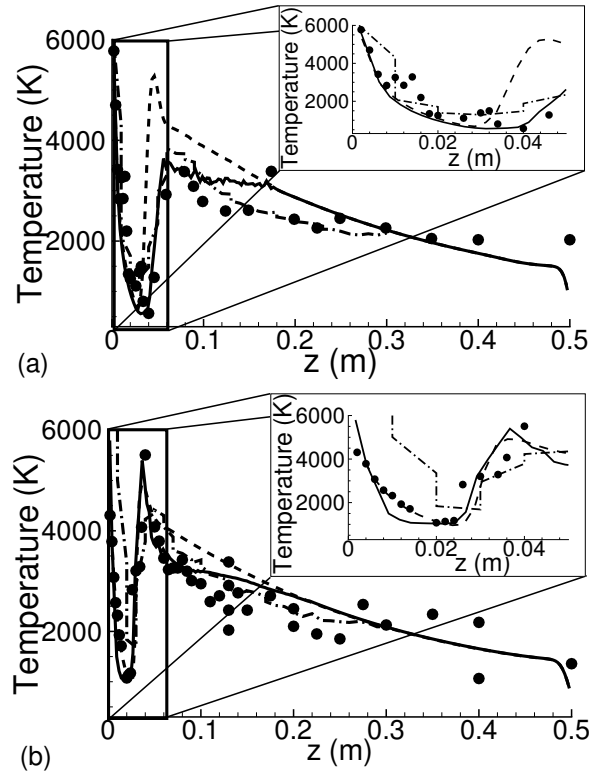


Figure 4.8: Temperature distribution along z -axis for 20 Pa (a), and 100 Pa (b) chamber pressures. Continuum (---), DSMC data from [31] (- · -), Hybrid (—), Experimental data from [21] (•).

appears too early and the temperature after the shock is too high, whereas in the hybrid approach the shock moves forward due to rarefaction and the temperature after the shock is lower.

Figure 4.9 demonstrates that the continuum approach is unable to quantitatively predict the velocity profile and maximum velocity in the expansion-shock region at either 20 Pa (a) or 100 Pa (b) chamber pressures, and is quantitatively correct only downstream of the expansion-shock region as already shown in [31]. Because of rarefaction, upstream of the shock the expansion is stronger, reaching higher velocity values at both 20 and 100 Pa chamber pressure as predicted by the hybrid solution in agreement with the experimental data.

If we compare the hybrid method to the full DSMC simulations by Selezneva et al.

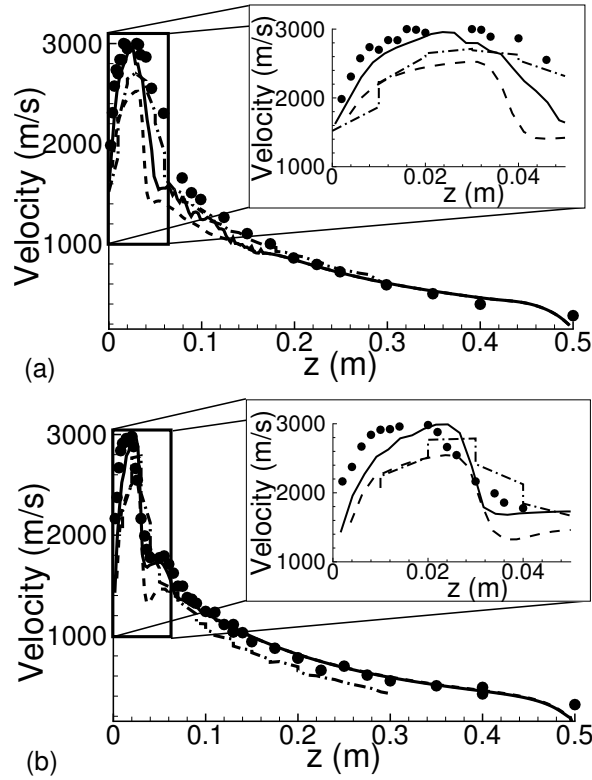


Figure 4.9: Velocity profile along z -axis for 20 Pa (a), and 100 Pa (b) chamber pressures. Continuum (---), DSMC data from [31] (- · -), Hybrid (—), Experimental data from [21] (●).

[31], we can notice that the results of the full DSMC simulations and the hybrid method are almost equivalent in the shock and after shock regions. However, in the near inlet and expansion regions, especially at 100 Pa chamber pressure, the hybrid approach matches the experimental data better than the full DSMC approach.

We can notice that even if at 20 Pa chamber pressure, the temperature profiles predicted by the DSMC alone and by the hybrid approach are very similar and they both accurately match the experimental data (figure 4.8(a)), increasing the chamber pressure to 100 Pa, and therefore enlarging the continuum region, the differences between the DSMC and the hybrid approach in the near inlet and expansion regions become more significant (figure 4.8(b)). The DSMC alone cannot follow the experimental data in the near inlet and expansion regions, and cannot predict the temperature

peak after the shock, while the hybrid solution results are in a very good agreement with experiments.

In an analogous manner, from figure 4.9 we can conclude that, because it was not possible to respect DSMC requirements in the near-inlet region, the DSMC method predicts a wrong velocity in this region that influences its solution also in the expansion region. As a result, DSMC predicted a too low value of the maximum velocity reached in the expansion at 100 Pa chamber pressures, whereas the hybrid approach accurately predicts this maximum.

4.4.2 Invasion of the supersonic region by background particles

In order to study the possible invasion of the supersonic region by the background molecules, during the simulations at 20 Pa chamber pressure, the particle velocity distribution functions were recorded at the positions where they have been measured experimentally by Engeln et al. [21].

In figures 4.10(a), (b) and (c), we compare the axial velocity distribution function of our simulated particles at $r = 0$, and $z = 26$ mm, $z = 59$ mm and $z = 100$ mm with the ones measured by Engeln et al. In the same way, in figures 4.10(d) and (e) we compare Engeln's radial velocity component distribution functions with our simulated ones at $z = 50$ mm and $r = 0$ and $r = 22$ mm. In [21], Engeln et al. expressed the measured velocity distribution functions in terms of the intensity of the recorded signal during the experiments and, therefore, the surface area below the experimental data is not equal to 1. In order to be able to compare our numerical data with the measured distributions, in figure 4.10 our curves were scaled by a factor equal to the surface area under the experimental curves. From figure 4.10, it is clear that there is a very good agreement between our current hybrid simulations and the experiments from [21].

If we compare the axial and radial velocity distribution functions of our simulations with a Maxwellian distribution (figure 4.10), we can affirm that downstream of $z \approx 30$ mm there is a clear departure from equilibrium.

In this section we want to demonstrate that this non-equilibrium is due to the invasion of background particles into the expansion-shock region. In continuum conditions, because of the presence of the shock, these particles would not be able to enter the supersonic region. However, we will show that, because of the rarefaction effects, the shock becomes transparent and does not protect the supersonic region. Therefore some particles may actually move into it from the subsonic part of the flow. To demonstrate this hypothesis, it is necessary to know the origin of the particles present in the supersonic region. For this reason, for the DSMC particles, two different labels were used; one for the particles which, after entering the reactor chamber, have always been in the supersonic region (the so called "inlet particles"), and a different one for

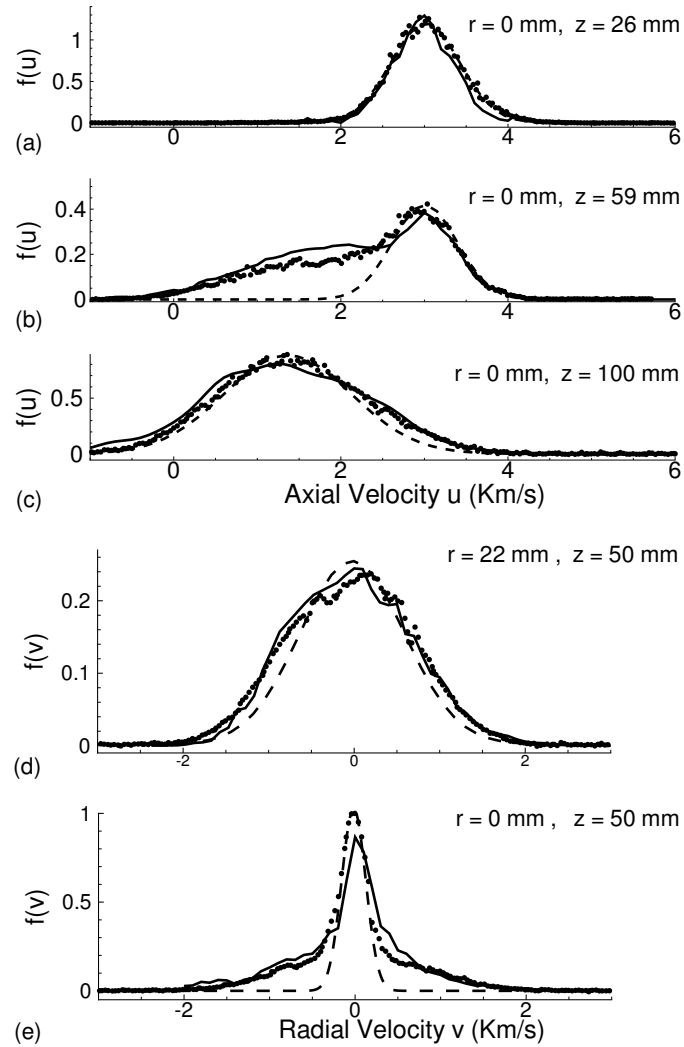


Figure 4.10: Axial velocity distribution at $r = 0$ and $z = 26$ mm (a), $z = 59$ mm (b) and $z = 100$ mm (c) and radial velocity distribution at axial position $z = 50$ mm and radial position $r = 0$ (d) and $r = 22$ mm (e), for 20 Pa chamber pressure. Hybrid simulation results (—), Maxwellian distribution (---), and experimental data from [21] (●).

the background particles.

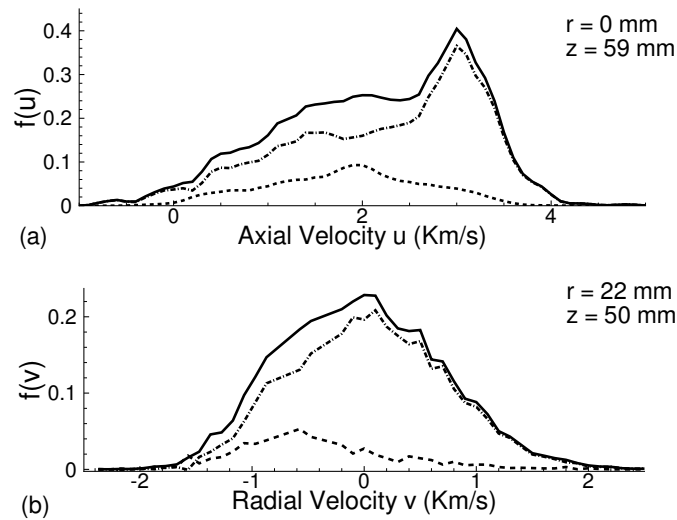


Figure 4.11: Relative contribution of background particles to the axial velocity distribution at $r = 0$ and $z = 59$ mm (a) and to the radial velocity distribution at $r = 22$ mm and $z = 50$ mm (b), for 20 Pa chamber pressure. Total velocity distribution (—), Inlet particles (- · -), Background particles (- -).

In figure 4.11(a) we show the contribution of the background particles and the inlet particles to the axial velocity distribution, at the position $r = 0$ and $z = 59$ mm, where the departure from the equilibrium is most clear. The presence of background particles in the supersonic region is evident. Once the background particles have penetrated the supersonic region, they start colliding and interacting with the particles that are already there, decelerating them and being accelerated by them. As a result, the velocity distribution of the "inlet particles" becomes non-Maxwellian.

In an analogous manner, in figure 4.11(b) the contribution of background and inlet particles to the radial velocity distribution at the position $r = 22$ mm and $z = 50$ mm is shown. It is interesting to note that the peaks of the two contributions are located on opposite sides of the zero velocity position. This means that while particles coming from the inlet are moving away from the axis because of the expansion, the background particles are penetrating into the supersonic region and moving toward the axis.

In order to further prove the hypothesis of the presence of background particles in the supersonic region and explain how they collide and interact with the local particles,

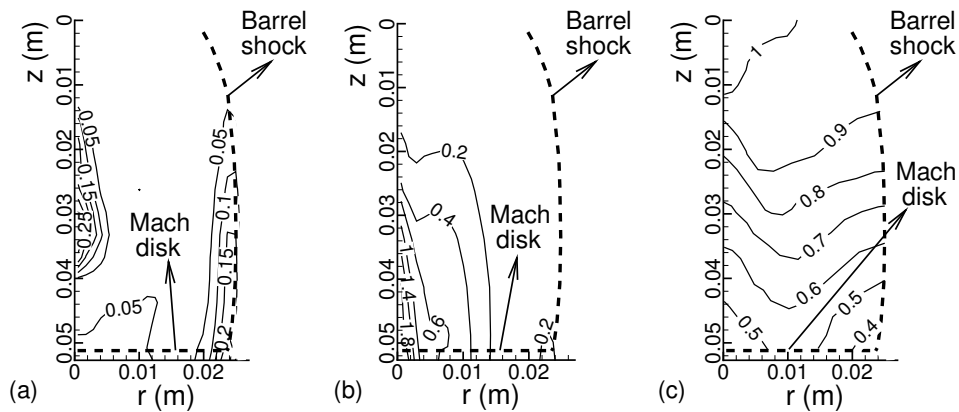


Figure 4.12: Fractional concentration of background particles in the supersonic region (a), average number of times that inlet particles have collided with background particles before reaching the given location (b), and fractional concentration of inlet particles which have never collided with background particles (c).

a study was performed, at the molecular scale, by tracking particles and collisions in the supersonic region. The results of this study are presented in figure 4.12.

The background particles concentration in figure 4.12(a) further proves their presence in the supersonic region.

In the expansion region, the velocity increases, reaching a maximum value on the axis at a distance $z \approx 3$ cm from the inlet (figure 4.9(a)), whereas density and pressure decrease reaching a minimum (figure 4.2) at the same location. The invading background particles are driven into the region of minimum pressure by favorable pressure gradients. For the same reason, once they are there, it is difficult for them to cross the Mach disk because of the adverse pressure gradient. Therefore, the invading background particles concentrate in the region of minimum pressure, reaching values of up to 25% of the total number of particles.

Figure 4.12(b) presents the average number of collisions with background particles that an inlet particle has undergone before reaching its position. As expected, the number of collisions increases along the z axis and it reaches the maximum value of ≈ 1.8 collisions. This is of course an averaged value, meaning that there are inlet particles which did not collide, as well as inlet particles that have collided much more than 1.8 times with background particles.

Finally, in figure 4.12(c) the fractional concentration of inlet particles which have never collided with background particles is reported. As expected, the concentration of such particles decreases rapidly in the regions with a high concentration of

background particles (along the axis and across the barrel shock). This clearly demonstrates that the inlet particles do interact with the background particles that invaded the supersonic region and influence the flow.

Experimental indications for the presence of background particles in the expansion-shock region were also found by Engeln et al. in [21], Vankan et al. in [114] and Gabriel et al. in [115]. Therefore, our study gives a numerical support to the hypothesis of Engeln et al., Vankan et al. and Gabriel et al. that background particles can penetrate the supersonic region and, by interacting with the inlet particles, can influence the flow field.

4.5 Conclusions

The gas dynamics of a hot gas jet supersonically expanding into a low pressure (20 – 100 Pa) chamber is studied by means of a hybrid coupled continuum-DSMC method.

This method gives the possibility to save computational time using CFD in most of the domain and to use DSMC only where it is necessary in order to correctly model the flow.

Answers to two main questions about supersonic expansion in a low pressure environment have been found: the importance of taking into account rarefaction effects in modelling the flow and the invasion of the supersonic region by background particles. We have shown that, because of the presence of rarefaction effects, already at 100 Pa chamber pressure the continuum approach is not suitable to model the flow, while a hybrid continuum-DSMC method can be applied correctly and efficiently.

Through an analysis of the velocity distributions and the tracking of particles and collisions in the supersonic region, we have demonstrated the presence of background particles in this region, thus proving the invasion of the supersonic region by background particles passing through the barrel shock.

5. Conclusions

The aim of the present work was the development of a comprehensive simulation model for the gas flow dynamics in a complicated environment such as that encountered in thin film deposition processes based on the application of an expanding gas jet.

From the preliminary study presented in chapter 1 it became clear that it is not possible to model those kind of processes using commercially available software packages and/or commonly used methods (e.g. CFD and DSMC). This study showed the presence of a continuum-rarefied regime transition which could strongly influence the properties and characteristics of the flow.

For this reason a hybrid CFD/DSMC code, capable of handling gas flow regimes from the continuum to the free molecular, has been developed, validated and applied to simulate the flow field in the expanding gas jet thin film deposition process of interest. Three main issues have been addressed in this work:

- CFD/DSMC coupling in steady-state and transient flows,
- Influence of rarefaction on expanding gas jet hydrodynamics,
- Supersonic region invasion by background particles in rarefied supersonic jet expansion.

Each of these questions will be discussed separately in the next sections.

5.1 CFD/DSMC coupling in steady-state and transient flows

The first research question concerned the challenge of accurately coupling two fundamentally different flow simulation approaches: the CFD (Computational Fluid Dynamics) approach based on the solution of the compressible Navier-Stokes equations, and the particle based DSMC (Direct Simulation Monte Carlo) method, both in steady-state and unsteady flow simulations.

Chapter 3 describes the two different strategies used for steady-state and unsteady flows and discusses, through a sensitivity analysis of the method to various parameters, the potentials and limitations of the method.

From the discussion presented in chapter 3 it was clear that the coupling method used (overlapped Schwarz coupling with Dirichlet-Dirichlet boundary conditions) was showing only a weak sensitivity to various parameters, e.g. the exact position of the CFD/DSMC interface, the size of the overlap region, and the DSMC noise.

The latter proved to be a clear advantage of the chosen coupling method over the more commonly used flux-based coupling, both for steady-state and transient flows. For transient flows, another clear advantage of the chosen coupling method was that the CFD and DSMC time steps can be decoupled, and that in general a coupling time step can be used which is much larger than the DSMC time step.

The study performed was also highlighting some limits of the method. For unsteady flow simulations it was found to be necessary to keep the Courant number, based on the coupling time step $\Delta t_{\text{coupling}}$, the CFD cell size Δx_{CFD} and the molecular most probable velocity C_r , below 1 in order to avoid instabilities.

Furthermore, it was found to be necessary to restrict the application of the CFD approach to regions where $\text{Kn} \lesssim 0.1$. Not respecting this condition leads to the appearance of instabilities.

The hybrid Schwarz coupling method has been validated against theoretical and DSMC results in chapter 3 and against theoretical and experimental results in chapter 4. The validation showed the accuracy of the hybrid CFD/DSMC in various test cases in predicting both macroscopic variables (e.g. pressure, temperature, velocity) and microscopic characteristics of the flow (e.g. the particles velocity distribution, particle's collisions).

From our study it was clear that for the type of flows of interest the hybrid coupling CFD/DSMC method is much more accurate than CFD, and it is also applicable in conditions where the CPU expenses of full DSMC are inadmissible.

5.2 Influence of rarefaction on expanding gas jet hydrodynamics

The second research question we answered in this thesis concerns the effect of rarefaction on gas jets expanding into (near) vacuum. In particular we analyzed the necessity of taking into account the continuum-rarefied regime transition through a molecular approach when simulating the flow field in such flows. This issue has been studied in chapter 4.

The hybrid coupling method has been used to simulate the flow field in the geometry of a reactor for thin film deposition and in the conditions met during deposition processes. A comparison between hybrid simulations, full CFD simulations and experimental data provided insight into the influence of rarefaction effects on both velocity and temperature fields.

It was clear that because of rarefaction the expansion predicted by the hybrid method was stronger than that predicted by the continuum approach, reaching a lower tem-

perature and higher velocity (approximately 200 – 500 m/s higher) in the supersonic region, in agreement with the experiments. The shock was moved downstream and downstream from the shock the temperature predicted by the hybrid method, in agreement with experimental observations, was significantly (500 – 1500 K) lower than the one calculated by the continuum approach.

Since already at 100 Pa chamber pressure the full CFD simulations were in qualitative and quantitative deviation from the experimental observations, the necessity of a hybrid model (that on the one hand accounts for the molecular nature of the gas flow where needed, and on the other hand uses a continuum model where allowed in order to save computational time) was evident.

A further effect due to the rarefied flow conditions in the reactor is the phenomenon of invasion of the supersonic part of the flow by background particles. This phenomenon will be discussed in the next section.

5.3 Supersonic region invasion in rarefied supersonic jet expansion

In section 4.4.2 the invasion of background particles into the supersonic region of a hot gas jet expansion was demonstrated. In continuum conditions, because of the presence of the shock, the background particles, that are initially outside the supersonic region, would not be able to penetrate into it. However, we have demonstrated that, because of rarefaction, the shock becomes transparent and does not protect the supersonic region. Therefore, some particles may actually move into it from the subsonic part of the flow.

In order to demonstrate this hypothesis, in our simulation of a near-atmospheric gas jet expanding into a low pressure chamber at 20 Pa, two analyses of flow at the molecular scale have been performed.

In the first analysis, the velocity distribution profiles of the molecules were recorded in different positions in the supersonic region. This analysis showed a clear departure from thermodynamic equilibrium in this region. The possibility to discern the contribution of the background particles to the velocity distribution confirmed the hypothesis that they have an important role in generating the thermodynamic non-equilibrium by penetrating the supersonic region, and by colliding and interacting with the local particles.

A clear explanation of the reason why background particles can penetrate the supersonic region under rarefied conditions was given by the second analysis we performed. Through the tracking of particles and collisions in the supersonic region it became clear that they concentrate in the region of minimum pressure.

In the supersonic region, the velocity increases reaching a maximum value, whereas, at the same location, density and pressure decrease reaching a minimum. The invading background particles penetrate the supersonic region driven into the region of

minimum pressure by favorable pressure gradients. Once they are there, because of the adverse pressure gradient, it is difficult for them to cross the Mach disk and/or the barrel shock. Therefore, the invading background particles concentrate in the region of minimum pressure. At a background pressure of 20 Pa the invading background particles concentration can reach values of up to 25% of the total number of particles in the supersonic region.

By means of tracking particle collisions, it was also possible to demonstrate that the invading background particles do interact with the local particles. At a background pressure of 20 Pa, the average number of times that particles from the gas jet collided with invading background particles was found to reach values up to ≈ 1.8 collisions. This is of course an averaged value, meaning that there are jet particles which did not collide as well as particles that collided much more than 1.8 times with background particles. This clearly proves that the background particles can invade the supersonic region and, colliding and interacting with local particles, can produce non-equilibrium, thus influencing the flow field.

5.4 General conclusions and outlook

The work presented in this thesis provides a solid basis for modelling gas flows with continuum-rarefied transitions, such as for instance encountered in thin film deposition processes based on near atmospheric pressure gas jets expanding into a low pressure deposition chamber. The developed hybrid CFD/DSMC approach was found to be flexible, robust and accurate, and to have several advantages over other published hybrid approaches.

For the actual modelling of thin film deposition processes, the hybrid approach has the possibility to apply the DSMC method in a thin zone above the deposition surface, allowing one to account for non-equilibrium effects near that surface and facilitating a further coupling to particle based surface models such as MD (Molecular Dynamics) or Monte Carlo.

The modelling of thin film deposition processes will necessitate that the CFD and DSMC parts of the developed CROW code, and their coupling, are extended by multi-species and reaction capabilities. This is relatively straightforward [34; 117], but was outside the scope of this thesis.

Bibliography

- [1] L. Boltzmann, *Sitzungsberichte Akademie der Wissenschaften Wien*, **66** pp. 275–370 (1872)
- [2] J.C. Maxwell, *Philos. Trans. R. Soc. London* **170** pp. 231–256 (1879)
- [3] B. Adler, *Phys. A* **240** pp. 193–195 (1997)
- [4] N.G. Hadjiconstantinou, *Phys. of Fluids* **15** pp. 2352–2354 (2003)
- [5] N.G. Hadjiconstantinou, *2nd Int. Conf. on Microchannels and Minichannels*, ed. S.G. Kandlikar, Rochester, New York, pp. 289–296 (2004)
- [6] G.A. Bird, *Molecular Gas Dynamics and the Direct Simulation Monte Carlo*, Clarendon Press, Oxford Univ. Press, Oxford (1998)
- [7] N.G. Hadjiconstantinou, *J. Comput. Phys.* **154** pp. 245–265 (1999)
- [8] P. Le Tallec, F. Mallinger, *J. Comput. Phys.* **136** pp. 51–67 (1997)
- [9] O. Aktas, N.R. Aluru, *J. Comput. Phys.* **178** pp. 342–372 (2002)
- [10] H.S. Wijesinghe, N.G. Hadjiconstantinou, *Int. J. Multiscale Comp. Eng.* **2** (2) pp. 189–202 (2004)
- [11] R. Roveda, D.B. Goldstein, P.L. Varghese, *J. Spacecraft Rockets* **35** pp. 258–265 (1998)
- [12] A.L. Garcia, J.B. Bell, W.Y. Crutchfield, B.J. Alder, *J. Comput. Phys.* **154** pp. 134–155 (1999)
- [13] C.E. Glass, P.A. Gnoffo, *8th AIAA/ASME Joint Thermophysics and Heat Transfer Conference*, AIAA Paper 2002–3099 (2002)
- [14] J.S. Wu, Y.Y. Lian, G. Cheng, R.P. Koomullil, K.C. Tseng, *J. Comput. Phys.* **219** pp. 579–607 (2006)

-
- [15] T.E. Schwartzentruber, L.C. Scalabrin, I.D. Boyd, AIAA-2006-3602, June 2006, San Francisco, CA.
- [16] T.E. Schwartzentruber, I.D. Boyd, *J. Comput. Phys.* **215** (2) pp. 402–416 (2006)
- [17] M.C.M. van de Sanden, R.J. Severens, J.W.A.M. Gielen, R.M.J. Paffen, D.C. Schram, *Plasma Sources Sci. Technol.* **5** (2) pp. 268–274 (1996)
- [18] M.C.M. van de Sanden, J.M. de Regt, D.C. Schram, *Plasma Sources Sci. Technol.* **3** pp. 501–510 (1994)
- [19] M.C.M. van de Sanden, R. van de Bercken, D.C. Schram, *Plasma Sources Sci. Technol.* **3** pp. 511–520 (1994)
- [20] R.F.G. Meulenbroeks, R.A.H. Engeln, M.N.A. Beurskens, R.M.J. Paffen, M.C.M. van de Sanden, J.A.M. van der Mullen, D.C. Schram, *Plasma Sources Sci. Technol.* **4** pp. 74–85 (1995)
- [21] R. Engeln, S. Mazouffre, P. Vankan, D.C. Schram, N. Sadeghi, *Plasma Sources Sci. Technol.* **10** pp. 595–605 (2001)
- [22] S. Mazouffre, M.G.H. Boogaarts, I.S.J. Backer, P. Vankan, R. Engeln, D.C. Schram, *Phys. Rev. E* **64** (2) 16411 (2001)
- [23] S. Mazouffre, M.G.H. Boogaarts, J.A.M. van der Mullen, D.C. Schram, *Phys. Rev. Lett.* **84** pp. 2622–2625 (2000)
- [24] J.J. Beulens, G.M.W. Kroesen, P.M. Vallinga, D.C. Schram, *proc. Int. Symp. Plasma Chemistry (ISPC-9)*, Pugnochiuso, Italy, ed. R.d’Agostino **1** pp. 302–308 (1989)
- [25] J.J. Beulens, D. Milojevic, D.C. Schram, P.M. Vallinga, *Phys. Fluids B* **3** pp. 2548–2557 (1991)
- [26] K.T.A.L. Burm, W.J. Goedheer, D.C. Schram, *Phys. Plasmas* **6** pp. 2622–2627 (1999)
- [27] G.M. Janssen, PhD Thesis University of Technology, Eindhoven, The Netherlands (2000)
- [28] W.M.M. Kessels, A. Leroux, M.G.H. Boogaarts, J.P.M. Hoefnagels, M.C.M. van de Sanden, D.C. Schram, *J. Vac. Sci. Technol. A* **19** pp. 467–476 (2001)
- [29] FLUENT 5, *User’s Manual*, Fluent Inc., Lebanon (USA) (1998)
- [30] M.C.M. van de Sanden, J.M. de Regt, G.M. Jansen, J.A.M. van der Mullen, D.C. Schram, B. van der Sijde, *Rev. Sci. Instrum.* **63** pp. 3369–3377 (1992)

-
- [31] S.E. Selezneva, M.I. Boulos, M.C.M. van de Sanden, R. Engeln, D.C. Schram, *J. Phys. D: Appl. Phys.* **35** pp. 1362–1372 (2002)
- [32] S.E. Selezneva, M. Rajabian, D. Gravelle, M.I. Boulos, *J. Phys. D: Appl. Phys.* **34** pp. 2862–2874 (2001)
- [33] J.O. Hirschfelder, C.F. Curtis, R.B. Bird, *Molecular Theory of Gases and Liquids*, Wiley, New York, 4th edition (1954)
- [34] R. Dorsman, PhD Thesis University of Technology, Delft, The Netherlands (2007)
- [35] M. Okkerse, C.R. Kleijn, H.E.A. Van Den Akker, M.H.J.M. De Croon, G.B. Marin, *J. Appl. Phys.* **88** (7) pp. 4417–4428 (2000)
- [36] C.R. Kleijn, *Thin Solid Films* **365** (2) pp. 294–306 (2000)
- [37] C.R. Kleijn, R. Dorsman, K.J. Kuijlaars, M. Okkerse and H. van Santen, *Journal of Crystal Growth* **303** (1) pp. 362–380 (2007)
- [38] G. Abbate, B.J. Thijsse, C.R. Kleijn, Hybrid Navier-Stokes/DSMC simulations of gas flows with rarefied-continuum transitions, In: *Advanced Computational Method in Science and Engineering*, Chapter 1, Springer (2008)
- [39] S. Chapman, T.G. Cowling, *The Mathematical Theory of Non-Uniform Gases*, Cambridge Univ. Press, London (1960)
- [40] H. Grad, *Commun. Pure Appl. Math.* **2** 331 (1949)
- [41] G.N. Patterson, *Molecular Flow of Gases*, Wiley, New York (1956)
- [42] J.C. Maxwell, *Philos. Trans. R. Soc. London*, **157** pp. 49–88 (1867)
- [43] W.G. Vincenti, C.H. Krueger Jr., *Introduction to Physical Gas Dynamics*, Wiley, New York (1965)
- [44] A.L. Garcia, B.J. Alder, *J. Comput. Phys.* **140** pp. 66–70 (1998)
- [45] M. Manzini, A. Ticca, G. Zanetti, <http://crs4.it> (May 2001)
- [46] S.Y. Chou, D. Baganoff, *J. Comput. Phys.* **130** pp. 217–230 (1997)
- [47] T. Lou, D.C. Dahlby, D. Baganoff, *J. Comput. Phys.* **145** pp. 489–510 (1998)
- [48] B. van Leer, *J. Comput. Phys.* **32** pp. 101–136 (1979)
- [49] P.L. Roe, *J. Comput. Phys.* **43** pp. 357–372 (1981)

-
- [50] H. Brezis, *Analyse fonctionnelle, théorie et applications*, Paris, New York, (1983)
- [51] D. Gilbarg, N.S. Trudinger, *Partial Differential Equations of Second Order*, Springer-Verlag, Berlin (1998)
- [52] R.B. Bird, W.E. Stewart, E.N. Lighfood, *Transport Phenomena*, Wiley, New York, 1960
- [53] J.D. Ramshaw, *J. Non-Equilib. Thermodyn.* **15** pp. 295–300 (1990)
- [54] G.A. Sod, *J. Comput. Phys.* **27** pp. 1–31 (1978)
- [55] A. Harten, *J. Comput. Phys.* **49** pp. 357–393 (1983)
- [56] H. Lamb, *Hydrodynamics*, 6th ed., New York: Dover (1945)
- [57] R.L. Daugherty, J.B. Franzini, *Fluid Mechanics*, 6th ed., New York: McGraw-Hill (1965)
- [58] B.R. Munson, D.F. Young, T.H. Okiishi, *Fundamentals of Fluid Mechanics*, John Wiley and Sons (2002)
- [59] W. Wagner, *J. Statist. Phys.* **66** pp. 1011–1044 (1992)
- [60] P.L. Bhatnagar, E.P. Gross, M. Krook, *Phys. Rev.* **94** pp. 511–525 (1954)
- [61] C. Cercignani, M. Lampis, *Rarefied Gas Dynamics*, ed. K.Karamcheti, Academic Press, New York (1974)
- [62] R.G. Lord, *Rarefied Gas Dynamics*, ed. A.E.Beylich, VCH Verlagsgesellschaft GmbH, Weinheim, Germany (1991)
- [63] R.G. Lord, *Phys. Fluids A* **3** pp. 706–710 (1991)
- [64] G.A. Bird, ed.S.S. Fischer, 12th *Int. Symp. Rarefied Gas Dynamics*, part 1, pp. 239–255 (1981)
- [65] K. Koura, H. Matsumoto, *Phys. Fluids* **3** pp. 2459–2465 (1991)
- [66] K. Koura, H. Matsumoto, *Phys. Fluids* **4** pp. 1083–1085 (1992)
- [67] R.P. Nance, D.B. Hash, H.A. Hassan, *J. Thermophys. Heat Trans.* **12** pp. 447–449 (1998)
- [68] R.C. Reid, T.K. Sherwood, *Properties of Gases and Liquids*, McGraw-Hill, New York, 2nd edition, (1966)
- [69] C.R. Wilke, C.Y. Lee, *Industrial and Engineering Chemistry* **47** pp. 1253–1257 (1955)

-
- [70] G. Chen, I.D. Boyd, *J. Comput. Phys.* **126** pp. 434–448 (1996)
- [71] F.J. Alexander, A.L. Garcia, B.J. Alder, *Phys. Fluids* **10** pp. 1540–1542 (1998)
- [72] A.L. Garcia, W. Wagner, *Phys. Fluids* **12** pp. 2621–2633 (2000)
- [73] N.G. Hadjiconstantinou, *Phys. Fluids* **12** pp. 2634–2638 (2000)
- [74] D.J. Rader, M.A. Gallis, J.R. Torczynski, W. Wagner, *Phys. Fluids* **18** 77102 (2006)
- [75] F. Sharipov, V. Seleznev, *J. Phys. Chem. Ref. Data* **27** pp. 657–706 (1998)
- [76] D.W. Mackowski, D.H. Papadopoulos, D.E. Rosner, *Phys. Fluids* **11** pp. 2108–2116 (1993)
- [77] D.C. Wadsworth, *Phys. Fluids A* **5** pp. 1831–1839 (1993)
- [78] S.K. Loyalka, *Phys. Fluids A* **1** pp. 403–408 (1989)
- [79] Y. Sone, T. Ohwada, K. Aoki, *Phys. Fluids A* **1** pp. 363–370 (1989)
- [80] T.A. Delchar, *Vacuum Physics and Techniques*, Chapman & Hall, St Edmundsbury Press, Suffolk (1993)
- [81] C. Cercignani, R. Illner, M. Pulvirenti, *The Mathematical Theory of Dilute Gases*, Springer, New York (1994)
- [82] P.A. Lagerstrom, J.D. Cole, L. Trilling, Guggenheim Aeronautical Laboratory, California Institute of Technology, Calcit Report (1949)
- [83] J.P. Moran, S.F. Shen, *J. Fluid Mechanics*, **25** pp. 705–718 (1966)
- [84] R.J. Mason, *Phys. Fluids* **11** (12) pp. 2524–2532 (1968)
- [85] S. Yohung, W.K. Chan, *J. Vac. Sci. Technol. A* **22** pp. 383–394 (2004)
- [86] C. Cai, I.D. Boyd, J. Fan, *J. Thermophys. Heat Trans.* **14** (3) pp. 368–378 (2000)
- [87] V.I. Kolobov, R.R. Arslanbekov, V.V. Aristov, A.A. Frolova, S.A. Zabelok, *J. Comput. Phys.* **223** pp. 589–608 (2007)
- [88] J.F. Bourgat, P. Le Tallec, M.D. Tidriri, *J. Comput. Phys.* **127** pp. 227–245 (1996)
- [89] H.S. Wijesinghe, R.D. Hornung, A.L. Garcia, N.G. Hadjiconstantinou, *J. Fluids Eng.* **126** pp. 768–776 (2004)

- [90] D.B. Hash, H.A. Hassan, AIAA paper AIAA-97-2507 (1997)
- [91] G.C. Cheng, R.P. Koomullil, B.K. Soni, *Math. Comput. Simulation* **75** pp. 161–170 (2007)
- [92] W.L.Wang, I.D.Boyd, *36th AIAA Thermophysics Conference*, 23-26 June 2003, Orlando, Florida, AIAA paper 2003-3644
- [93] A. Carlson, R. Roveda, I.D. Boyd, G.V. Candler, *42nd AIAA Aerospace Sciences Meeting and Exhibit*, 5-8 January 2004, Reno, NV, AIAA paper 2004-1180
- [94] T.E. Schwartzentruber, L.C. Scalabrin, I.D. Boyd, *J. Comput. Phys.* **225** pp. 1159–1171 (2007)
- [95] G. Abbate, B.J. Thijsse, C.R. Kleijn, *proc. Int. Conf. Comput. Sci. 2007*, LNCS 4487, Y. Shi et al. (Eds.) pp. 842–849 (2007)
- [96] F. Sharipov, *Brazilian J. Phys.* **33** (2) pp. 398–405 (2003)
- [97] C. Cai, I.D. Boyd, *36th AIAA Plasmadynamics and Laser Conference*, 6-9 June 2005, Toronto, Ontario, Canada, AIAA-2005-4662
- [98] Wen-Lan Wang, I.D. Boyd, *40th AIAA Aerospace Sciences Meeting and Exhibit*, 14-17 January 2002, Reno, NV
- [99] H.M. Mott-Smith, *Phys. Rev.* **82** (6) pp. 885–892 (1951)
- [100] D. Hash, H. Hassan, AIAA Paper AIAA-96-0353 (1996)
- [101] G. Abbate, B.J. Thijsse, C.R. Kleijn, *Int. J. Multiscale Comput. Eng.* **6** (1) pp. 1–12 (2008)
- [102] R. Roveda, D.B. Goldstein, P.L. Varghese, *J. Spacecraft Rockets* **37** (6) pp. 753–760 (2000)
- [103] A.J. Lofthouse, I.D. Boyd, M.J. Wright, AIAA-2006-0993, January 2006, Reno, NV.
- [104] G. Abbate, B.J. Thijsse, R. Engeln, M.C.M. van de Sanden, D.C. Schram, C.R. Kleijn, *Phys. Rev. E* **77** (1) 036703 (2008)
- [105] J.W.A.M. Gielen, W.M.M. Kessels, M.C.M. van de Sanden, D.C. Schram, *J. Appl. Phys.* **82** (5) pp. 2643–2654 (1997)
- [106] J.B. Fenn, J.B. Anderson, *Rarefied Gas Dynamics 2*, J.H. de Leeuw Eds., New York: Academic (1966)
- [107] R. Campargue, *J. Chemical Phys.* **52** pp. 1795–1802 (1970)

-
- [108] M.C.M. van de Sanden, J.M. de Regt, D.C.Schram, *Phys. Rev. E* **47** pp. 2792–2797 (1993)
- [109] G.M. Janssen, J. van Dijk, D.A. Benoy, M.A. Tas, K.T.A.L. Burm, W.J. Goedheer, J.A.M. van der Mullen, D.C. Schram, *Plasma Sources Sci. Technol.* **8** (1) pp. 1–14 (1999)
- [110] P.W. Vankan, D.C. Schram, R. Engeln, *proc. 24th Int. Symp. Rarefied Gas Dynamics*, Monopoli - Italy (M. Capitelli Eds.) pp. 361–367 (2004)
- [111] P.W. Vankan, D.C. Schram, R. Engeln, *Plasma Sources Sci. Technol.* **14** pp. 744–750 (2005)
- [112] G. Abbate, B.J. Thijsse, C.R. Kleijn, *proc. Int. Conf. Comput. Sci.*, 23-25 June, Krakow (Poland), LNCS 5102, part II, M. Buback et al. (Eds.), Springer-Verlag Berlin Heidelberg, pp. 251-260 (2008)
- [113] S. Mazouffre, I. Bakker, P. Vankan, R. Engeln, D.C. Schram, *Plasma Sources Sci. Technol.* **11** pp. 439–447 (2002)
- [114] P. Vankan, S. Mazouffre, R. Engeln, D.C. Schram, *Phys. Plasmas* **12** 102303 (2005)
- [115] O. Gabriel, P. Colsters, R. Engeln, D.C. Schram, *proc. 25th Int. Symp. Rarefied Gas Dynamics*, S.Petersburg (Russia), M.S. Ivanov and A.K. Rebrov (Eds.), (2006)
- [116] H. Ashkenas, F.S. Sherman, *Experimental methods in rarefied gas dynamics*, In: *Rarefied Gas Dynamics*, Vol. II, J.H. de Leeuw (Eds.), Academic Press, New York (1965)
- [117] K.J. Kuijlaars, PhD Thesis University of Technology, Delft, The Netherlands (1996)

Acknowledgements

It was the 16th August 2004 when I started my PhD project here in Delft. Since then four years passed and a lot of things happened...Finally my PhD is over and it is time to thank all the people who have helped me during these years.

First of all, I would like to thank my supervisors Chris and Barend for their support, tips and discussions. I would also thank Daan Schram, Richard van de Sanden, Richard Engeln and Onno Gabriel for their support, discussions and making available to me their experimental data while I was working on the Physics Review E paper and on the chapter 4 of this thesis. Moreover, I would like to give very special thanks to Richard Engeln and Onno Gabriel also for all their effort in making available to me the picture that you can see on the cover of this thesis.

Similarly, I would like to thank Valeria Krzhizhanovskaya and Alfons Hoekstra for inviting me to submit a paper to the International Journal of Multiscale Computational Engineering.

I will always be particularly grateful to HP, Jos van 't Westende and Ruurd for having been always available and for helping me when I really needed it during my project. In order to feel comfortable at your work, it is also important to find a familiar and relaxing working environment, and for that I thank Usama and Anton: How boring would have been our office without you!!

I would also thank Annkatrien for her "legal and bureaucratic" support in translating documents from Dutch to English and in the difficult task of filling the tax-form, Volkert for translating the summary, and Cor and Helmar for translating the propositions which accompany this thesis.

Apart from the office related life, I would like to thank Luciano who introduced me to the Netherlands when I was just arrived.

Despite of the awful coffee (or maybe it is more correct to define it "warm dark water") I cannot forget the relaxing atmosphere of the coffee-breaks at Aula with Francesco e Fabio...I wish you the best in your life and career!!

During these years I was investing a lot in learning foreign languages and for that I would like to thank my "teachers" Yann, Pidio, Mathieu and Micha...I appreciated your fruitful help!

The most grateful thankwords, however, are for Francesco, Alessandro and Fanny, my best friends here in the Netherlands, and Roberta my best friend in Italy.

I would like to give a special thank also to Eleonora for her support in these last months. I will never find the right words to thank Concetta for all her support in the most difficult moments I had in the last two years, for all I learned from her, for our discussions and experiences we shared. Probably without her strength, support and trust I would never have finished my PhD.

Finally I would like to thank my parents and my sister, who, even from far away, have always been very close to me in every moment I needed them.

List of publications

- G. Abbate, B.J. Thijsse, C.R. Kleijn, Hybrid N-S/DSMC gas flow simulations in very low pressure thin film deposition, proc. *25th Rarefied Gas Dynamics Symposium*, 15-21 July, Saint Petersburg (Russia), M.S. Ivanov and A.K. Rebrov (Eds.), Novosibirsk: House of the Siberian Branch of the Russian Academy of Science, pp. 830-835 (2006)
- G. Abbate, B.J. Thijsse, C.R. Kleijn, Coupled N-S/DSMC method for transient and steady-state gas flows, proc. *Int. Conf. Comput. Sci.*, 27-30 May, Beijing (China), LNCS 4487, part I, Y. Shi et al. (Eds.), Springer-Verlag Berlin Heidelberg, pp. 842-849 (2007)
- G. Abbate, B.J. Thijsse, C.R. Kleijn, Validation of a hybrid N-S/DSMC method for multi-scale transient and steady-state gas flows, *Int. J. Multiscale Comput. Eng.* **6** (1) pp. 1-12 (2008)
- G. Abbate, B.J. Thijsse, R. Engeln, M.C.M. van de Sanden, D.C. Schram, C.R. Kleijn, Flow dynamics of a stationary supersonic hot gas expansion, *Phys. Rev. E* **77** (1) 036703 (2008)
- G. Abbate, B.J. Thijsse, C.R. Kleijn, Hybrid Navier-Stokes/DSMC simulations of gas flows with rarefied-continuum transitions, In: *Advanced Computational Method in Science and Engineering*, Chapter 1, Springer (2008)
- G. Abbate, B.J. Thijsse, C.R. Kleijn, Multi-Scale Modelling of the Two-Dimensional Flow Dynamics in a Stationary Supersonic Hot Gas Expansion, proc. *Int. Conf. Comput. Sci.*, 23-25 June, Krakow (Poland), LNCS 5102, part II, M. Buback et al. (Eds.), Springer-Verlag Berlin Heidelberg, pp. 251-260 (2008)
- G. Abbate, B.J. Thijsse, C.R. Kleijn, Hybrid Continuum/Molecular Simulations of Transient Gas Flows with Rarefaction, submitted to *AIAA Journal*

About the author

Giannandrea Abbate was born on 2nd December 1978 in Caserta (Italy). In 1993, at the age of 15 he decided to attend the "Nunziatella" Military School of Naples (Italy) where he graduated from secondary school ("Maturità Scientifica") in 1997. Soon he realized not to be made for a military career and started his Aerospace Engineering studies at the "Federico II" University of Naples (Italy). He was a very active student and took part in several projects and students' activities such as the SSETI - Student Space Exploration & Technology Initiative workshop in cooperation with ESA - European Space Agency. During this workshop he was a member of the team of the University of Naples entrusted for the design of the power system of a micro-satellite. In 2003 he received his MSc degree ("Laurea") based on his research entitled "Reduction of the wall-interference in a transonic wind tunnel". The research for his MSc thesis was performed at CIRA - Italian Centre for Aerospace Research. Immediately following his MSc, he started working as independent consultant engineer in Naples. At that time he was very interested in UAVs - Unmanned Aerial Vehicles and he took part in two european projects: CAPECON - Civil UAV APplications & Economic effectivity of potential CONfiguration solutions, where he was entrusted for the primarily design of an UAV, and USICO - UAV Safety Issues for Civil Operations, in which he wrote a part of the draft of the european regulation for UAVs' civil use. In September 2003, he moved to Bruxelles (Belgium) where he started the Diploma Course at the Von Karman Institute for Fluid Dynamics. During the Diploma Course he worked on his research project "Investigation on water-cooled calorimeter heat-flux measurements in plasmatron facility". Immediately following the Diploma Course he started his PhD project at the "Kramers Laboratorium voor Fysische Technologie" (currently a part of the Multi-Scale Physics department) of the Delft University of Technology (The Netherlands).